
Unfolding the Milky Way bulge

Oscar A. Gonzalez



München 2012

Unfolding the Milky Way bulge

Oscar A. Gonzalez

Dissertation
an der Fakultät für Physik
der Ludwig–Maximilians–Universität
München

vorgelegt von
Oscar A. Gonzalez
aus Chillan, Chile

München, den 14.05.2012

Erstgutachter: Priv. Doz. Dr. Ortwin Gerhard

Zweitgutachter: Priv. Doz. Dr. Markus Kissler-Patig

Tag der mündlichen Prüfung: 25.06.2012

Contents

Summary	xv
Zusammenfassung	xvi
1 The Milky Way bulge in the general context of galactic bulges	1
1.1 An overview of galactic bulges	2
1.1.1 Classical bulges	3
1.1.2 Galactic bars and boxy-bulges	4
1.1.3 Pseudo-bulges	5
1.1.4 Clump-origin bulges	6
1.2 The Bulge of the Milky Way	7
2 Stellar abundances as tracers of formation history	11
2.1 The chemical composition of stars	11
2.2 Model atmospheres and abundance measurements	12
2.3 Alpha elements and the formation timescale	13
3 The formation timescale of the Galactic bulge from alpha-element abundance measurements and gradients	15
3.1 The sample	16
3.2 Stellar parameters	18
3.3 Abundance analysis	18
3.4 Error analysis	22
3.4.1 Error due to stellar parameters uncertainties	22
3.4.2 Errors from the spectral synthesis	22
3.4.3 The role of spectral resolution	25
3.5 Results	27
3.5.1 Thick and thin disk sample	27
3.5.2 Alpha elements across the bulge, thick and thin disk	27
3.5.3 Is there an α -element gradient in the bulge?	36
3.5.4 Correlation with kinematics	37
3.6 Implications of $[\alpha/\text{Fe}]$ abundance results on the Bulge formation history	37
3.7 Conclusions	40

4	The Red Clump as tracer of the Bulge extinction and structure	41
4.1	The VVV survey data	43
4.1.1	Multiband catalogs	44
4.1.2	Photometric calibration	45
4.2	Characterizing the Red Clump in the Bulge color-magnitude diagram	46
4.2.1	Red clump color in the reference Bulge field: Baade's Window	47
4.2.2	The absolute magnitude of the red clump	48
5	The extinction towards the Milky Way bulge	51
5.1	Determination of A_K values and the complete extinction map of the Bulge	52
5.1.1	A note about the extinction law	57
5.1.2	BEAM calculator	59
5.2	Comparison with existing extinction maps of the Bulge	60
5.3	Implications for Bulge studies	63
5.3.1	The Color-Magnitude diagram of the inner Bulge	63
5.3.2	Photometric effective temperatures	66
5.3.3	Bulge luminosity function and distances	68
5.4	Conclusions	69
6	The Bulge structure	71
6.1	The data	73
6.2	Tracing the bar in the inner regions	73
6.3	Is there a secondary inner bar in the Milky Way?	77
6.4	The bar at higher latitudes	78
6.5	Conclusions	80
7	Towards the complete picture of the Milky Way bulge metallicity gradients	83
7.1	Bulge photometric metallicity distributions	83
7.2	Spectroscopic vs. photometric metallicity distributions along the minor axis of the Bulge	85
7.3	The complete metallicity map of the Bulge	86
8	Conclusions and outlook	89
A	Abundances of 650 bulge red giants	91
B	Bulge VVV tile centre coordinates	109
	Acknowledgments	122

List of Figures

1.1	Color image of the Sombrero galaxy (M104), the prototypical example of a disk galaxy with a large classical, merger-built bulge in its center. Image was obtained directly from the ESO photo release eso0007 "Fine shades of a Sombrero" and was made by a combination of three CCD images from the FORS1 multi-mode instrument on VLT ANTU, by Peter Barthel from the Kapteyn Institute (Groningen, The Netherlands) during an observing run at the ESO Paranal Observatory.	4
1.2	Spitzer/IRAC 3.6 m negative image of NGC 4565, taken from the work of Kormendy & Barentine (2010), showing a clear boxy-bulge structure in its center. This is panel a of Figure 2 from Kormendy & Barentine (2010), reproduced by permission of the AAS.	6
1.3	Spitzer/IRAC 3.6 m negative image of NGC 4565, using a contrast and brightness stretching to highlight its pseudobulge from the work of Kormendy & Barentine (2010). This is panel b of Figure 2 from Kormendy & Barentine (2010), reproduced by permission of the AAS	7
2.1	Illustration of the $[\alpha/\text{Fe}]$ ratio versus metallicity trends expected for a classical bulge population formed on a short timescale and the drop produced by the contribution of SN Ia during a more extended process. The absolute values of these trends depend on the IMF and the SFR of the population.	14
3.1	Color magnitude diagrams for the four fields: Baade's window (<i>upper left</i>), $b=-6^\circ$ (<i>upper right</i>), $b=-12^\circ$ (<i>lower left</i>) and NGC6553 (<i>lower right</i>). Spectroscopic targets in each field are marked as large filled circles. Magnitudes were obtained from the OGLE catalogue (Udalski et al. 2002) and the Z08 catalog obtained from WFI images	17
3.2	Calibration of the synthesis regions for the Sun, Arcturus and μ -Leonis. Observed spectra convolved to the GIRAFFE resolution are shown as black dotted line and the red dashed line shows the synthetic spectra using the stellar parameters from L07 and abundances in Table 3.3.	20

3.3	Example of the final output of the synthesis procedure in order to derive the abundances of Mg (upper left), Ca (upper right), Ti (lower left) and Si (lower right). Observed spectrum for target star 212175c6 is plotted as black dots and the red dashed line shows the synthetic spectrum using the best fitting abundance as obtained from our procedure.	21
3.4	Abundance errors associated with the uncertainties in effective temperature (upper left), surface gravity (upper right), metallicity (lower left) and microturbulence (lower right). A change of ± 200 K was applied to T_{eff} , ± 0.1 dex to $[\text{Fe}/\text{H}]$, ± 0.3 dex to $\log g$ and ± 0.2 dex to ξ . Model atmosphere were then created and abundances were re-determined. Filled circles show the change in abundance as $\Delta[\text{X}/\text{Fe}] = [\text{X}/\text{Fe}] - [\text{X}/\text{Fe}]_{\pm\Delta}$ when changes were added to the original parameters. Empty circles show the change in abundance when the respective value is subtracted. Dashed lines show the mean variations $\sigma_{(+)}$ and $\sigma_{(-)}$ when the uncertainty in the stellar parameter is added and subtracted respectively.	23
3.5	Difference between the abundances measured using the same lines for stars observed twice in the field at $b = -12$. The dashed line shows the mean difference between both measurements and the dotted lines the 1σ around the mean.	24
3.6	$\Delta[\alpha/\text{Fe}] = [\alpha/\text{Fe}]_{\text{UVES}} - [\alpha/\text{Fe}]_{\text{GIRAFFE}}$ for our bulge sample plotted as black filled circles. The dashed line indicates the mean value of the difference and the dotted lines show the 1σ range around the mean difference for each element.	25
3.7	$\Delta[\alpha/\text{Fe}] = [\alpha/\text{Fe}]_{\text{HR}} - [\alpha/\text{Fe}]_{\text{LR}}$ for the disk sample plotted as black filled circles where the low resolution (LR) spectra were obtained by degrading the high resolution (HR) to the resolution of our GIRAFFE sample. The dashed line indicates the mean value of the difference and the dotted lines show the 1σ range for each element.	26
3.8	Difference between the stellar parameters obtained in this work and the values presented in AB10 calculated as $\Delta X = X_{\text{thiswork}} - X_{\text{AB10}}$. The dashed line indicates the mean value of the difference and the dotted lines show the 1σ range for each element.	28
3.9	Difference between the $[\alpha/\text{Fe}]$ values for Mg, Ca, Ti and Si obtained in this work and the values presented in AB10 calculated as $\Delta[\alpha/\text{Fe}] = [\alpha/\text{Fe}]_{\text{thiswork}} - [\alpha/\text{Fe}]_{\text{AB10}}$. The dashed line indicates the mean value of the difference and the dotted lines show the 1σ range for each element. In particular, disk giants used by AB10 to calculate their internal zero points are shown as red filled stars.	29
3.10	$[\text{Mg}/\text{Fe}]$ abundances in 4 fields of the bulge shown as red filled circles. Bulge globular cluster members are shown as black filled squares. $[\text{Mg}/\text{Fe}]$ abundances for the thick disk stars are shown as blue filled triangles and as empty black circles for the thin disk stars.	30
3.11	$[\text{Ca}/\text{Fe}]$ abundances in 4 fields of the bulge. Symbols are as in Fig. 3.10.	31
3.12	$[\text{Ti}/\text{Fe}]$ abundances in 4 fields of the bulge. Symbols are as in Fig. 3.10.	32
3.13	$[\text{Si}/\text{Fe}]$ abundances in 4 fields of the bulge. Symbols are as in Fig. 3.10.	33
3.14	$[\alpha/\text{Fe}]$ abundances in 4 fields of the bulge calculated as the average between Ca, Mg, Ti and Si abundances. Symbols are as in Fig. 3.10.	34

3.15	The left panels show $[\alpha/\text{Fe}]$ trends as a function of $[\text{Fe}/\text{H}]$ in 3 bulge fields located along the minor axis. Best fit trends are shown for both $[\text{Fe}/\text{H}]$ ranges, a metal-poor between -1.2 and -0.5 dex and a metal-rich between -0.3 and 0.2 dex, as well as the location of the knee in all fields. The right panels show the $[\alpha/\text{Fe}]$ distribution for each field.	35
3.16	Same as in Figure 3.15 for 2 bulge fields along the major axis.	35
3.17	Dispersion of radial velocity as a function of $[\alpha/\text{Fe}]$, in bins of 0.15 dex, for the three fields along the minor axis (filled circles and left axis scale). Overplotted as a dashed line is the $[\alpha/\text{Fe}]$ distribution for each field, which scale is given on the right. Globular cluster members in the sample were removed for this particular analysis.	38
4.1	Near-IR Color-Magnitude diagram for a sample of disk stars with measured distances from the Hipparcos satellite and 2MASS magnitudes. This is Figure 2 from Casetti-Dinescu et al. (2011), reproduced by permission of the AAS.	42
4.2	Distributions of the RA and DEC differences in arcsec between matched sources of single band, J and Ks, photometric catalogs. Crossmatching for field b278 is shown here as an example	44
4.3	J, H and K_s magnitudes differences between VVV catalogs and 2MASS. Dashed lines show the mean difference between both catalogs in the range denoted by the solid lines	45
4.4	VVV observed ($J - K_s, K_s$) CMD of a $20' \times 20'$ region within the tile b278 calibrated and completed with 2MASS photometry.	47
4.5	Right panel shows the observed color magnitude diagram for a 4×4 arcmin region centered in Baade's Window and a selection box corresponding to the red clump. Left panel shows the color distribution of these red clump stars. Overplotted is the best fit Gaussian curve with the mean RC color.	48
5.1	The mean value obtained from a Gaussian fit to a set of N data points randomly distributed following a Gaussian distribution centered on zero (solid horizontal line) and with a sigma of 0.10. The dashed vertical line shows the limit of 200 points adopted as the minimum number of stars in each subfield.	53
5.2	VVV coverage of the Bulge in Galactic coordinates. Each small square shows the coverage by individual $1^\circ \times 1.5^\circ$ tile from the VVV. Tile numbering for the VVV survey is described in Saito et al. (2012) and the coordinates of the center of each tile are listed in the Appendix B. The different color shading of the tiles depends on the spatial resolution ($2'$, $4'$ and $6'$, respectively) used to derive reddening from the mean color of the red clump stars (see text for details).	54
5.3	Red clump region of the observed color magnitude diagram for tile b306 (right panel) compared to the de-reddened one obtained by our procedure (left panel). Only a subsample of the stars are plotted in each CMD and contour levels are shown to mark the clump position and shape. The arrow in the right panel shows the reddening vector for a change in $E(B-V)$ of 0.5 magnitudes.	55

5.4	Extinction map of the Galactic Bulge for the complete region covered by the VVV survey. The A_{K_s} values are computed from $E(J - K_s)$ measurements assuming Cardelli et al. (1989) extinction law for all tiles. At A_{K_s} values larger than 1.5 mag the color scale saturates. The details of the extinction variation in the inner highly extinct regions, where A_{K_s} reaches up to 3.5 mag, are better seen in the upper panel of Fig. 5.8.	56
5.5	$(J - K_s)$ and $(J - H)$ color difference between our control field and those measured in the subfields of tiles b317, b303 and b275. The size of the subfields corresponds to the same resolution described in Fig. 2. The blue dashed line shows the relation $E(J - H) = 0.638E(J - K_s)$ corresponding to the extinction law from Cardelli et al. (1989) and red solid line to $E(J - H) = 0.671E(J - K_s)$ from Nishiyama et al. (2009)	58
5.6	Screen-shot of the BEAM calculator web-page. The user provides the center coordinates and field size to retrieve the reddening values and/or photometric metallicities.	59
5.7	Difference between the A_{K_s} values obtained in this work and those of Schlegel et al. (1998), as a function of Galactic latitude, for 1000 randomly distributed $30' \times 30'$ regions between $(-8^\circ < b < -1^\circ)$	61
5.8	The upper panel shows the inner $\sim \pm 2^\circ$ region around the Galactic plane of our VVV extinction map. A_{K_s} values are based on Cardelli et al. (1989) extinction law. Part of this region was also covered by the DENIS survey, used in Schultheis et al. (1999) to build an extinction map shown in the lower panel.	62
5.9	Upper panel shows the comparison of the A_{K_s} values obtained in this work and those of Schultheis et al. (1999) for the common inner Bulge region $(-2^\circ < b < +2^\circ)$. Lower panel shows the comparison with the SPITZER extinction map of Schultheis et al. (2009) for the central 1° of the Galaxy. Both plots are shown as density contours due to huge number of data points.	64
5.10	Left panel shows the VVV observations based HESS diagram of a $40'$ region in the inner Bulge $(l, b) = (-1.0, -1.0)$. The right panel shows the diagram for the same region as obtained from the Besancon model.	65
5.11	The effect of differential reddening towards the Bulge for the determination of photometric effective temperatures. We plot the variations in the A_{K_s} values for a set of 200 random positions in a $30'$ region towards $b = -4^\circ$ (black squares) and $b = -2^\circ$ (red circles), as obtained from the BEAM calculator, and compare them to variations in the photometric effective temperature.	67
5.12	Lower panels show the luminosity functions for a subfield in Baade's Window and at $b = -6$. The underlying RGB is fitted with a second order polynomial and the red clump is fitted with two Gaussians centered at $K_{s0} = 12.9$ and $K_{s0} = 13.2$ for $b = -6$ (right panels) and with a single Gaussian centered at $K_{s0} = 12.9$ for Baade's Window (left panels). Upper panels show the corresponding CMD for each field, oriented with color along the y-axis and magnitude along the x-axis. Density contours denote the single and double RC in each field. The second gaussian component in BW field is due to the RGB bump.	69

6.1	K-band extinction map in Galactic coordinates showing the fields analyzed in this study. The 28 VVV tiles cover ranges of longitude $-10^\circ < l < 10^\circ$ and of latitude $-1.4^\circ < b < -0.4^\circ$ and $0.7^\circ < b < 1.7^\circ$	72
6.2	$K_{s,0}$ luminosity functions for representative fields at $b = -1^\circ$ (left panels) and $b = +1^\circ$ (right panels). The red solid line shows the best fit to each distribution while the dashed line shows the individual Gaussian fits to the RC and to the additional peak when detected.	75
6.3	Position of the Galactic bar with respect to the Sun as measured with the RC method assuming a mean RC magnitude of $M_K = -1.55$. Red and black filled circles show the results for VVV data at latitudes $b = -1^\circ$ and $b = +1^\circ$, respectively. Solid lines show the distance spread along each line of sight correcting for an intrinsic bulge dispersion of 0.17 mag and photometric errors. Black open squares are the results from N05 at $b = +1$. Dashed lines represent the observed orientation angles for true orientations of 15° , 30° , and 45° following Stanek et al. (1994). Dotted lines show the lines of sight for longitudes $l = \pm 5$ and $l \pm 10$	77
6.4	Position of the Galactic bar with respect to the Sun as measured with the RC method from the the dereddened K_s magnitudes using our extinction map (red filled circles) at a latitude of $b = -5^\circ$. Also shown, are the measurements from the Galactic model as presented in Gerhard & Martinez-Valpuesta (2012) at the same latitude, corresponding to a bar with an angle of 25° with respect to the Sun-Galactic center line of sight (black empty squares). Dotted lines mark the lines of sight for longitudes $l = \pm 5^\circ$ and $l = \pm 10^\circ$	79
7.1	<i>Left panels:</i> Comparison of the photometric (hashed histogram) and spectroscopic (red dotted histogram) MDFs along the Bulge minor axis at $b = -4^\circ$, -6° and -8° . The average $[\text{Fe}/\text{H}]$ and dispersion σ_s are also shown for all MDFs. <i>Right panels:</i> CMDs in the absolute plane of the fields located along the minor axis at $b = -4^\circ$, -6° and -8° with overplotted the empirical RGB templates. Thick black circles refer to the stars used to derive the photometric MDFs.	84
7.2	Map of the mean values of the metallicity distributions for the complete region of the Bulge covered by the VVV survey.	86

List of Tables

3.1	Galactic coordinates of bulge fields. Extinction values and number of stars analyzed in each field are also listed.	16
3.2	Atomic linelist for Ca, Mg, Ti and Si used in this work. Also listed are the excitation potential (χ_{ex}) and oscillator strength ($\log gf$) for each analysed line.	19
3.3	Abundances of the Sun, Arcturus and μ -Leonis, obtained by comparison to synthetic spectra, as well as reference solar abundances from Asplund et al. (2009). The last two rows show the zero point abundances adopted by AB10 and our mean abundances measured for those same disk giants to which they refer.	20
3.4	Mg, Ca, Ti and Si abundances for stars in the four bulge fields. Metallicities are those presented in Z08 and listed here for reference. The full table is available in Appendix B.	29
3.5	Best fit parameters for linear ($a+m[\text{Fe}/\text{H}]$) trends for [$\langle \text{Mg}, \text{Ca}, \text{Ti}, \text{Si} \rangle / \text{Fe}$] abundances in the bulge and thick disk.	36
6.1	Listed are the mean dereddened (K_{s_0}), sigma (σ) and peak of the Gaussian used to fit the RC in each one of the tiles. $K_{s_{0,2}}$, peak_2 and σ_2 are the parameters used fo fit the secondary peak.	76
A.1	Full table listing Mg, Ca, Ti and Si abundances for stars in the four bulge fields. Metallicities are those presented in Z08 and listed here for reference.	91
A.1	continued.	92
A.1	continued.	93
A.1	continued.	94
A.1	continued.	95
A.1	continued.	96
A.1	continued.	97
A.1	continued.	98
A.1	continued.	99
A.1	continued.	100
A.1	continued.	101
A.1	continued.	102
A.1	continued.	103
A.1	continued.	104

A.1 continued.	105
A.1 continued.	106
A.1 continued.	107
B.1 VVV Tile centres for the Galactic bulge region.	109
B.1 continued.	110
B.1 continued.	111
B.1 continued.	112
B.1 continued.	113
B.1 continued.	114

Summary

The Milky Way bulge is the nearest galactic bulge and the best laboratory for studies of stellar populations in spheroids based on individual stellar abundances and kinematics. The observed properties point to a very complex nature, which is hard to extrapolate from a few fields. The global studies are challenged by the strongly variable and often large extinction on a small spatial scale.

We present the analysis of the $[\alpha/\text{Fe}]$ abundance ratios for a large number of stars at several locations in the Milky Way bulge with the aim of constraining its formation scenario. We observe an alpha-enhanced metal-poor component chemically indistinguishable from the thick disk which hints for a fast and early formation for both the bulge and the thick disk. This component shows no variation, neither in abundances nor kinematics, in the studied bulge regions. A metal-rich component showing low $[\alpha/\text{Fe}]$, similar to that of the thin disk, disappears at larger latitudes. This component has bar-like kinematics.

We present a method to obtain reddening maps and to trace structure and metallicity gradients of the bulge using data from the recently started ESO public survey Vista Variables in the Via Lactea (VVV). The method is used to derive properties of the stars across the complete region covered by the survey. We derive the reddening map on a small enough scale to minimize the problems arising from differential extinction. The reddening determination is sensitive to small scale variations which are clearly visible in our maps. Our results are in agreement within the errors with literature values based on different methods, although our maps have much higher resolution and more complete coverage. The dereddened magnitudes are used to build the bulge luminosity functions which are then used as distance indicator in order to trace the bulge structure.

Finally, for each subfield the derived distance and extinction values have been used to obtain photometric metallicities through interpolation of red giant branch colors on a set of empirical ridge lines. The photometric metallicity distributions are compared to metallicity distributions obtained from high resolution spectroscopy in the same regions. This allows us to investigate, for the first time, the general picture of the Bulge metallicity gradients and to trace a component formed through fast early mergers and a bar component formed on a more extended timescale.

Zusammenfassung

Die Bulge unserer Milchstraße ist die nächste ihrer Art und damit ein hervorragend geeignetes Objekt, um Sternpopulationen in Spheroiden anhand ihrer Elementhäufigkeiten und Sternbewegungen zu untersuchen. Die Beobachtungen lassen auf hohe Komplexität schließen, welche nicht durch punktuelle Untersuchungen erfasst werden kann. Die Aussagefähigkeit aller bisheriger Studien leidet erheblich an der Höhe und ausgeprägten Variabilität der Extinktionen.

Im ersten Teil dieser Arbeit untersuchten wir die Häufigkeiten sogenannter Alpha Elemente ($[\alpha/Fe]$) in einer Vielzahl von Sternen in der Bulge. Diese Elemente entstehen hauptsächlich in Supernovaexplosionen und lassen uns Rückschlüsse auf die Entstehungsgeschichte der Bulge ziehen. Dabei entdeckten und unterschieden wir zwei Populationen. Die erste, metallarme Population weist erhöhte Werte in der Alpha-Häufigkeit auf und ist in allen Eigenschaften nicht von dicken Scheiben der Milchstraße zu unterscheiden. Das lässt auf eine schnelle und simultane Entstehung der dicken Scheibe und dieser Komponente der Bulge schließen. Die Arbeit zeigt des Weiteren, dass es keine Variationen in Elementhäufigkeiten und Kinematik im gesamten untersuchten Bereich der Bulge für diese Komponente gibt. Die Geometrie scheint sphärisch zu sein. Die zweite Population gleicht eher einem inneren Balken, wie man ihn oft in entfernten Galaxien beobachtet und ist, ähnlich der dünnen Scheibe der Milchstraße, viel metalreicher als die erste Komponente. Sie weist geringe Alpha-Werte auf und scheint stärker auf die Ebene der Scheibe konzentriert zu sein, während die sphärische Komponente in allen Richtungen gleich stark ausgeprägt ist.

Ein weiterer Hauptbestandteil dieser Arbeit bestand in der Entwicklung einer Methode, die detaillierter Rötungskarten für den inneren Bereich der Bulge erzeugt. Diese Karten ermöglichen es, die innere Struktur und Gradienten in Metalizitäten zu entschlüsseln. Dafür verwendeten wir Beobachtungsdaten der ESO Survey 'Vista Variables in the Via Lactea' (VVV) welche vom Vista Teleskop der Europäischen Südsternwarte (ESO) über die letzten Jahre gesammelt wurden. Die Rötungskarten wurden in einer sehr hohen räumlichen Auflösung erstellt, sodass auch kleinste Variationen in der Extinktion erfasst werden können. Die Ergebnisse stimmen gut mit Literaturwerten überein, welche mit unterschiedlichen Methoden auf verschiedene Gebiete der Bulge angewandt wurden. Unsere Karten sind im Hinblick auf Rötung und Extraktion jedoch die bis heute vollständigsten und verfügen über die höchste Auflösung. Mithilfe dieser Karten gelang es uns, die Helligkeiten aller Sterne zu korrigieren und anhand ihrer Leuchtkraftfunktionen auf ihre Entfernung zu schließen. Dies erlaubt Rückschlüsse auf die räumliche und geometrische Beschaffenheit der Bulge.

Schließlich wurden die ermittelten Werte für Extinktion und Entfernung in jedem Unterge-

biet der Beobachtungen genutzt um photometrische Metallizitäten zu berechnen. Diese Werte wurden mit Ergebnissen von spektralen Messungen hochauflösender Instrumente verglichen und stimmen gut überein. Mithilfe dieser umfangreichen und vollständigen Metallizitätskarte ist es uns zum ersten Mal möglich, Variationen und Gradienten der Metallizitäten in der Bulge zu untersuchen und die Geheimnisse um ihre Entstehung und Entwicklung zu entschlüsseln.

Chapter 1

The Milky Way bulge in the general context of galactic bulges

Nearly 25% of the visible light emitted from stars in the local universe comes from bulges embedded in galactic disks (Fukugita et al. 1998). How are these bulges formed? and What is their connection with the formation and evolution process of their host galaxy? These fundamental questions need to be answered by obtaining an accurate characterization of the central structures of galaxies.

The current picture seems to be complicated, as recent observations suggest that bulges may be an in-homogeneous class of objects, each of them holding a different formation history (e.g. Athanassoula 2005). The early view of these components was rather intuitive since, in the hierarchical scenario of galaxy formation, it was natural to consider the central, spheroidal concentration of stars in a spiral galaxy as scaled down counterparts of elliptical galaxies. The (minor) merger history of spiral galaxies in the early universe is expected to trigger one or more starburst events (Weinzirl et al. 2009; Hopkins et al. 2010) which would rapidly form stars in its center, in a similar way to early-type galaxies. The structural, kinematical and stellar population properties of the resulting central component, as seen today, are expected to characterize a spheroidal system with hot kinematics (supported by velocity dispersion) of mainly old stars, known as *classical bulges*.

However, evidence for a much more complex nature of bulges has been found. Secular evolution processes due to instabilities in the disk of spiral galaxies result in the formation of a central bar (Combes & Sanders 1981; Weinberg 1985; Debattista & Sellwood 1998; Athanassoula & Misiriotis 2002). The presence of the bar has also strong influence on the distribution of gas within the disk, favoring the infall of gas content into the very central regions of the galaxy which ends in the formation of young central disks, or so called *pseudo-bulges* (see Kormendy & Kennicutt 2004, for a review on secular evolution and pseudo-bulges). Contrary to those of classical bulges, pseudo-bulges hold a majority of young stars and are rotationally supported.

Moreover, vertical instabilities in bars produce a buckling process which significantly increases the thickness of the bar which, when seen edge-on, appear boxy, peanut or even X-shaped (e.g. Bureau et al. 2006). These type of bulges are nothing more than bars which have suffered the effect of vertical heating in the orbits of their stars (Athanassoula 2005; Debattista et al.

2005; Martinez-Valpuesta et al. 2006; Wozniak & Michel-Dansac 2009). However, since they are formed as a product of the secular evolution of the disk, boxy-bulges are often also referred to as pseudo-bulges in the literature.

With the exception of the Milky Way and M31 (Jablonka & Sarajedini 2005), the observational studies of the central components of galaxies is strongly challenged by the impossibility to resolve individual stars due to crowding and blending in high stellar density regions of distant galaxies. In this context, the Milky Way bulge, one of the major components of the Galaxy, can be studied at a unique level of detail, in comparison to those of external galaxies, thanks to its resolved stellar populations which hold the imprints of how our Galaxy formed and evolved. Thus, a better understanding of the Milky Way bulge will provide solid constraints to interpret observations of extragalactic bulges as well as for detailed galaxy formation models. However, to obtain a complete characterization of the Bulge is not straightforward. A large coverage is required in order to study its global properties. Observations in discrete Bulge regions, less affected by extinction, have recently been found not to be representative due to an apparently very complex Bulge nature.

This chapter first introduces the reader into the different types of bulges and their main observational properties. It later describes our current knowledge of the Milky Way bulge, its place in the picture of the different formation scenarios, and the open questions to be addressed in the following chapters of this thesis.

1.1 An overview of galactic bulges

Here we summarize some of the observational properties of galactic bulges, which are normally investigated in order to characterize their origin and evolution.

- Light profile: The Sersic law is used to describe the relation between brightness (I) as a function of radius (R) of the galaxy in the form:

$$I(R) \propto e^{-\alpha R^{1/n}} \quad (1.1)$$

The larger the n value, the more centrally concentrated the profile. Light profiles of disk galaxies hosting a classical bulge are well fitted by a de-composition of a Vaucouleurs-like bulge ($n=4$) and exponential disk ($n=1$) (Gadotti 2009; Lackner & Gunn 2012, and references therein).

- Kinematics: The kinematic information for bulges comes mostly from the analysis of radial velocity information. This provides a measurement of both rotation velocity (V_{rot}) and the velocity dispersion (σ_v) along a given line of sight (Kormendy & Illingworth 1982). Important information for the characterization of bulges arises from the study of the velocity profiles at different scale heights from the plane. When rotational velocity does not change with height, it is referred to as *cylindrical rotation*.

- The analysis of stellar population in extragalactic bulges has been obtained from correlations between the measurement of integrated color index and age. Redder integrated colors are used as tracer of older populations while bluer colors should trace younger stars. However, this technique suffers the strong effects of age-metallicity degeneracy and extinction problems towards the inner regions of the galaxies, and has therefore been superseded by the spectroscopic measurements. Line strength indices, (H, Fe5015, Mg b, Fe5270, Fe5335 and Fe5406) in the Lick/IDS system (Burstein et al. 1984; Worthey et al. 1994; Trager et al. 1998), have been used in large sample of galaxies to study their stellar populations. They can be used as indicators of metallicity and age, breaking the degeneracy between these two factors present in integrated color techniques (Jablonka et al. 2007; Peletier et al. 2007; Cappellari et al. 2011; Williams et al. 2011).
- Stellar abundances: The connection between metallicity ($[\text{Fe}/\text{H}]$) and alpha element over iron abundance ratio ($[\alpha/\text{Fe}]$) provides constraints for the formation timescale of the Bulge (a more detailed explanation is given in Sect. 2.3). A high value of the $[\alpha/\text{Fe}]$ ratio is an indication of a fast formation scenario with a chemical enrichment dominated by the contribution of core collapse supernovae. On a more extended time-scale, SNIa explosions enrich the interstellar medium mostly with iron peak elements, and therefore new generations of stars will show a lower $[\alpha/\text{Fe}]$. The behavior of the $[\alpha/\text{Fe}]$ ratio in the Bulge can be also compared to that of other Galactic components to investigate connections between their formation timescales.

In the sections 1.1.1 to 1.1.4, the observational characteristics of bulges with different origins are described. The Milky Way bulge characteristics are summarized at the end of this section.

1.1.1 Classical bulges

In the hierarchical scenario of galaxy formation, the early mass assembly of galaxies will be dominated by merger processes which favors the formation of spheroids (Toomre 1977). This violent and relatively fast process produces the present day elliptical galaxies. However, when the spheroids are accompanied by the (re-)growth of stellar disk (Kauffmann et al. 1999; Springel & Hernquist 2005), they receive the name of classical bulges.

Classical bulges are expected to share the same observational properties of elliptical galaxies. Their morphological and stellar population properties can be summarized as follows:

- Light profiles of classical bulges are well fitted by a Vaucouleurs-like profile with $n \sim 4$ (e.g. Gadotti 2009).
- As in the case of elliptical galaxies, classical bulges show hot dynamics ($V_{rot}/\sigma_V < 0.2$) dominated by velocity dispersion (e.g. Gadotti 2011). An important point is that this rotation is observed to be non-cylindrical, therefore showing a decrease in their rotation velocity at increasing height from the plane (e.g. Emsellem et al. 2004).



Figure 1.1: Color image of the Sombrero galaxy (M104), the prototypical example of a disk galaxy with a large classical, merger-built bulge in its center. Image was obtained directly from the ESO photo release eso0007 "Fine shades of a Sombrero" and was made by a combination of three CCD images from the FORS1 multi-mode instrument on VLT ANTU, by Peter Barthel from the Kapteyn Institute (Groningen, The Netherlands) during an observing run at the ESO Paranal Observatory.

- Since classical bulges are formed violently, in fast and early processes of collisions and mergers, stars in classical bulges are expected to have formed mostly from the starburst in the early times, with little or no star formation since then. For this reason, classical bulges are expected to be composed predominantly of old stars (~ 10 Gyr) (e.g. Renzini 1998).
- Like in the case of elliptical galaxies, bulges are not only dominated by old stellar populations but they have enhanced abundance ratios as a result of the early and fast burst of star formation (Peletier et al. 1999; Moorthy & Holtzman 2006; MacArthur et al. 2008). They also often show metallicity gradients, going from metal-poor stars in the outskirts to a more metal-rich population towards the center. (see for example Jablonka et al. 2007)

Fig. 1.1 shows the color image of the Sombrero galaxy. This is the typical example of an edge-on disk galaxy with a prominent classical bulge in the center.

1.1.2 Galactic bars and boxy-bulges

Given that the classical bulge formation scenario is connected to the rate of merger events, this is expected to be the dominant process in the evolution of galaxies at early times (Kormendy & Kennicutt 2004). Later on, secular evolution processes would become important, re-arranging stellar material from a settled galactic disk. Disk instabilities, such as the presence of spiral arms, are expected to induce the formation of bars in the inner regions of a galactic disk (Combes & Sanders 1981; Weinberg 1985; Debattista & Sellwood 1998; Athanassoula & Misiriotis 2002). Indeed, galactic bars are a very common phenomena, found in $\sim 60\%$ of spiral galaxies in the local Universe (e.g. Eskridge et al. 2000).

Although disks are thin galactic components, bars might become thicker because of the vertical resonances and buckle off the plane of the galaxy. For this reason, galaxies, when observed

edge-on, often show a central component which swells out of the disk with a boxy, peanut, or even an X-shape (e.g. Bureau et al. 2006; Patsis et al. 2002). These structures have been seen in numerous of simulations, as the result of the development of vertical instabilities that create such structures from the, initially thin, stellar bar (Athanasoula 2005; Debattista & Williams 2004; Debattista et al. 2006; Martinez-Valpuesta et al. 2006).

The dynamical and structural properties of boxy-bulges are well constrained from models and observations. However, its stellar populations are less clear than in the case of classical bulges. In fact, a variety of stellar populations are observed among bars (e.g. Gadotti & de Souza 2006; Pérez et al. 2009). In practice, since boxy-bulges are bars thickened by vertical instabilities, it would be natural to expect them to share the stellar populations of the original bar.

Some important properties of boxy-bulges can be summarized as follows:

- The brightness profiles of boxy-bulges are less centrally concentrated than those of classical bulges, therefore they are better fitted by light profiles with a lower sersic index (e.g. Kormendy & Bruzual A. 1978; Gadotti 2009).
- What is probably the most characteristic property of boxy-bulges is that they are observed to rotate cylindrical. This means that the rotation velocity within the boxy-bulge does not change with height above the galactic plane (e.g. Kormendy & Illingworth 1982; Combes et al. 1990; Athanasoula & Misiriotis 2002; Shen et al. 2010).
- Different stellar ages are observed among different bars. The null hypothesis would be that they should hold similar ages as their parent disks from which they formed. Similar case would be expected for the metallicity and alpha elements abundances. However, Freeman (2008) suggested that age and abundance gradients could still be present in boxy bulges. Older, more metal-poor stars would have more time to be scattered to larger distances from the plane by the buckling process, therefore establishing a negative metallicity and positive age gradient. The presence and strength of such gradients would then depend on the enrichment process of the disk material from which the bar forms and the timescale of the buckling instability to form the boxy-bulge.

Figure 1.2 shows the image of NGC4565, a good example of a boxy-bulge seen in an edge-on galaxy.

1.1.3 Pseudo-bulges

As described before, boxy-bulges are thickened bars, with bars being in fact disk phenomena resulting from internal processes of secular evolution. The absence of an external factor in the formation process of boxy-bulges, as opposite to the classical bulge scenario, led different authors to refer to them as pseudo-bulges. This was also qualitatively supported by the pseudo-bulge definition in the review of Kormendy & Kennicutt (2004), where they describe: *'..if the component in question is very E-like we call it bulge, if its more disk-like, we call it pseudo-bulge'*. The morphology of thickened bars is certainly not E-like (Bureau et al. 2006), however, to avoid confusion during our analysis, we refer to them as boxy-bulges and not pseudo-bulges.

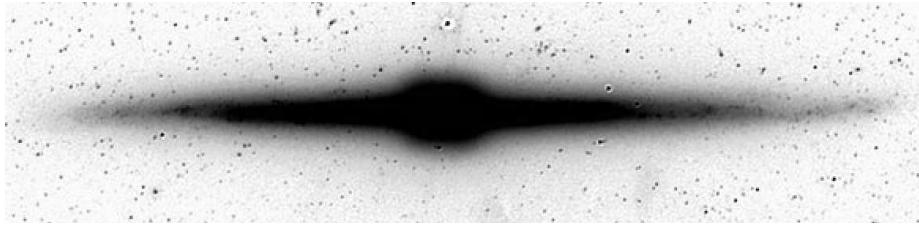


Figure 1.2: Spitzer/IRAC 3.6 m negative image of NGC 4565, taken from the work of Kormendy & Barentine (2010), showing a clear boxy-bulge structure in its center. This is panel a of Figure 2 from Kormendy & Barentine (2010), reproduced by permission of the AAS.

But then, what are these disk-like components in the center of disk galaxies, to which we refer as pseudo-bulges?

The presence of a central bar has important consequences for the subsequent evolution of the galaxy, redistributing the angular momentum and matter in the disk. In particular, it produces the loss of angular momentum of the molecular gas settled in the rotating disk, inducing its infall process into the inner regions of the galaxy. The slow gas fueling into the center, produces a slow star formation process that results in the formation of a disk-like component in these inner regions. We refer to these structures as pseudo-bulges.

Properties of pseudo-bulges are summarized here:

- Their brightness can be fitted with a very disk-like, exponential light profile and are observed as flat, rotation supported structures
- As a result of a very slow process of gas fueling into the center, because of the presence of the bar, the star formation is also slow and continuous. This results in pseudo-bulges having young stellar populations and being dominated by metal-rich stars with low alpha-element abundances as a result of the long timescale of star formation.

In Kormendy & Barentine (2010), a study of the inner regions of the galaxy NGC 4565 revealed a central disk-like component, inside the boxy-bulge shown in Fig. 1.2. The image of NGC 4565 used in Kormendy & Barentine (2010) is shown in Fig.1.3 as the example of a pseudo-bulge found in the center of barred galaxies.

1.1.4 Clump-origin bulges

The above scenarios for bulge formation and their properties have historically emerged from the observation of bulges in nearby galaxies. However, a new paradigm has recently emerged, mostly driven by the observations of galaxies at redshift ~ 2 , i.e., at a lookback time comparable to the ages seen in classical bulges. Such galaxies, for example, may offer examples of how our own Milky Way was looking like in its early days, prior to and during its bulge formation. At $z \sim 2$ a widespread population exists of large, rotating disk galaxies, with much higher gas fractions and velocity dispersion compared to local spirals (Genzel et al. 2006, 2008; Förster

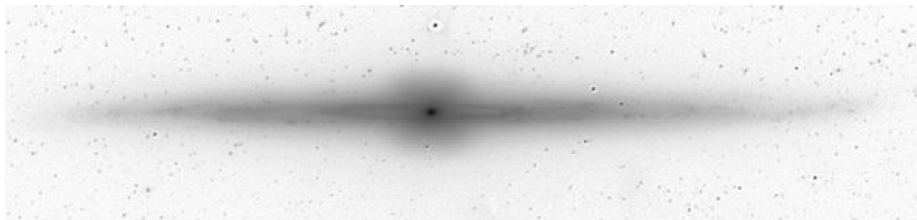


Figure 1.3: Spitzer/IRAC 3.6 μ m negative image of NGC 4565, using a contrast and brightness stretching to highlight its pseudobulge from the work of Kormendy & Barentine (2010). This is panel b of Figure 2 from Kormendy & Barentine (2010), reproduced by permission of the AAS

Schreiber et al. 2009; Tacconi et al. 2010; Daddi et al. 2010). Such gas-rich galaxies are prone to disk instabilities that can result in the formation of gas clumps which are large (> 1 kpc) and massive ($10^8 M_{\odot}$). These massive clumps will gravitationally interact and migrate to the center of the disk, resulting in bulge formation over timescales of a few 10^8 yr, much shorter than those typically ascribed to secular instabilities in local disk galaxies (Immeli et al. 2004; Carollo et al. 2007; Elmegreen et al. 2008).

Such rapid formation, partly due to the quasi-exponential mass growth experienced by these galaxies, quite naturally leads to an α -element enhancement in the resulting, old, stellar populations (Renzini 2009; Peng et al. 2010), that would apply both to the disk and bulge stars formed at these early cosmic epochs. Additionally, given the violent mechanism in which they are formed would result in a morphology and kinematics that resemble more those of classical bulges.

1.2 The Bulge of the Milky Way

Stellar populations properties of the Galactic bulge seem to support the scenario of a structure formed by violent process of mergers in early epochs, which ended up in a spheroid like, old, metal-rich population – in other words, as a *classical bulge*. However, we now have indications that the picture might be far more complicated. The consensus is that the bulk of the Bulge is old ($t \sim 10$ Gyr) with a metallicity distribution that extends from $[\text{Fe}/\text{H}] = -1.5$ to $[\text{Fe}/\text{H}] = 0.5$, with a peak at solar metallicity (Zoccali et al. 2003, 2008; Clarkson et al. 2008, and references therein) and that the formation of the Bulge was fast as evidenced by the enhanced α elements in Bulge stars (McWilliam & Rich 1994; Fulbright et al. 2006, 2007; Zoccali et al. 2006; Lecureur et al. 2007). Therefore, the conclusions so far regarding age, metallicity and chemical enrichment in the Bulge point to a formation scenario similar to that of early-type galaxies. Even more, the existence of a metallicity gradient in the Bulge, as shown by Zoccali et al. (2008) strongly supports this classical bulge scenario.

On the other hand, a different formation history for the Bulge might be interpreted by morphological signatures and some recent chemical abundance studies. Using a sample of high resolution spectra for disk and Bulge giants, Meléndez et al. (2008) finds a similarity between the oxygen over iron ratio of the bulge and the thick disk, both enhanced when compared to the

thin disk. Later on, Alves-Brito et al. (2010) reaches the same conclusions when analyzing other α -elements from the sample of Meléndez et al. (2008). These results are in contrast to some previous studies. However, since these previous studies were done comparing Bulge giants to local disk dwarfs from other works using in-homogeneous literature measurement compilations (e.g. Fulbright et al. 2006; Zoccali et al. 2006; Lecureur et al. 2007), Meléndez et al. (2008) claims that differences between thick disk and Bulge stars might be explained by systematic errors when comparing dwarfs to giants or relative calibrations between those works. If the similarity between the Bulge and thick disk is confirmed with a larger sample, this could be a strong evidence for a different formation scenario for the inner parts of the galaxy, in which thick disk and Bulge share a similar chemical evolution history and the latter might have been formed from inner disk stars. However, it is important to recall that, as long as a significantly large sample of inner disk stars is not available, a final conclusion will be hard to accomplish.

In terms of morphology, the evidences for a barred structure in the Milky Way are numerous. Red clump stars distributions from photometric surveys have established the existence of a bar inclined with respect to the Sun–Galactic center line of sight with its near end towards positive longitudes (Stanek et al. 1994; Rattenbury et al. 2007; Cabrera-Lavers et al. 2007). Observations of the bulge are usually modeled with a triaxial bulge with a position angle of ~ 15 -30 degrees and nearly 2.5 kpc in length (e.g. Babusiaux & Gilmore 2005; Rattenbury et al. 2007). Furthermore, the near-IR COBE/DIRBE image provided clear evidence for boxy-peanut shaped Milky Way bulge (Weiland et al. 1994). Howard et al. (2009) analyzed the kinematics of the bulge concluding that the dynamical signature of the stars at high latitudes ($b = -8^\circ$) is the same as that in fields closer to the galactic plane ($b = -4^\circ$), therefore showing evidence for cylindrical rotation *as expected for boxy bulges*. Their data lack evidence indicative of an accretion origin of bulge in contrast with the claims of tidal streams in kinematics and metallicity from Rangwala et al. (2009). Moreover their cylindrical rotation signal was modeled by Shen et al. (2010) without any need for a classical component.

Did the bar form from inner disk stars which then buckled and formed the boxy bulge we see today? Did secular evolution form a younger pseudo-bulge in the inner regions? Were merger histories in the galaxy able to produce a classical bulge within the central part of the galaxy?

There has been evidence, from both observations and models, that different types of bulges could coexist in the same galaxy (Samland & Gerhard 2003; Nakasato & Nomoto 2003; Kormendy & Kennicutt 2004; Peletier et al. 2007). If this is the case, we might have a very complex structure in the bulge, with two or more components partially overlapping. *Could this be the case of the Milky Way bulge?*

Suggestive evidence for a dual nature of our bulge started to emerge from chemical abundances and kinematic studies. Indication for bimodality in the metallicity distribution has been found from red clump stars in Baade’s Window (Hill et al. 2011). The two components seem to have also different kinematics (Babusiaux et al. 2010) which is consistent with different structures present in the bulge: a metal-rich component with bar-like kinematics and a metal-poor one showing kinematics of a spheroidal component.

The picture is further complicated by the recent finding of a double peaked red clump along the minor axis, at both positive and negative latitudes, but only for $|b| > 6^\circ$. The double clump is clearly visible in several color magnitude diagrams available in the literature (e.g. Zoccali et al.

2003; Rattenbury et al. 2007; McWilliam & Zoccali 2010; Nataf et al. 2010; Saito et al. 2011). Such a feature has been interpreted as two components at different distances and is likely to be the observational signature of X-shaped bulge (McWilliam & Zoccali 2010; Saito et al. 2011).

All these observational evidences support a very complex structure of the Bulge, with two or more distinct components partially overlapping. Signatures of the different formation histories for these components, should still remain in bulge stars.

Therefore, a homogeneous study, based on a large photometric and spectroscopic coverage, is the key to make further progress in our understanding of the Milky Way bulge stellar populations and structure. This is the main scientific goal of this thesis.

Chapter 2

Stellar abundances as tracers of formation history

The atmospheres of stars act as fossils of the history of processes underwent by the material from which the stars were formed. This history is imprinted in their chemical composition, which can be studied in detail through the measurement of strength of spectral lines. The basic parameters of a star can be measured by building a detailed model atmosphere to reproduce particular features of the observed spectrum. Once this model is constructed with the appropriate parameters, it can be used to measure the abundances of specific elements in the stellar atmosphere.

Stellar parameters and chemical abundances can be obtained from a variety of techniques, depending on how much information one has about the source. For this reason, we will limit our description to the case of giant stars in the Bulge. As Bulge stars are located ~ 8 kpc from the Sun and are often heavily extinguished, dwarf stars are too faint ($V \sim 20$, for a low extinction region) for the systematic high-resolution spectroscopic studies necessary to derive accurate abundances. In this chapter, we introduce the basics of the determination of stellar parameter and abundances in giant, brighter, stars and how we use them to understand the formation history of the Galactic bulge.

2.1 The chemical composition of stars

We can consider the Sun to be an example of a typical star. The Sun is composed of roughly 91.2% hydrogen and 8.7% helium of the total atoms. The remaining $\sim 0.1\%$ of the elements in the atmosphere of the Sun, are referred to as *metals*. Most of these heavier elements are synthesized in the stellar interior by a process called *nucleosynthesis*. Once a star is in the last stages of its evolution, metals are partially expelled to the interstellar medium by a number of mass loss episodes and, in particular cases, as a supernovae explosion. For this reason, in any given star, the amount of metals present in its atmosphere will vary from 0.1% to 0.01%, depending on how enriched by these heavier elements was the molecular cloud from which the star was born.

The abundance of a given element X in a stellar atmosphere, $A(X)$, is often quantified rela-

tively to the abundance of hydrogen, on a logarithmic scale:

$$A(X) = \log(N(x)/N(H)) + 12 \quad (2.1)$$

where $N(X)$ is the number density of the element. In particular, the abundance of iron is used as a reference of the amount of metals in a star. When the iron abundance of a star is measured relative to that of the Sun, it is defined as the 'metallicity' of the star. This quantity is denoted as $[Fe/H]$ and its calculated as:

$$[Fe/H] = A(Fe)_{\text{star}} - A(Fe)_{\text{sun}} = \log(N(Fe)/N(H))_{\text{star}} - \log(N(Fe)/N(H))_{\text{sun}} \quad (2.2)$$

The iron abundance and abundances of other elements can be directly measured spectroscopically. The more abundant the element is in the atmosphere, the stronger the absorption line profile will be. However, the absorption line profile will also be affected by the stellar temperature, surface gravity and microturbulence velocity profile. Therefore, to derive stellar abundances, correct determination of the stellar parameters and the construction of a model of the stellar atmosphere are required.

2.2 Model atmospheres and abundance measurements

The elemental abundances in stars can be derived by comparing a model atmosphere with the observed spectrum of a star. To construct the model atmosphere, the following stellar parameters must be determined: i) the effective temperature T_{eff} , describing the typical temperature of the outer photospheric layers from which the radiation is emitted, ii) the surface gravity $\log g$ related to the mass and radius of the star, iii) the microturbulence velocity ξ which describes the broadening of the stellar lines due to the turbulent gas motions in the atmosphere, and finally iv) the metallicity $[Fe/H]$ of the star.

A first guess of the parameters of Bulge giant stars can be obtained from photometry. An estimation of T_{eff} can be derived from calibrations between the stellar color and its temperature (Alonso et al. 1999; Ramírez & Meléndez 2005), while other parameters can be derived by assuming a distance to the star and deriving its corresponding bolometric magnitudes. The accuracy of these photometric values will depend mostly on how well constrained is the distance to the star, and on the use of correct extinction values due the dust along the line of sight (see Chapter 5). Unfortunately, individual distances for Bulge giant stars cannot be determined accurately and photometric stellar parameters require a refinement done through the analysis of the stellar spectra. To do this, a first guess model atmosphere must be created using the photometrically determined parameters.

The next step is the determination of the Equivalent Width (EW) of Fe lines. The EW is the width of a rectangular surface, with the same area as the line profile, measured from the level of the continuum and is therefore an indicator of the strength of a given spectral line. This technique can only be applied over lines not suffering from severe blending with other features, thus a careful selection of Fe lines over the spectral range should be carried.

Using the first guess model atmosphere a $[\text{Fe}/\text{H}]$ value can be derived for each EW obtained along the corresponding spectral range. This is done under the local thermal equilibrium (LTE) approximation where, for all elements, the number populations of different excitation levels is derived following the Boltzmann distribution and the Saha equation provides the corresponding relative ionization fractions.

The final T_{eff} can be then determined iteratively by requiring that the same $[\text{Fe}/\text{H}]$ is derived for lines with different excitation potential. This is referred to as imposing the excitation equilibrium on Fe I lines. Microturbulence velocity is constrained requiring that all lines with different EWs give the same FeI abundance. No trend in the $[\text{Fe}/\text{H}]$ abundance as a function of the EW of the lines should be observed. Finally, surface gravity is derived by requiring that the mean metallicity derived from FeI lines is the same as from FeII lines, in other words imposing ionization equilibrium. At each step of the iteration, a new model is created with the modified stellar parameters until all the conditions are fulfilled simultaneously. After the final model is computed, it can be used to compute a synthetic spectrum of each star, and different element abundances can be derived by comparison to the corresponding line profiles in the observed spectrum.

2.3 Alpha elements and the formation timescale

One key factor to discriminate between the different formation scenarios of a given stellar population is how fast the chemical enrichment process actually occurred. As described in Sect. 1, this becomes particularly important to discriminate between violent and secular formation scenarios for galactic bulges.

Elements produced by nucleosynthesis in the stellar interior can be returned to the interstellar medium (ISM), mainly via supernovae (SNe) explosions, so that a new generation of stars will hold this information in their atmospheres. By comparing the abundance of elements, that are produced and returned to the ISM in different timescales, one can derive the amount of time that passed since the star formation started. This is the case of the alpha-elements, produced in high-mass stars which quickly evolve into core-collapse SNe II, compared to iron, returned to the medium after the delayed onset of SN Ia explosions (Wyse & Gilmore 1988; Matteucci 2003).

Thus, in order to trace back the formation timescale of a given population, we focus on the two types of supernova explosions and their products into the interstellar medium. Core-collapse SNe II, as the result of the fast evolution of high-mass stars ($M > 8 M_{\odot}$), occur first in the galactic evolution scenario. They enrich the environment with both iron peak elements (V, Cr, Mn, Fe, Co and Ni), and the so-called alpha-elements (Ne, Mg, Si, S, Ar, Ca, Ti), with the later being synthesized by alpha-capture process in the precursor state of SNe II (Matteucci & Greggio 1986). On the other hand, the timescale in which the different channels of SN Ia events (Greggio 2010) are produced is longer (> 1 Gyr) and will return mostly iron peak elements into the environment. New generations of stars will have larger metallicities as a result of the enrichment produced by SNe II in the early stages and by the subsequent SN Ia explosions (e.g. Matteucci & Greggio 1986). Therefore, within the context of galactic evolution, we can then consider $[\text{Fe}/\text{H}]$ as an indicator of time.

The ratio between the alpha-element abundance and metallicity is defined as the difference

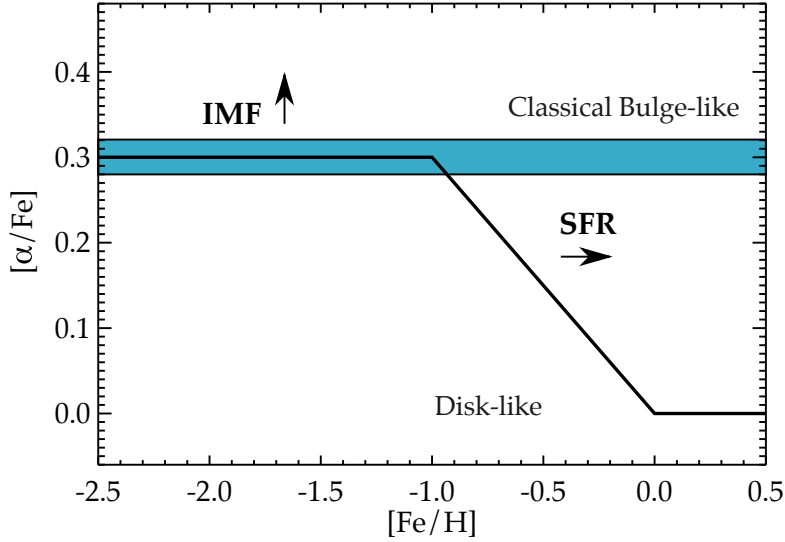


Figure 2.1: Illustration of the $[\alpha/\text{Fe}]$ ratio versus metallicity trends expected for a classical bulge population formed on a short timescale and the drop produced by the contribution of SN Ia during a more extended process. The absolute values of these trends depend on the IMF and the SFR of the population.

between the abundance of a given alpha-element in a star and that of the Sun, using Fe as reference, such that:

$$[\alpha/\text{Fe}] = A(\alpha)_{\text{star}} - A(\alpha)_{\text{sun}} = \log(N(\alpha)/N(\text{Fe}))_{\text{star}} - \log(N(\alpha)/N(\text{Fe}))_{\text{sun}} \quad (2.3)$$

and indicates the contribution of SNe II, as a rather constant value with metallicity (plateau), and the delayed contribution of SN Ia observed as a decrease in the $[\alpha/\text{Fe}]$ ratio.

The absolute value of the, alpha-enhanced, classical bulge-like plateau will depend on the distribution of masses of the newly formed stellar population, referred to as the initial mass function (IMF), while the metallicity at which the $[\alpha/\text{Fe}]$ ratio drop starts depends on its star formation rate (SFR). We can study these trends, as shown in Fig. 2.1, and use it to assess the star formation history of a given population.

A bulge-like population, corresponding to the classical bulge scenario, is characterized by a violent and fast formation process, which is therefore dominated by the contribution of SNe II (Wyse & Gilmore 1988). Most of its stars are formed before the onset of SN Ia occurs, such that the $[\alpha/\text{Fe}]$ ratio remains constant over metallicity (time). On the other hand, a disk-like population will be formed on a more extended timescale, where SN Ia contribution becomes important, and the $[\alpha/\text{Fe}]$ ratio drops down to solar values. This is one of the most important plots in galactic chemical evolution studies, and we use it in the following chapter to investigate the formation timescale of the Bulge and compare it to the disk component of the Milky Way.

Chapter 3

The formation timescale of the Galactic bulge from alpha-element abundance measurements and gradients

As described in Sect. 1.2., the presence of the bar in the central parts of the Galaxy is well established from several studies (e.g. Stanek et al. 1997). The detailed mapping of a double red clump (RC) feature in the luminosity function of the outer bulge regions from McWilliam & Zoccali (2010), interpreted as two over-densities at different distances, led to the conclusion that the Bulge is actually an X-shaped bar. In addition, the kinematic Brava survey (Shen et al. 2010), found no evidence for the existence of an additional spheroidal component.

In contrast to the above structure and kinematics studies, the combination of chemical abundances and kinematics suggests that there might be mixed populations in the Bulge. Hill et al. (2011) showed that, when looking at the metallicities derived from high resolution spectroscopy of RC giants in Baade's Window, and after producing an error deconvolution, the metallicity distribution appears to be bimodal, with a metal-poor and a metal-rich component. The known minor axis metallicity gradient (Zoccali et al. 2008; Johnson et al. 2011) would be then a result of the different contribution of these two populations at different latitudes. Babusiaux et al. (2010) showed that these two components have actually also distinct kinematics. In particular, based on accurate proper-motions and radial velocities, they concluded that the vertex deviation of the velocity ellipsoid is consistent with a metal-poor component showing spheroid kinematics and a metal-rich with bar-like kinematics.

To investigate further these results, in this chapter we have used a large sample of 650 FLAMES-GIRAFFE spectra to analyze the α -element distribution of giant stars in three fields along the minor axis and another at a larger galactic longitude. We use them to homogeneously compare with disk giant stars abundances and to investigate the presence of gradients within the bulge. These results are then discussed in the context of bulge formation theories.

Table 3.1: Galactic coordinates of bulge fields. Extinction values and number of stars analyzed in each field are also listed.

N	Name	l°	b°	E(B-V)	stars
1	Baade's Window	1.14	-4.18	0.55	194
2	$b = -6^\circ$	0.21	-6.02	0.48	194
3	Blanco field	0.00	-12.0	0.20	86
4	NGC 6553	5.25	-3.02	0.70	176

3.1 The sample

The bulge spectra discussed here belong to the same sample presented in Zoccali et al. (2008, hereafter Z08) as part of a project aimed to provide a spectroscopic characterization of the Galactic bulge. The sample consists of spectra of 650 K giant stars obtained with the FLAMES-GIRAFFE spectrograph (Pasquini et al. 2003) using the HR13, HR14 and HR15 setups (6100-7000Å) at a resolution of $R \sim 20,000$. For the present analysis we have only used the HR13 setup ($R=22,500$) in which we have lines for all the analyzed elements. As described in Z08, the S/N of our sample ranges from 40 to 90. Details on the fields analyzed here are presented in Table 3.1. In the last column of Table 3.1 we list the number of stars for which we were able to measure abundances for Ca, Mg, Ti and Si. These are only those spectra that had sufficient S/N (>50) for all the elements to be measured and did not present very large FWHM which could affect the results due to line blending. The sample also contains target stars which belong to bulge globular clusters: NGC 6522 in Baade's Window (7 stars), NGC 6558 in the field at $b=-6^\circ$ (3 stars) and NGC 6553 in the eponymous field (29 stars). These stars were classified as cluster members by Z08 based on the following criteria: $[\text{Fe}/\text{H}]$ within 0.2 dex and radial velocity within ± 10 km/s of the mean for the cluster, and a location within 2 arcmin from the cluster center.

Magnitudes and astrometry for this sample come from the OGLE catalog for Baade's Window and from WFI images for the field at $b=-6^\circ$, $b=-12^\circ$ and NGC6553 (see Z08 for a detailed description). Selected targets are nearly 1 mag above the red clump as shown in Fig 3.1.

The sample for thick and thin disk RGB stars in the local neighborhood consists of the same spectra analyzed in Meléndez et al. (2008) and Alves-Brito et al. (2010, hereafter AB10). Stars belong to a range of effective temperatures of $3800 < T_{eff} < 5000$ K and metallicities $-1.5 < [\text{Fe}/\text{H}] < 0.5$, making this sample ideal to compare with our bulge sample. Spectra were taken with different spectrographs, MIKE ($R \sim 65,000$) mounted on the Clay 6.5m Magellan telescope, the 2dcoude ($R \sim 60,000$) spectrograph on the 2.7m Harlan J. Smith telescope at McDonald Observatory, HIRES ($R \sim 100,000$) on the Keck I 10m telescope and complemented with spectra from the ELODIE archive ($R \sim 42,000$). Population membership and data reduction is described in AB10. Population membership for the bulge sample is described in Z08.

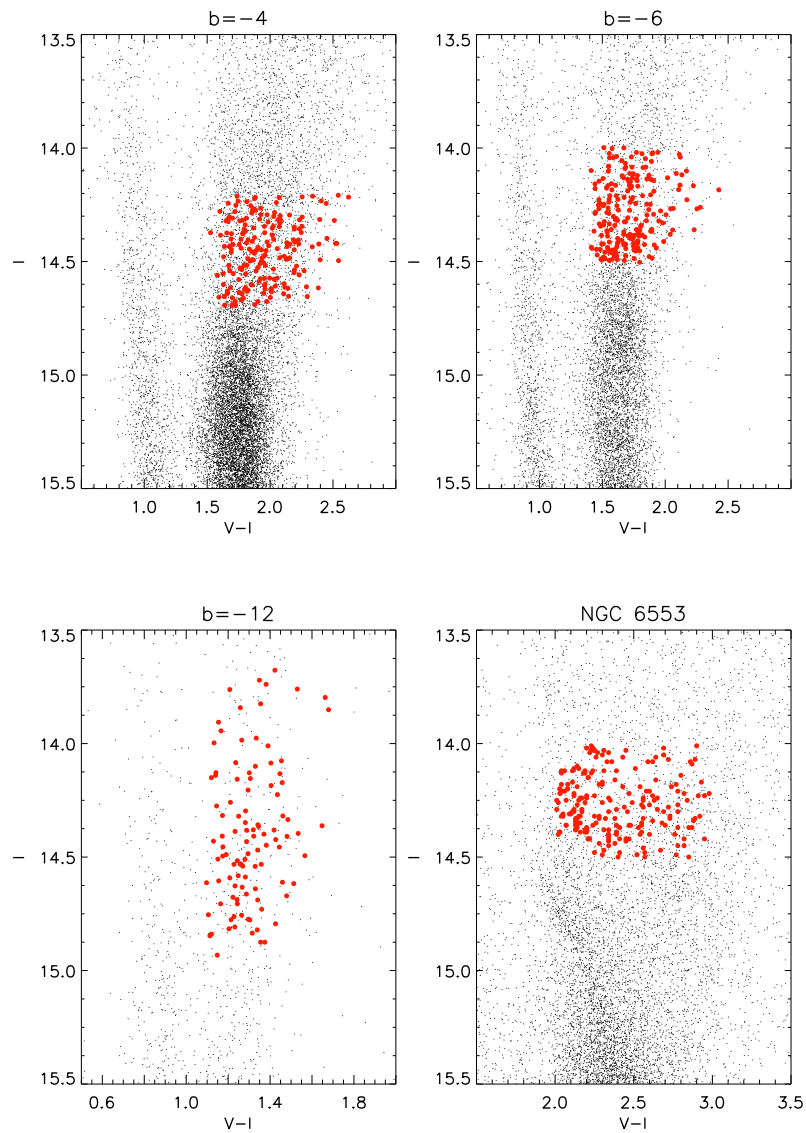


Figure 3.1: Color magnitude diagrams for the four fields: Baade's window (*upper left*), $b = -6^\circ$ (*upper right*), $b = -12^\circ$ (*lower left*) and NGC6553 (*lower right*). Spectroscopic targets in each field are marked as large filled circles. Magnitudes were obtained from the OGLE catalogue (Udalski et al. 2002) and the Z08 catalog obtained from WFI images

3.2 Stellar parameters

For bulge stars we have adopted the same stellar parameters, effective temperature (T_{eff}), surface gravity ($\log g$), microturbulence velocity (ξ) and metallicity $[\text{Fe}/\text{H}]$ presented in Z08 and we refer the reader to that work for a detailed description of the procedure. In order to perform a differential analysis when comparing bulge and disk stars, we followed the same procedure from Z08 to determine parameters of the disk sample. We have used the same iron linelist from Z08 based on calibrated $\log gf$ values to match the observed spectra of the metal-rich giant μ -Leonis. Only small difference is that as first input value for T_{eff} we used photometric values obtained from the calibration provided by Alonso et al. (1999) as opposed to the Ramírez & Meléndez (2005) calibration adopted by Z08. T_{eff} values were then refined spectroscopically by imposing excitation equilibrium between FeI lines therefore removing any dependence on the adopted calibration. Microturbulence velocity ξ was calculated by requiring the same $[\text{Fe}/\text{H}]$ for all equivalent widths of FeI lines. Surface gravity was determined photometrically using the following equation:

$$\log(g) = \log(g_{\odot}) + \log\left(\frac{M_{*}}{M_{\odot}}\right) + 0.4(M_{\text{Bol},*} - M_{\text{Bol},\odot}) + 4 \log\left(\frac{T_{\text{eff},*}}{T_{\text{eff},\odot}}\right) \quad (3.1)$$

where for the Sun we have used the same values used by Zoccali et al. (2008): bolometric magnitude $M_{\text{Bol},\odot} = 4.72$ mag, effective temperature $T_{\text{eff},\odot} = 5770$ K and surface gravity $\log(g_{\odot}) = 4.44$ dex. We have adopted the masses from AB10 which are based on Padova isochrones. Absolute visual magnitudes were obtained assuming distances from Hipparcos parallaxes. Finally, bolometric magnitudes were calculated by applying bolometric corrections from Alonso et al. (1999).

3.3 Abundance analysis

Mg, Ca, Ti and Si abundances were determined by comparing the observed spectra with synthetic ones created with MOOG (Snedden 1973). MOOG is a FORTRAN code that performs a spectral line analysis and spectrum synthesis assuming local thermal equilibrium. MARCS model atmospheres (Gustafsson et al. 2008) were used for our analysis. These models were created using the stellar parameters provided in Z08 for bulge stars, while for disk stars we used the stellar parameters determined as described in Section 3.2. We have used the same atomic line list from the analysis of bulge stars in Lecureur et al. (2007, hereafter L07). Unfortunately, the lower resolution of GIRAFFE compared to that of the UVES spectra of L07 prevents us to obtain accurate oxygen abundance measurements from the available OI line at 6300 Å.

The broad (~ 5 Å) autoionization Ca I line at 6318.1 Å affects the continuum of the Mg triplet as discussed in L07. Therefore, Ca abundances were determined first in our procedure and then this value was given as an input to determine Mg abundances. The CN line list from the same work was adopted and calibrated carefully as CN lines are known to be important for cool giant stars. The TiO molecular line list (Plez 1998) was also included. Reference solar abundances are from Asplund et al. (2009).

Table 3.2: Atomic linelist for Ca, Mg, Ti and Si used in this work. Also listed are the excitation potential (χ_{ex}) and oscillator strength ($\log gf$) for each analysed line.

λ (Å)	Element	χ_{ex}	$\log gf$
6318.71	MgI	5.110	-2.000
6319.23	MgI	5.110	-2.240
6319.49	MgI	5.110	-2.680
6166.43	CaI	2.521	-1.142
6169.04	CaI	2.523	-0.797
6169.56	CaI	2.526	-0.478
6312.23	TiII	1.460	-1.552
6142.49	SiII	5.620	-1.500

Although this is a differential analysis, in the sense that we determine the stellar parameters and perform the spectral analysis in the exact same way for all stars, it is important to provide abundances of some reference targets using our procedure, therefore establishing our “zero point” in order to be able to contrast our results with the values obtained in other works. For this reason we have also adopted the calibration procedure based on reproducing the observed spectrum of the Sun, Arcturus and μ -Leonis. We have used the optical spectra of these stars that were analyzed in L07 for the same purpose. μ -Leonis spectrum was taken at the Canada-France-Hawaii telescope with the ESPanDOnS spectropolarimeter at a resolution of 80,000. The Arcturus spectrum with a resolution of 120,000 comes from the UVES database (Bagnulo et al. 2003). Finally for the Sun we used a UVES optical spectrum¹. These spectra were convolved to the GIRAFFE resolution and compared with synthetic spectra in a region around the Mg, Ca, Ti, and Si lines analyzed in this work. Table 3.2 shows the wavelength, excitation potential, and $\log gf$ of these lines. Model atmospheres were created adopting the same stellar parameters used in L07, $[\text{Fe}/\text{H}]=0.3$, $T_{\text{eff}}=4540$, $\xi=1.3$, $\log g=2.3$ for μ -Leonis, $[\text{Fe}/\text{H}]=-0.52$, $T_{\text{eff}}=4300$, $\xi=1.5$, $\log g=1.5$ for Arcturus and $T_{\text{eff}}=5770$, $\xi=0.9$, $\log g=4.42$ for the Sun. Figure 3.2 shows the comparison between the synthetic and observed spectra for these stars with the abundances listed in Table 3.3. For the Sun, we only required a 0.05 dex modification in Ca abundance with respect to our reference values of Asplund et al. (2009) also listed in Table 3.3.

Abundances for our target stars were determined by an iterative process in which the synthetic spectrum is compared to the observed one modifying the abundance in each step of the process until reaching the best fitting value. Given the large number of stars in our sample, we have developed a code which calculates the best fitting abundance by χ^2 minimization in a semi-automatic way. In the first step, radial velocities and a first guess for the FWHM of each star is determined using the DAOSPEC code (Stetson & Pancino 2008). The placement of the continuum is carried out manually for each star, by direct comparison between observed and synthetic spectrum in a region of 10 Å around the line of interest. Additionally, inspection of nearby lines

¹(http://www.eso.org/observing/dfo/quality/UVES/-pipeline/solar_spectrum.html)

3. The formation timescale of the Galactic bulge from alpha-element abundance measurements and gradients

Table 3.3: Abundances of the Sun, Arcturus and μ -Leonis, obtained by comparison to synthetic spectra, as well as reference solar abundances from Asplund et al. (2009). The last two rows show the zero point abundances adopted by AB10 and our mean abundances measured for those same disk giants to which they refer.

Stars	A(Ca)	A(Mg)	A(Ti)	A(Si)
Sun	6.39	7.60	4.95	7.51
Sun (Asplund et al)	6.34	7.60	4.95	7.51
Arcturus	5.93	7.30	4.55	7.17
μ -Leonis	6.65	8.02	5.31	7.85
AB10 ZP	6.32	7.65	4.83	7.60
This work	6.49	7.65	5.09	7.62

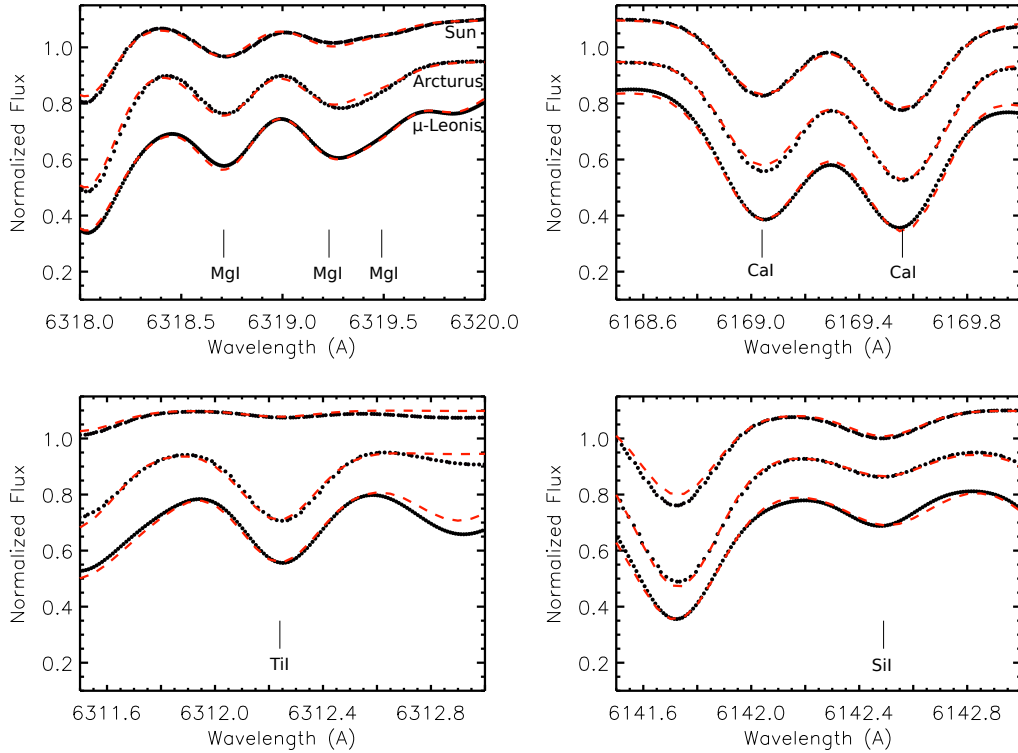


Figure 3.2: Calibration of the synthesis regions for the Sun, Arcturus and μ -Leonis. Observed spectra convolved to the GIRAFFE resolution are shown as black dotted line and the red dashed line shows the synthetic spectra using the stellar parameters from L07 and abundances in Table 3.3.

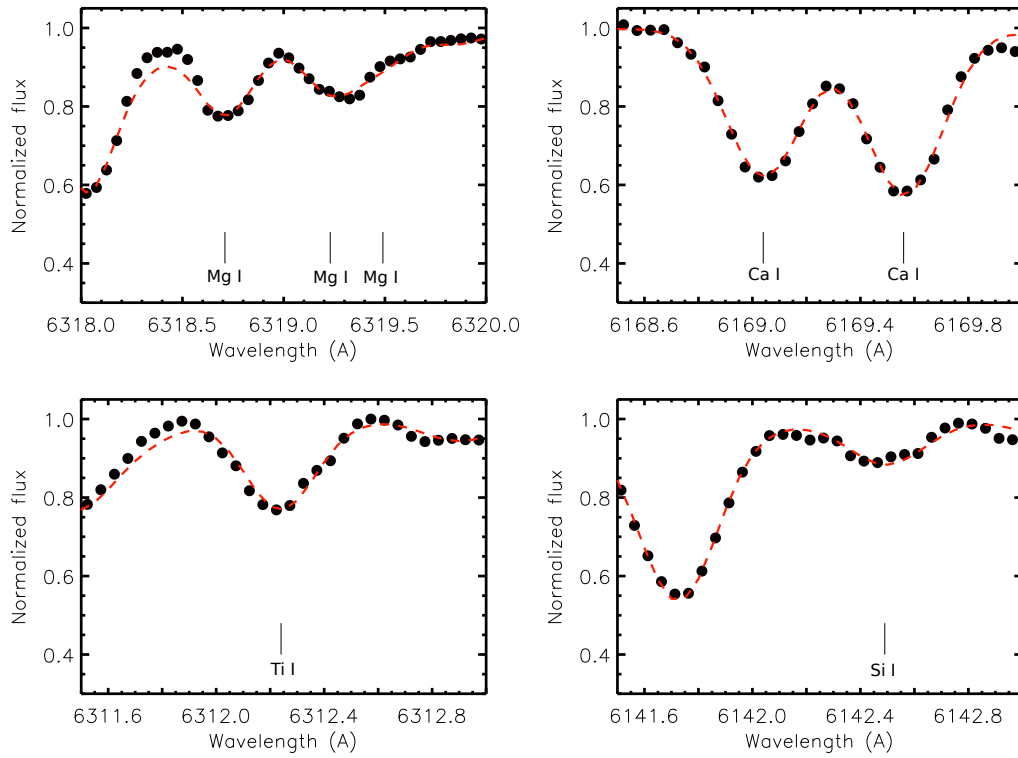


Figure 3.3: Example of the final output of the synthesis procedure in order to derive the abundances of Mg (upper left), Ca (upper right), Ti (lower left) and Si (lower right). Observed spectrum for target star 212175c6 is plotted as black dots and the red dashed line shows the synthetic spectrum using the best fitting abundance as obtained from our procedure.

are used to modify the FWHM from the value obtained from DAOSPEC, when the latter clearly fails to reproduce the spectral features. Later on, the code automatically calculates the best fitting abundance by minimization of a χ^2 value which is obtained in the following way:

$$\chi^2 = \sum_{\lambda} (F_{syn}(\lambda) - F_{obs}(\lambda))^2 \cdot W(\lambda) \quad (3.2)$$

where $F_{syn}(\lambda)$ is the flux of the synthesis at each wavelength, $F_{obs}(\lambda)$ is the observed flux previously normalized and $W(\lambda)$ is a weight value calculated as the difference between a normal synthesis and another without the line of the element to be fitted. This allows us to give more importance to the core of the line under analysis. To create this weight we have used μ Leonis parameters and abundances as a reference (Gratton & Sneden 1990). Figure 3.3 shows an example of the final output from the code for each analyzed line.

3.4 Error analysis

3.4.1 Error due to stellar parameters uncertainties

We have carefully analyzed the effect of the different sources of error in our procedure. When obtaining stellar abundances the errors are commonly dominated by the uncertainties in the stellar parameters. Their influence can be determined by varying the adopted parameters by their respective uncertainty and then re-calculating the abundance value which best fits the observed spectra. We have carried out this analysis in a subsample of stars which covers the whole range of metallicities and effective temperatures of our sample. We have used the uncertainties in stellar parameters presented in Z08 of 200K for T_{eff} , 0.3 dex in $\log g$, 0.2 dex in ξ and 0.1 dex in the final $[\text{Fe}/\text{H}]$ value. Figure 3.4 shows the variation in determined abundances for each element when varying the stellar parameters by their respective uncertainty. The final errors $\sigma_T, \sigma_{[\text{Fe}/\text{H}]}, \sigma_{\log g}, \sigma_{\xi}$ associated to each parameter were calculated as the average between the mean changes in abundance when uncertainties were added ($\sigma_{(+)}$) and subtracted ($\sigma_{(-)}$).

Figure 3.4 shows that errors in the abundance determination are strongly dominated by the uncertainties in the effective temperature determination. Given the adopted uncertainty of 200 K in temperature, Mg seems to be the least sensitive element with an associated error of $\sigma_{\Delta T}=0.05$ dex. Ca and Si show an associated error of 0.07 and 0.10 dex, respectively, and Ti has the largest dependence on temperature with an error value of $\sigma_{\Delta T}=0.17$ dex. From the lower left panel of Fig. 3.4 we see that the errors associated to the uncertainties in metallicity are quite similar among the elements with $\sigma_{[\text{Fe}/\text{H}]}$ values ranging between 0.05 and 0.10 dex for an adopted 0.1 dex error in $[\text{Fe}/\text{H}]$. Contrary to the sensitivity of the other elements, Mg is more affected by changes in metallicity than in temperature. The reason for such a dependence is most likely given by the blend with the strong FeI line at the red side of the triplet. Additionally Fig. 3.4 shows that the errors arising from uncertainties in gravity, $\sigma_{\log g}$, and microturbulence, σ_{ξ} , are small. However, Si still shows a 0.05 dex variation given an uncertainty of 0.3 dex in gravity. This is an important point to notice given that in our analysis we assume a distance of 8 kpc for all bulge stars, neglecting the bulge distance spread. If such stars are actually at 6 kpc, the bolometric magnitude will be underestimated by 0.65 mag. Such an error will change the photometric gravity by 0.25 dex. Mg abundances are almost completely in-sensitive to changes in both $\log g$ and ξ while Ca and Ti show a dependence of 0.06 dex on a microturbulence change of 0.2 dex.

3.4.2 Errors from the spectral synthesis

As described in Z08, stars in the field at $b = -12$ were observed twice due to a mistake in the fiber allocation. For this reason we only have about half the number of stars than in the other fields. However, we can use this repeated observation to carry out the same procedure to re-derive the abundances for all the elements analyzed in our work. In this way, we can estimate the influence of the steps in our analysis which are done by *eye* such as continuum placement and FWHM adjustment used for the synthesis. Additionally this will also provide an estimate for the errors associated to different S/N among stars in the same field. Figure 3.5 shows the difference

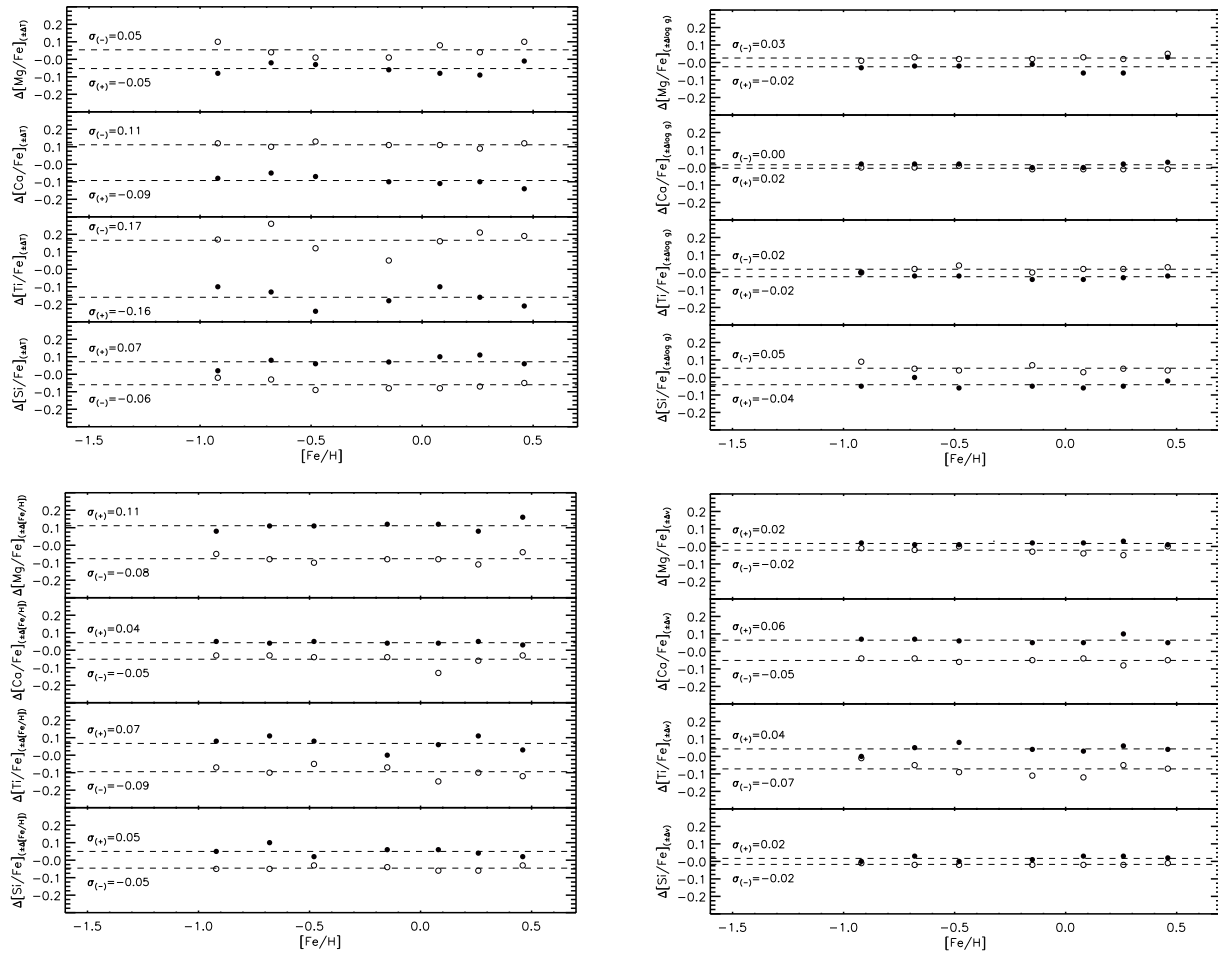


Figure 3.4: Abundance errors associated with the uncertainties in effective temperature (upper left), surface gravity (upper right), metallicity (lower left) and microturbulence (lower right). A change of ± 200 K was applied to T_{eff} , ± 0.1 dex to $[\text{Fe}/\text{H}]$, ± 0.3 dex to $\log g$ and ± 0.2 dex to ξ . Model atmosphere were then created and abundances were re-determined. Filled circles show the change in abundance as $\Delta[X/\text{Fe}] = [X/\text{Fe}] - [X/\text{Fe}]_{\pm\Delta}$ when changes were added to the original parameters. Empty circles show the change in abundance when the respective value is subtracted. Dashed lines show the mean variations $\sigma_{(+)}$ and $\sigma_{(-)}$ when the uncertainty in the stellar parameter is added and subtracted respectively.

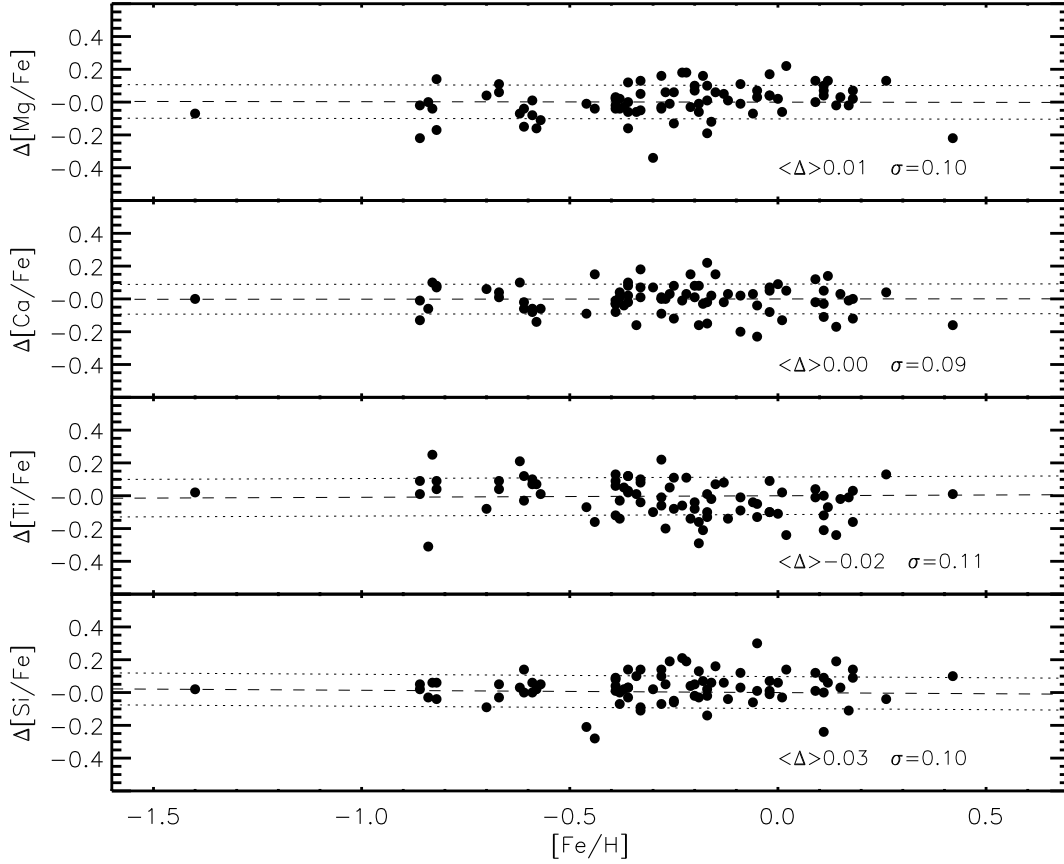


Figure 3.5: Difference between the abundances measured using the same lines for stars observed twice in the field at $b = -12$. The dashed line shows the mean difference between both measurements and the dotted lines the 1σ around the mean.

between the two independent analysis. The mean value of the difference for all elements ranges between 0 and 0.02 dex, which shows the absence of systematics in our procedure. The scatter is quite constant among the elements up to a value of 0.1 dex. Since the stellar parameters were not re-calculated, this scatter is not produced by their uncertainties but from the procedure to measure the abundances. We can therefore assume a 0.1 dex error from this source, which added to the errors from the stellar parameters gives an estimation for the final errors in our measured abundances following the relation:

$$\sigma_{[X/Fe]}^2 = \sigma_{\Delta T}^2 + \sigma_{\Delta[Fe/H]}^2 + \sigma_{\Delta \log g}^2 + \sigma_{\Delta \xi}^2 + \sigma_{syn}^2 \quad (3.3)$$

Therefore, the final values of the estimated error in our analysis are 0.15 dex for [Mg/Fe], 0.16 dex for [Ca/Fe], 0.22 dex for [Ti/Fe] and 0.14 dex for [Si/Fe].

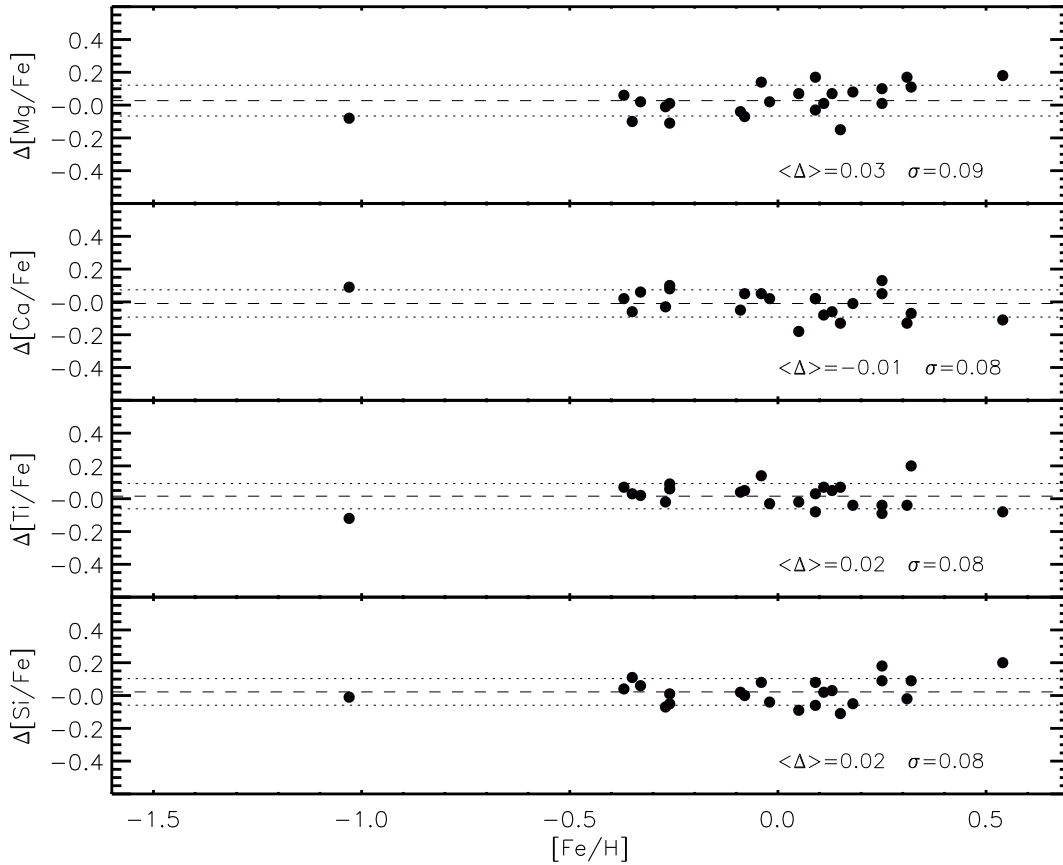


Figure 3.6: $\Delta[\alpha/\text{Fe}] = [\alpha/\text{Fe}]_{\text{UVES}} - [\alpha/\text{Fe}]_{\text{GIRAFFE}}$ for our bulge sample plotted as black filled circles. The dashed line indicates the mean value of the difference and the dotted lines show the 1σ range around the mean difference for each element.

3.4.3 The role of spectral resolution

It is also necessary to consider the effect of using lower resolution ($R \sim 22,500$) spectra from GIRAFFE in comparison to the high resolution of the disk sample of $R > 45,000$. In order to address this question we have re-calculated all the abundances using high resolution spectra for a subsample of stars in each field that was also observed with UVES ($R \sim 45,000$). The abundances were calculated following the same procedure as for the GIRAFFE sample.

Figure 3.6 shows the comparison between the abundances for each star in all analyzed elements. No systematic offsets are observed in our analysis from the change in resolution. This is particularly important to notice since it could be a source of systematic shifts in the trends when comparing bulge and disk.

In order to further check the existence of any systematics we have also redetermined the abundances in the disk sample after degrading the resolution of the spectra to the one of GI-

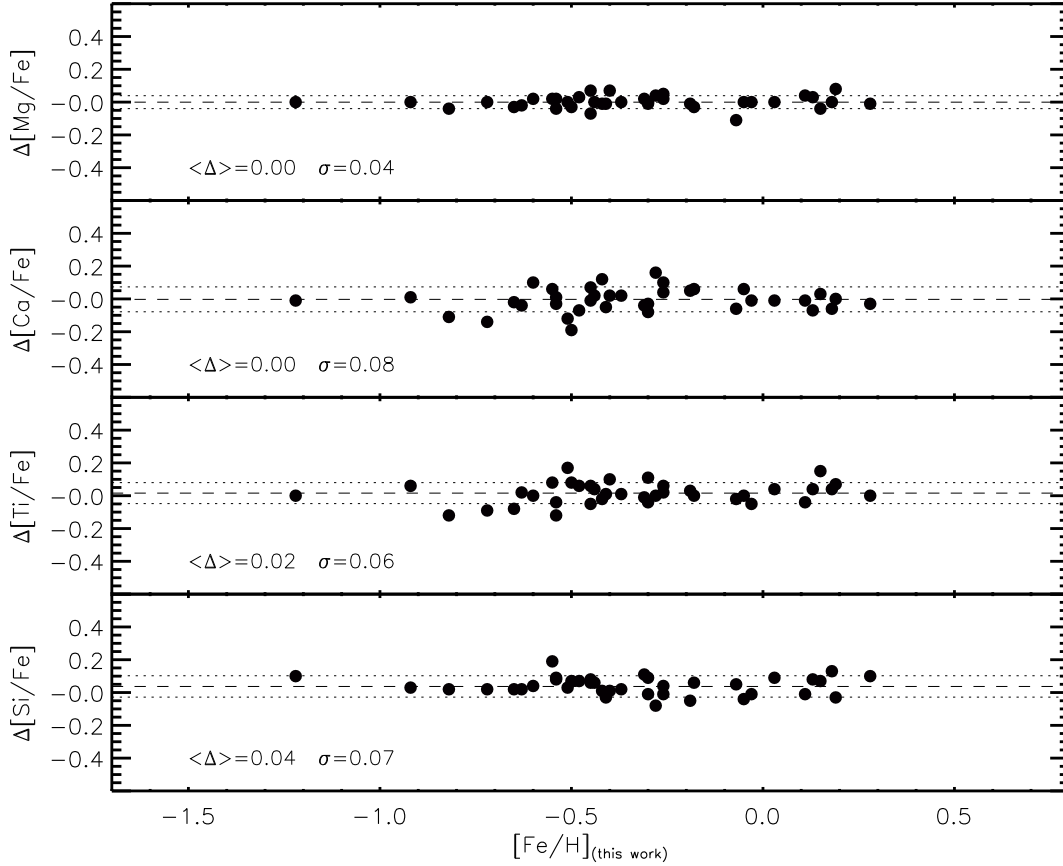


Figure 3.7: $\Delta[\alpha/\text{Fe}] = [\alpha/\text{Fe}]_{\text{HR}} - [\alpha/\text{Fe}]_{\text{LR}}$ for the disk sample plotted as black filled circles where the low resolution (LR) spectra were obtained by degrading the high resolution (HR) to the resolution of our GIRAFFE sample. The dashed line indicates the mean value of the difference and the dotted lines show the 1σ range for each element.

RAFFE. Figure 3.7 confirms that no differences are observed due to a change in resolution. Only Si shows a mean difference of 0.04 dex which is negligible within the errors on the abundance itself.

Additionally we have re-measured the abundances in our calibrator stars Arcturus, μ -Leonis and the Sun, using the spectra with the original high resolution. The results were compared with our abundance measurements from convolved spectra (Table 3.3 and Fig. 3.2) and no differences were found. We therefore conclude that our comparison of bulge stars based on lower resolution to those of the disk is valid and no systematic shifts should be applied to our results.

3.5 Results

3.5.1 Thick and thin disk sample

In order to characterize the bulge alpha abundances and compare them to other galactic components we have checked carefully the homogeneity of the procedure. Stellar parameters for the disk sample were calculated following the same procedure described in Z08. A comparison between the stellar parameters obtained using our procedure and the values presented in AB10 is shown in Fig. 3.8. We systematically find a larger effective temperature with a mean difference of 130 K between the two methods. Also, $\log g$ values are systematically larger in our analysis with respect to AB10. These differences between our studies show once more the importance of a homogeneous analysis in which parameters for all samples are on the same scale.

Using our determination of the stellar parameters, we have measured the abundances for Mg, Ca, Ti and Si as described in section 3.3. Figure 3.9 shows the difference between the abundances for the disk sample derived in this work and the values presented in AB10. Mg abundances appear to be on the same scale however abundances of Ca, Ti show larger differences.

AB10 uses the abundances of a subsample of thin disk stars, with metallicity near to the solar value, as internal zero-points. For the same stars we find larger Ca and Ti abundances as shown in Table 3.3. However we remain with our zero-points based on the solar abundances of Asplund et al. (2009). Table 3.3 should be used to compare our results either with models scaled to solar abundances or other works on different scales. Within our log-gf and adopted zero points, the homogeneity of our analysis remains unchanged.

3.5.2 Alpha elements across the bulge, thick and thin disk

The final $[\alpha/\text{Fe}]$ trends for Mg, Ca, Ti, and Si are shown in Figures 3.10 to 3.13 and listed in Table 3.4. The general alpha enhancement of the bulge stars is observed clearly in all four elements. The alpha enhancement is also seen in our globular cluster members and their mean abundances do not differ from those of field stars at their given metallicity. The scatter in the observed trends is different: Mg abundances show much smaller scatter than Ca, Ti and Si abundances. In particular at low metallicities, where there is almost no dependence on $[\text{Fe}/\text{H}]$, there is a ~ 0.09 dex scatter observed for $[\text{Mg}/\text{Fe}]$ and ~ 0.13 dex for the other elements. As shown in section 5, the dependence of the measured abundance on the stellar parameter uncertainties also varies among elements and the observed scatter in abundances is within the estimated errors. Therefore, the different amount of scatter is largely due to the uncertainties in the parameters. The similarity and overabundance in the bulge and thick disk stars appears to vary among the elements and therefore trends should be compared separately.

Mg is the element which shows the best defined trend among the elements analyzed here. This element shows the least dependency on the stellar parameters and can be considered as the most reliable of the alpha elements for chemical enrichment studies as, together with oxygen, it is expected to be enriched exclusively by SNI_{II} explosions. The mean abundance of the bulge at $[\text{Fe}/\text{H}] < -0.5$ is $[\text{Mg}/\text{Fe}] = +0.31$ which only differs by 0.03 dex from the mean thick disk at the same metallicity range with the bulge being slightly more enhanced than the thick disk. Such a

3. The formation timescale of the Galactic bulge from alpha-element abundance measurements and gradients

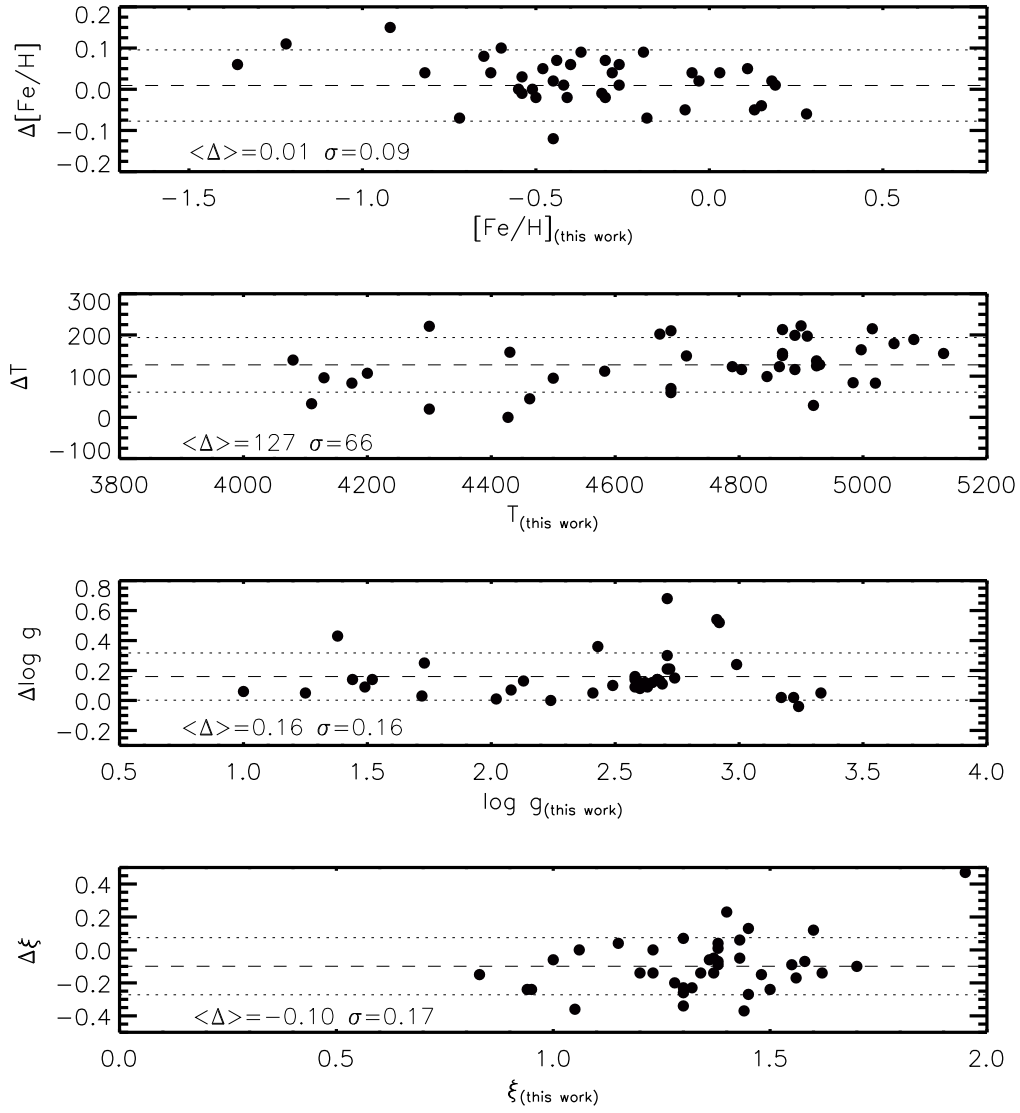


Figure 3.8: Difference between the stellar parameters obtained in this work and the values presented in AB10 calculated as $\Delta X = X_{\text{this work}} - X_{\text{AB10}}$. The dashed line indicates the mean value of the difference and the dotted lines show the 1σ range for each element.

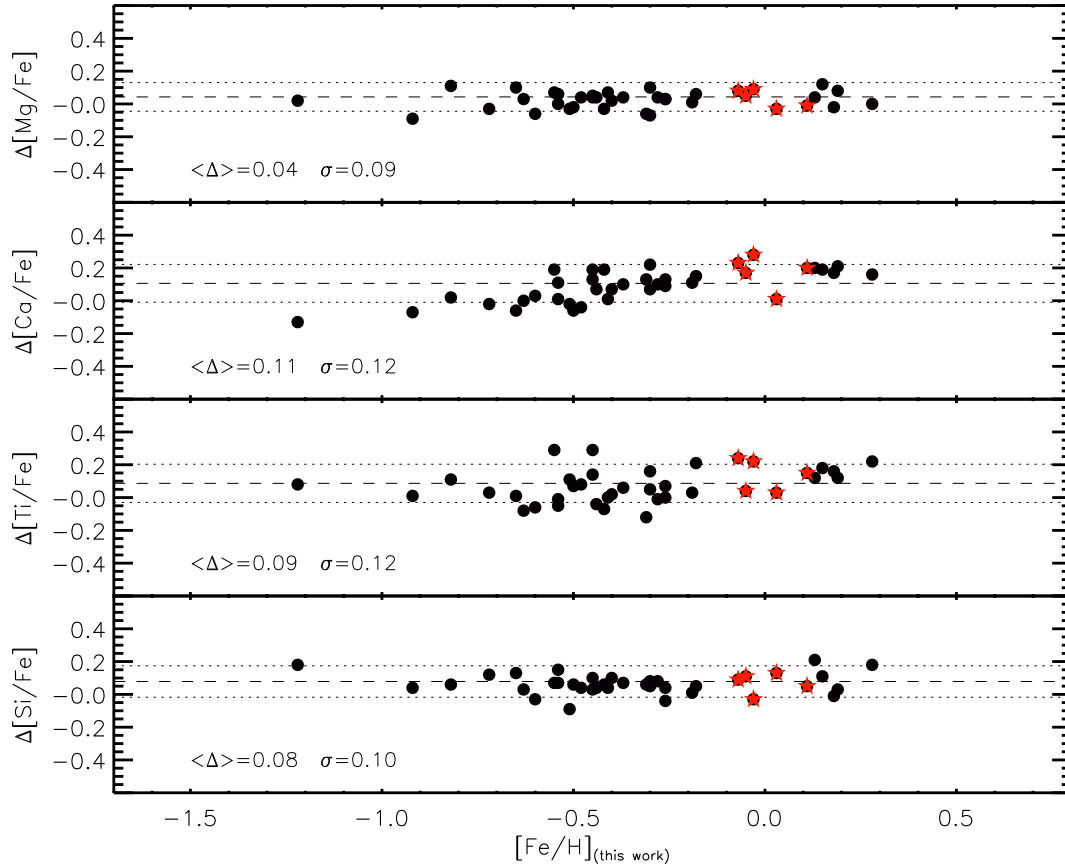


Figure 3.9: Difference between the $[\alpha/Fe]$ values for Mg, Ca, Ti and Si obtained in this work and the values presented in AB10 calculated as $\Delta[\alpha/Fe]=[\alpha/Fe]_{thiswork}-[\alpha/Fe]_{AB10}$. The dashed line indicates the mean value of the difference and the dotted lines show the 1σ range for each element. In particular, disk giants used by AB10 to calculate their internal zero points are shown as red filled stars.

Table 3.4: Mg, Ca, Ti and Si abundances for stars in the four bulge fields. Metallicities are those presented in Z08 and listed here for reference. The full table is available in Appendix B.

star ID	[Fe/H]	[Mg/Fe]	[Ca/Fe]	[Ti/Fe]	[Si/Fe]
423342	+0.46	-0.04	+0.13	+0.03	-0.08
423323	-0.48	+0.43	+0.15	+0.23	+0.26
412779	-0.37	+0.23	+0.29	+0.48	+0.22
423359	-1.23	+0.34	+0.30	+0.48	+0.43
.....

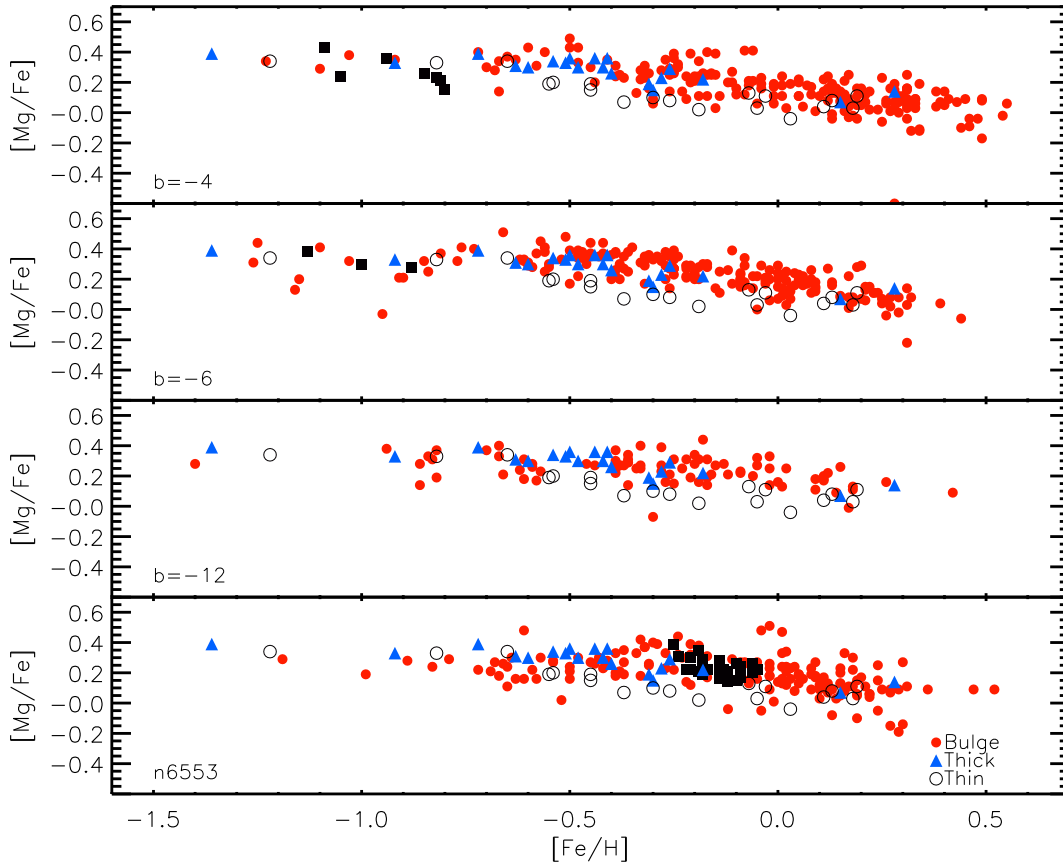


Figure 3.10: $[\text{Mg}/\text{Fe}]$ abundances in 4 fields of the bulge shown as red filled circles. Bulge globular cluster members are shown as black filled squares. $[\text{Mg}/\text{Fe}]$ abundances for the thick disk stars are shown as blue filled triangles and as empty black circles for the thin disk stars.

behavior remains in the intermediate metallicity range of our sample ($-0.5 < [\text{Fe}/\text{H}] < -0.2$) where the bulge shows a mean $[\text{Mg}/\text{Fe}]$ of 0.27 and is still only 0.03 dex more enhanced than the thick disk. The differences we have found between these populations are much smaller than those found by L07, in which the bulge is up to 0.2 dex more enhanced than the sample of thick disk dwarfs from the literature. Further comparison at higher metallicities are difficult because there are too few thick disk stars at those metallicities in the sample, as the separation between thin and thick disk becomes difficult. All elements show that, at the high metallicity range ($[\text{Fe}/\text{H}] > 0$) both the bulge and two of the high metallicity stars classified as thick disk by AB10 have lower ratios, as low as those of the thin disk.

On the other hand, $[\text{Ca}/\text{Fe}]$ trends show a larger scatter which complicates the comparison, particularly at high metallicities. However, at lower metallicities, where actually the thick disk is well defined, differences in $[\text{Ca}/\text{Fe}]$ between the mean of both populations are higher showing the bulge 0.09 dex more enhanced than the thick disk at $[\text{Fe}/\text{H}] < -0.5$ and 0.04 dex at higher

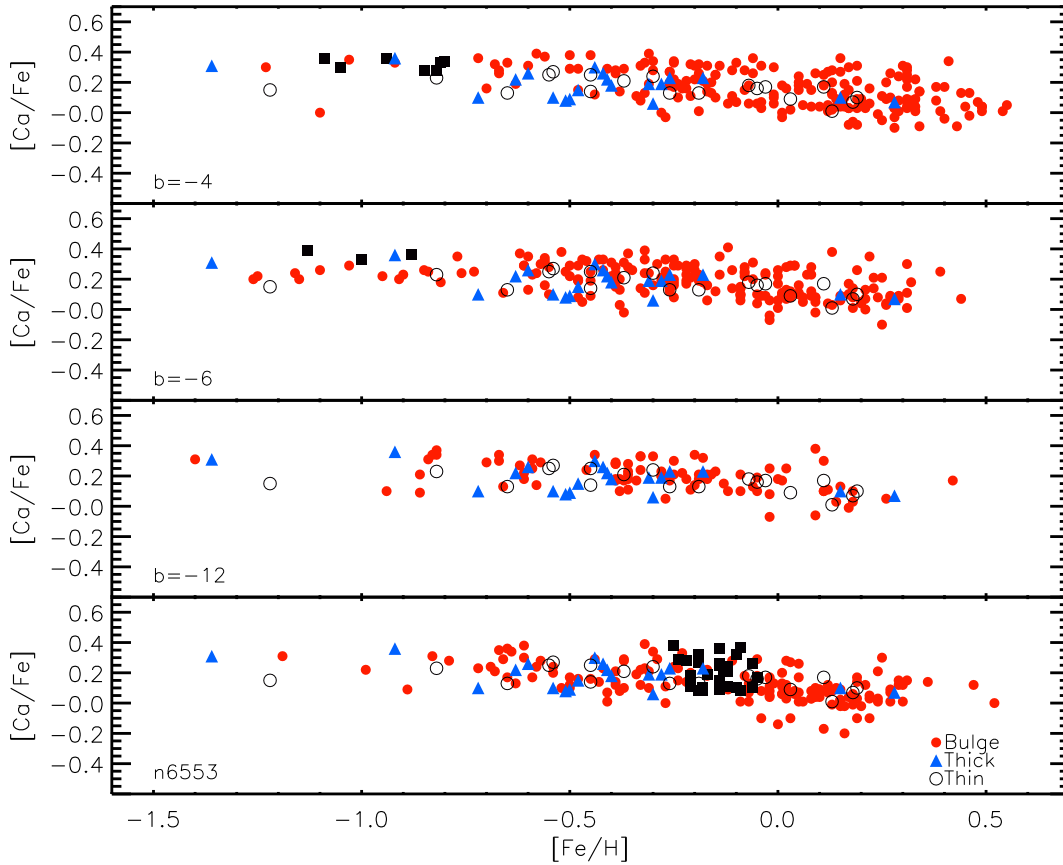


Figure 3.11: $[\text{Ca}/\text{Fe}]$ abundances in 4 fields of the bulge. Symbols are as in Fig. 3.10.

metallicities. Worth notice as well is that $[\text{Ca}/\text{Fe}]$ shows a shallower decline with metallicity than Mg in good agreement with model predictions where Ca contribution is also expected from SNIa explosions.

Results for $[\text{Ti}/\text{Fe}]$ are similar to those observed in Ca, showing trends with a shallower decline with metallicity but also a larger scatter. The mean abundance is $[\text{Ti}/\text{Fe}]=0.40$ and shows a difference with the thick disk of 0.10 dex from $[\text{Fe}/\text{H}]<-0.5$ up to intermediate metallicities. Only above solar metallicities the mean Ti abundances of bulge and thick disk are the same. However these differences are within the scatter of the Ti abundances in the bulge which is consistent with the larger error dependence on temperature. Moreover, the $[\text{Ti}/\text{Fe}]$ ratios in the thick disk are actually within the lower envelope of those of the bulge.

Finally in the case of $[\text{Si}/\text{Fe}]$, trends for the disk and the bulge are almost indistinguishable as in the case of Mg, with the bulge showing a mean $[\text{Si}/\text{Fe}]=0.35$ at $[\text{Fe}/\text{H}]<-0.5$ and differences lower than 0.03 dex with the thick disk at all metallicities.

Figure 3.14 shows the average α element abundances as $[\alpha/\text{Fe}]=[\langle\text{Mg},\text{Ca},\text{Ti},\text{Si}\rangle/\text{Fe}]$. Trends for the bulge and both thin and thick disk are very well defined and we can also use them to

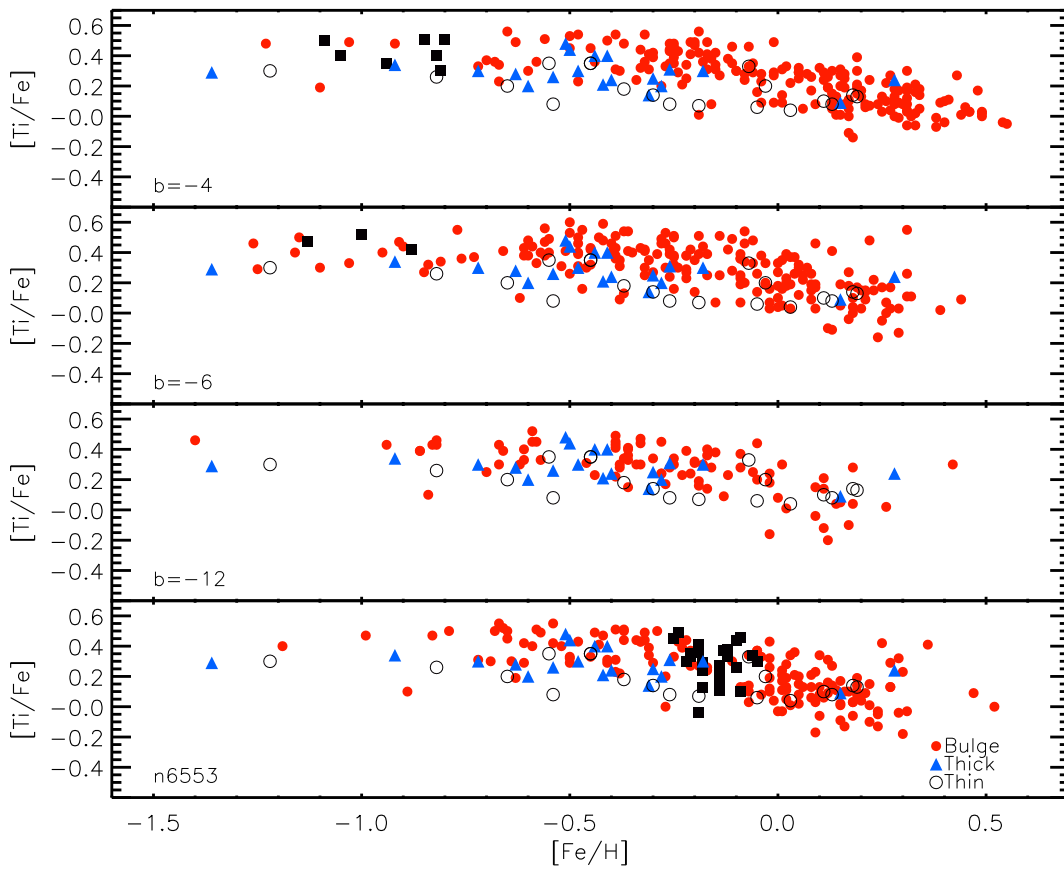


Figure 3.12: $[Ti/Fe]$ abundances in 4 fields of the bulge. Symbols are as in Fig. 3.10.

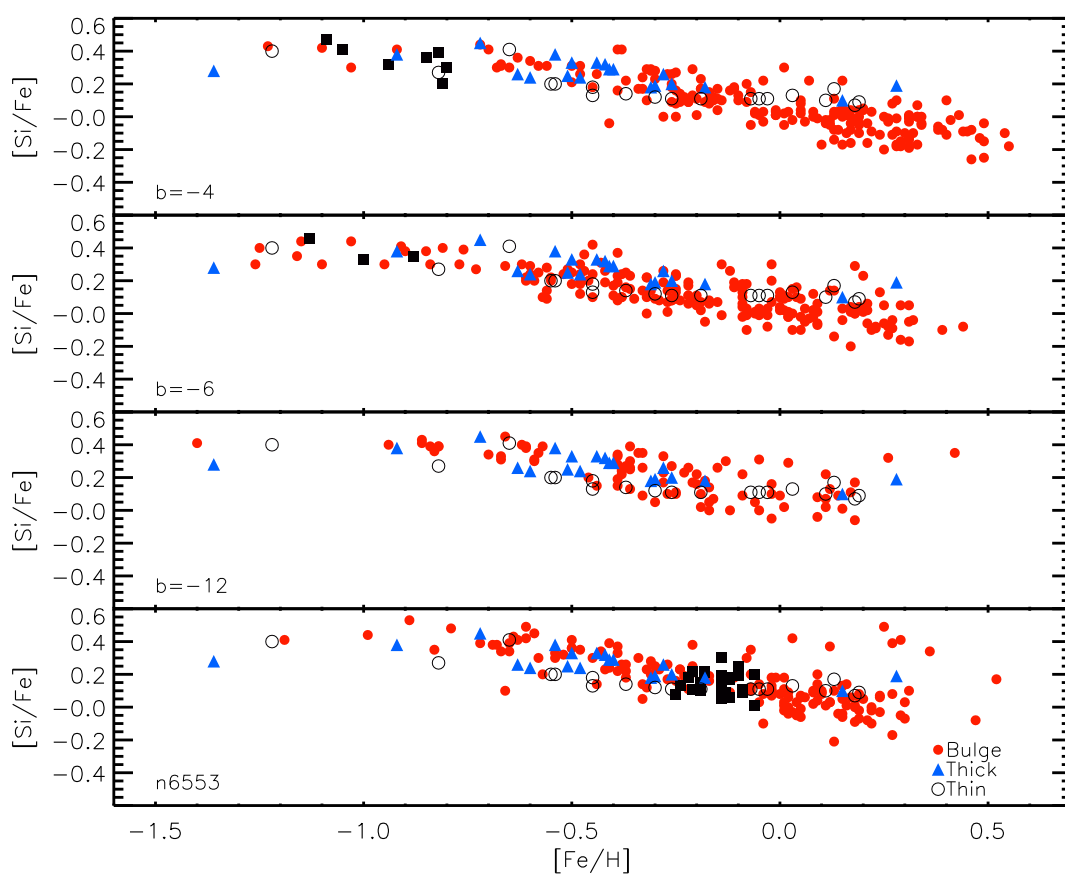


Figure 3.13: $[Si/Fe]$ abundances in 4 fields of the bulge. Symbols are as in Fig. 3.10.

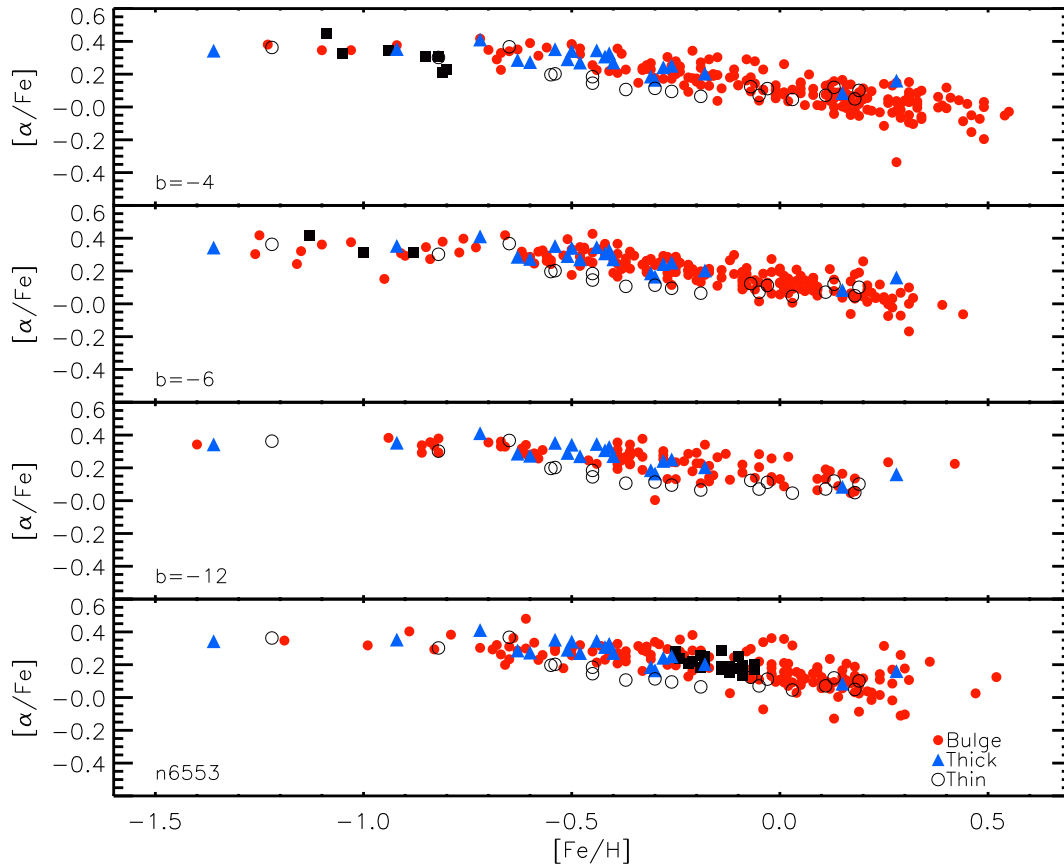


Figure 3.14: $[\alpha/\text{Fe}]$ abundances in 4 fields of the bulge calculated as the average between Ca, Mg, Ti and Si abundances. Symbols are as in Fig. 3.10.

compare the population properties between our different fields along the minor axis and with the field at a larger galactic longitude of $l=5^\circ$. A discussion regarding such a comparison is addressed in section 3.6

In order to generally compare abundances between bulge and disk, we have followed the procedure adopted in AB10 and fit two independent slopes for two different metallicity regimes. However, instead of fixing arbitrarily the point where the knee is produced to a $[\text{Fe}/\text{H}]$ value of -0.5 , as done in AB10, we have produced a linear fit to a metal-poor region between -1.2 and -0.5 dex and to a metal-rich region between -0.3 and 0.2 dex. These regions were selected in order to i) consider metallicity regions in which the trends are well defined and ii) avoid taking into account too metal-rich stars in which the uncertainties are larger. In this way, we are now able to provide a value for the metallicity at which the knee is actually produced, calculated as the intersection of the linear fits of both regions. The best fitting relations for both metallicity ranges in all the bulge fields and the thick disk are shown in Table 3.5 and plotted in Figures 3.15 and 3.16.

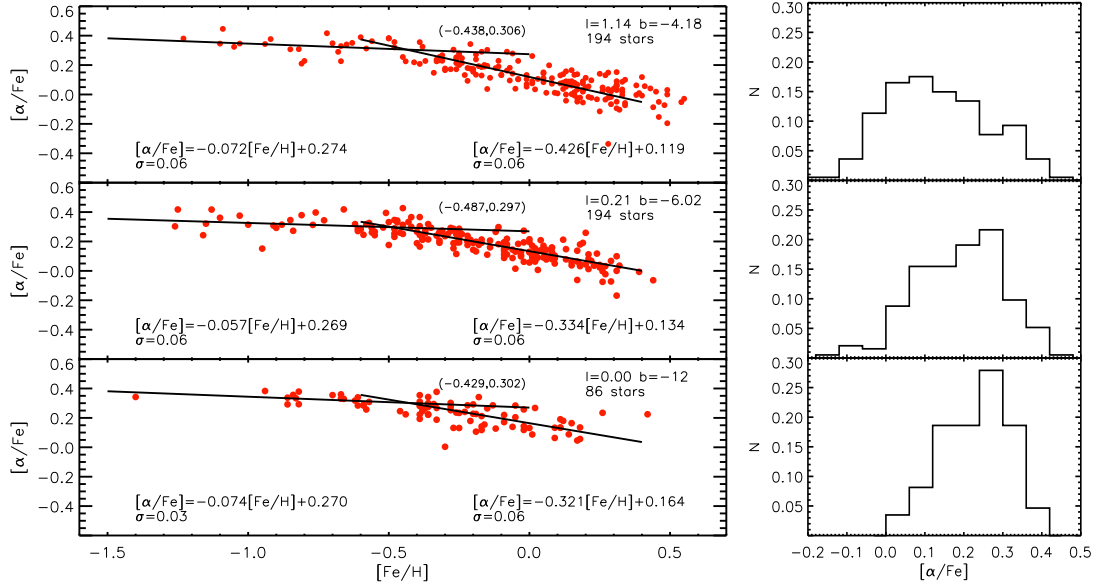


Figure 3.15: The left panels show $[\alpha/\text{Fe}]$ trends as a function of $[\text{Fe}/\text{H}]$ in 3 bulge fields located along the minor axis. Best fit trends are shown for both $[\text{Fe}/\text{H}]$ ranges, a metal-poor between -1.2 and -0.5 dex and a metal-rich between -0.3 and 0.2 dex, as well as the location of the knee in all fields. The right panels show the $[\alpha/\text{Fe}]$ distribution for each field.

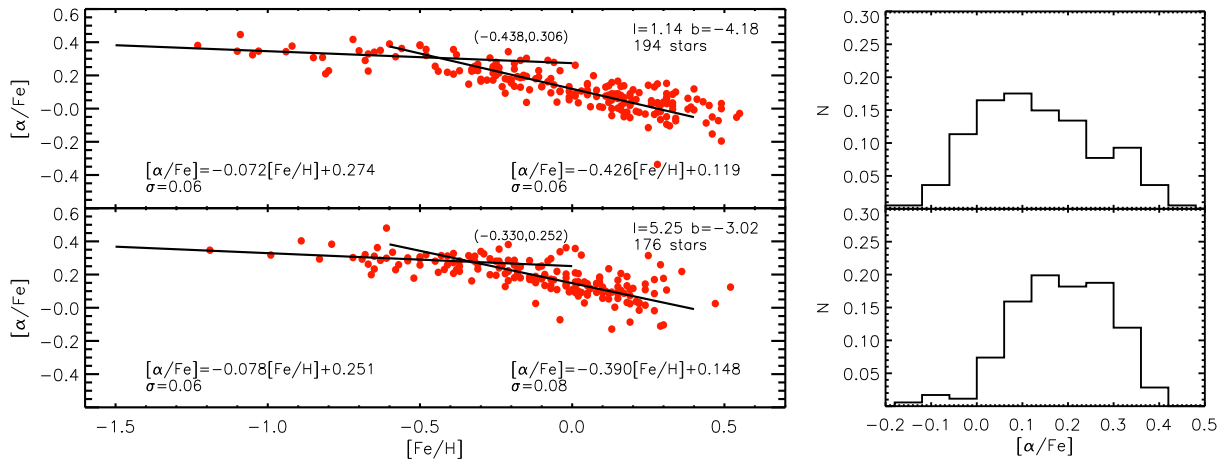


Figure 3.16: Same as in Figure 3.15 for 2 bulge fields along the major axis.

Table 3.5: Best fit parameters for linear ($a+m[\text{Fe}/\text{H}]$) trends for [$\langle \text{Mg}, \text{Ca}, \text{Ti}, \text{Si} \rangle / \text{Fe}$] abundances in the bulge and thick disk.

Field	$-1.2 < [\text{Fe}/\text{H}] < -0.5$		$-0.3 < [\text{Fe}/\text{H}] < 0.2$	
	m	a	m	a
Baade's Window	-0.07 ± 0.07	0.27 ± 0.06	-0.43 ± 0.04	0.119 ± 0.006
$b = -6^\circ$	-0.06 ± 0.04	0.27 ± 0.04	-0.33 ± 0.04	0.134 ± 0.006
Blanco field	-0.07 ± 0.04	0.27 ± 0.03	-0.32 ± 0.06	0.16 ± 0.01
NGC 6553	-0.08 ± 0.09	0.25 ± 0.06	-0.39 ± 0.06	0.148 ± 0.008
Thick disk	-0.04 ± 0.06	0.30 ± 0.05	-0.37 ± 0.08	0.13 ± 0.03

As a general result, when considering the mean abundances of all the elements analyzed, differences between the bulge and the thick disk do not exceed 0.05 dex for all metallicities. Trends between both populations are therefore indistinguishable within the errors of our analysis. Additionally we see that the knee in the bulge in Baade's Window is located at a metallicity of $[\text{Fe}/\text{H}] = -0.44$ and differs by less than 0.1 dex among the other bulge fields. This knee is also present in the thick disk distribution at $[\text{Fe}/\text{H}] = -0.51$, only 0.07 dex different from the location for the observed bulge downtrend. Therefore, within the errors considered in our analysis as discussed in previous sections, no significant differences are observed between the bulge and the thick disk abundances for individual elements. The similarity is even stronger when all elements are compared in the mean.

3.5.3 Is there an α -element gradient in the bulge?

The existence of a metallicity gradient in the bulge is considered a strong indication towards the classical bulge formation scenario and is not expected to be present in boxy or pseudo-bulges. On the other hand, if Galactic bulge is a mixture of two (or more) components, it could be expected that these populations should have gone through different formation histories. A component formed via mergers would show higher alpha elements than a structure dynamically formed from disk material which would have enough time for SNIa to explode and decrease the $[\alpha/\text{Fe}]$ ratio up to Solar values. These components might have different relative contributions across the bulge and therefore their content of alpha elements might help to distinguish between them.

Figures 3.15 and 3.16 show that in the case of the Galactic bulge, the relations between $[\alpha/\text{Fe}]$ and metallicity are indistinguishable among the different fields analyzed here. From the obtained relations for each field and in the two metallicity regimes that we have considered here, we can actually see no significant difference between the fields in terms of the IMF and the timescale given by the knee at which SNIa contribution becomes important. Differences between the fields are not larger than 0.02 dex at all metallicity regimes and the knee is observed at the same metallicity within 0.1 dex. This variation is in fact within our estimation for the uncertainties in

$[\text{Fe}/\text{H}]$. Such small differences are fairly consistent with the errors considered in our abundance analysis and a striking similarity can be concluded both along the minor axis (Fig. 3.15) and the major axis (Fig. 3.16). Also shown in Fig. 3.15 and Fig. 3.16, are the $[\alpha/\text{Fe}]$ distributions for each of the fields. The behavior of such distributions are consistent with the metallicity gradient in the bulge in which the population of stars with higher metallicities ($[\text{Fe}/\text{H}]\sim 0$) and lower α element abundances ($[\alpha/\text{Fe}]\sim 0$) becomes smaller at higher distances from the galactic plane.

3.5.4 Correlation with kinematics

Coupling the information from radial velocities, proper motions and metallicity for the same bulge FLAMES sample that we present here, Babusiaux et al. (2010) demonstrate that metal-rich component shows disk/bar kinematics and a metal-poor component has kinematics of an old spheroid. The formation time-scale for the old (and metal-poor) spheroid component is much shorter, than that of the disk/bar component, and therefore it is expected that the former is alpha enhanced, while the latter has lower alpha element abundance. We investigate this by combining our alpha element abundances with radial velocity information from Z08. Figure 3.17 shows the radial velocity dispersion for different alpha element abundance bins. We observe that alpha-enhanced stars have a velocity dispersion of ~ 90 km/s, which is approximately constant along the minor axis, while the stars with solar or slightly sub-solar $[\alpha/\text{Fe}]$ abundances have larger velocity dispersion in the inner fields and decreasing velocity dispersion at higher latitude. In the $b=-12^\circ$ field the most alpha-poor component disappears altogether. The behavior of alpha-enhanced stars mimics very closely the (lack of) trend shown by metal-poor component identified as having spheroid kinematics, while alpha-poor stars follow the trend of metal-rich component identified with disk/bar kinematics by Babusiaux et al. (2010). While these trends are interesting, they need to be confirmed with a more complete coverage of the bulge.

3.6 Implications of $[\alpha/\text{Fe}]$ abundance results on the Bulge formation history

We have confirmed the chemical similarity between the alpha element abundances in bulge and thick disk within the errors associated to our homogeneous abundance analysis. An overabundance in alpha elements of $[\alpha/\text{Fe}]=0.30$ dex up to a metallicity of $[\text{Fe}/\text{H}]\sim -0.5$ is observed in both components as an indication of a short timescale of formation, with a chemical enrichment dominated by the contribution of core collapse supernovae. At this metallicity the observed downtrend in the bulge reflects the instance in which the Fe contribution from SNIa becomes important. In the bulge both the trend at low metallicities and the value at which the knee is produced do not vary along the minor axis for latitudes $b < -4$. This can be interpreted as a formation process of the dominating population of the bulge being fairly homogeneous, sharing a similar IMF and formation timescale. Figure 3.16 shows that these trends are indistinguishable also for two fields at different longitudes ($l = 1^\circ$ and $l = 5^\circ$) at a fixed latitude of $b = -4^\circ$, an indication that the homogeneity is present along the major axis as well.

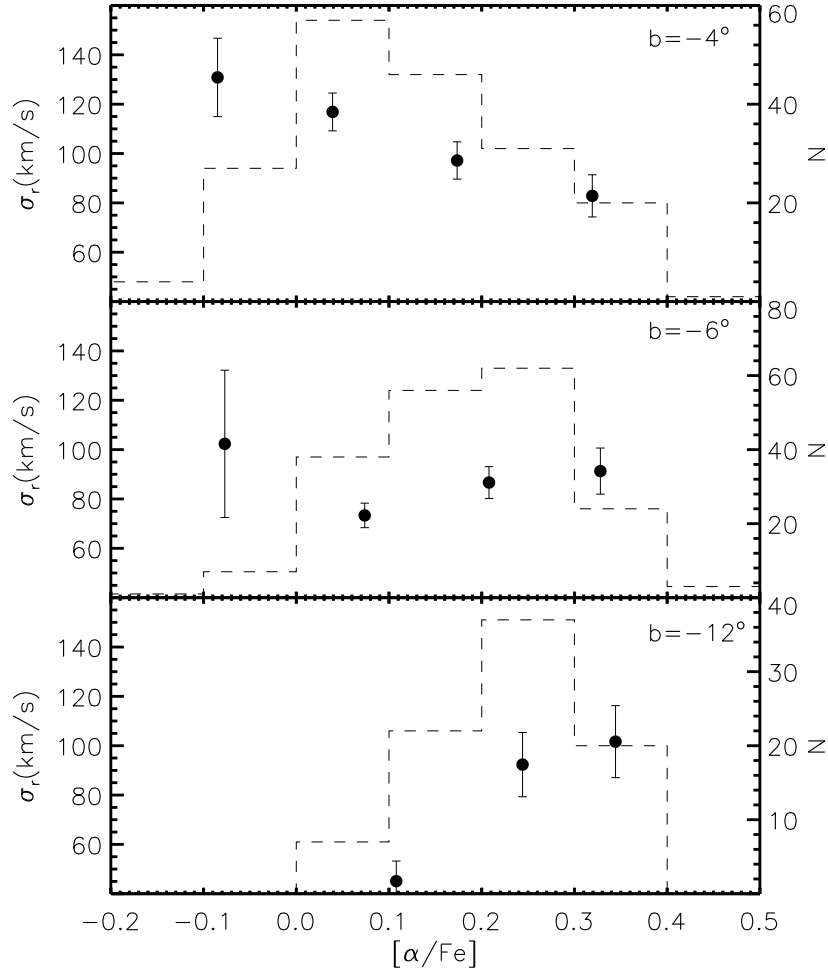


Figure 3.17: Dispersion of radial velocity as a function of $[\alpha/\text{Fe}]$, in bins of 0.15 dex, for the three fields along the minor axis (filled circles and left axis scale). Overplotted as a dashed line is the $[\alpha/\text{Fe}]$ distribution for each field, which scale is given on the right. Globular cluster members in the sample were removed for this particular analysis.

The chemical similarity of bulge stars and those of the solar neighborhood thick disk, at least for metallicities in which thick and thin disk can be clearly separated, is also remarkably intriguing. Furthermore, Bensby et al. (2010a) demonstrated for the first time that inner disk stars show both the dichotomy thin-thick disk and the chemical similarity with the bulge. Either the bulge and thick disk went through similar formation histories or the process which formed the bulge is directly linked to that of the thick disk. Unfortunately the formation history of the thick disk is currently a matter of debate. Therefore, as long as a complete understanding of the formation mechanism of the thick disk is missing, a correct interpretation for the bulge–thick disk connection will be hard to achieve. Particularly interesting, in the context of our results, are the scenarios in which both bulge and thick disk share a fast and early formation such as the scenario discussed in Bournaud et al. (2009) (see also Immeli et al. 2004). They show the properties obtained from simulations in which a thick disk and bulge are formed internally by instabilities of gas-rich clumpy disks in young galaxies. Such clumpy and turbulent rotating disks are in fact observed in galaxies around $z \sim 2$ (Elmegreen et al. 2008). This shared formation mechanism could explain the observed chemical similarities between these components.

The main result our observations provide is that all fields in the bulge follow the same $[\alpha/\text{Fe}]$ vs. $[\text{Fe}/\text{H}]$ relation, and that metal-poor stars correspond to a population enhanced in α elements which shows homogeneous kinematics. These observational facts taken on their own are in accordance with the classical bulge formation through the fast dissipative collapse. This is in contrast with the recent literature claims of pure disk/bar origin of the Galactic bulge (Shen et al. 2010), which would result in shallower $[\alpha/\text{Fe}]$ decline, more similar to that of the thin disk. The most metal-rich part of the population, that shows a downturn in $[\alpha/\text{Fe}]$ has formed on a timescale long enough for SNIa to start contributing significantly with iron peak elements and shows kinematics corresponding to a disk/bar component according to Babusiaux et al. (2010). This component progressively disappears with increasing distance from the plane.

Altogether, our results provide observational evidence for the coexistence of a classical bulge, within a bar-like component. Dual component bulges have also been observed in external galaxies in the work of Peletier et al. (2007) which shows an old elliptical-like component dominating the Bulge at higher distances from the plane, while a disk-like component is observed in the central regions. In particular, we highlight the recent results from Williams et al. (2011). They show that the bulge of a pure disk galaxy, NGC 3390, rotates perfectly cylindrically, has chemical properties resembling those of the disk and shows no metallicity gradient. On the other hand, the boxy bulge of NGC 1381 shows more complicated rotation properties, is alpha enhanced with respect to the disk and shows a metallicity gradient. These properties for NGC 1381 strikingly resemble those presented here, on a star by star basis, for the Milky Way bulge. In terms of simulations, the chemo-dynamical model of Samland & Gerhard (2003) also predicts a composite bulge: an early collapse component and a metal-rich, alpha-poor population associated to a bar.

To settle the issue of the origin of the bulge and to interpret its observables in the context of the formation of the other Galactic components, a detailed analysis of the kinematics and stellar abundances is necessary with a more complete coverage of the bulge and in the inner disk of the Galaxy.

3.7 Conclusions

We have analyzed the abundances of Mg,Ca,Si,Ti in four fields of the Galactic bulge. We have carried out a homogeneous analysis comparing $[\alpha/\text{Fe}]$ ratios for a large sample of bulge stars (650) with those of giants belonging to the thin and thick disk in the Solar vicinity. We also compared bulge $[\alpha/\text{Fe}]$ distributions across the different fields in our sample. Our conclusions can be summarized as follows:

1. We have confirmed the chemical similarity regarding alpha element abundances between the bulge and the thick disk when a homogeneous analysis is done and using only giant stars spectra. Both populations are enhanced compared to the thin disk and show a downtrend in $[\alpha/\text{Fe}]$ starting at a metallicity of $[\text{Fe}/\text{H}] \sim -0.4$. At higher metallicities, close to solar, bulge $[\alpha/\text{Fe}]$ ratios drop to values similar to those of the thin disk.
2. The trends of $[\alpha/\text{Fe}]$ ratios are indistinguishable among our three fields along the bulge minor axis. Analysis of a field at $l = 4^\circ$, $b = 5^\circ$ hints for a homogeneity also present along the major axis. The knee showing the downtrend in $[\alpha/\text{Fe}]$ is observed in all fields at $[\text{Fe}/\text{H}] \sim -0.4$. A more complete mapping of different bulge regions is necessary to confirm the conclusions regarding the major axis lack of gradients as well to explore the $[\alpha/\text{Fe}]$ distribution for inner bulge fields ($b > -4$).
3. The $[\alpha/\text{Fe}]$ distributions in our different fields show that, while the population of metal-rich stars and low $[\alpha/\text{Fe}]$ ratios observed at $b = -4^\circ$ seems to disappear at larger galactic latitudes, trends and distributions at low metallicities ($[\text{Fe}/\text{H}] < -0.2$), as well as velocity dispersion, remain unchanged at different latitudes. Such results are consistent with recent evidences for a dual nature of the bulge.

Our results demand future work to be based on a more complete coverage of the bulge. A better mapping of chemical and kinematical signatures from spectroscopy, coupled with the complete morphological characterization to be obtained from a multi-epoch photometric survey such as the VISTA Variables in the Via Lactea (VVV; Minniti et al. 2010), could provide the final step towards the observational characterization of the bulge.

In the second part of the thesis, the global properties of the Milky Way bulge are investigated using the VVV first year data release (VVV DR1; Saito et al. 2012)

Chapter 4

The Red Clump as tracer of the Bulge extinction and structure

Stellar populations can be strongly characterized by the properties of the observed sequences along the color-magnitude diagram (CMD). The CMD is a plot of stellar color, defined as the difference between the magnitude in two different bands and related to the effective temperature of the star, and the stellar magnitude which is a measure of the stellar luminosity. Specific sequences can be identified in the CMD, given the luminosity and effective temperature of stars at different evolutionary phases, for a given mass, age, and chemical composition. For this reason, the different sequences in the CMD can be used to describe a given stellar population.

The magnitude of a star will become fainter, depending on the amount of dust in the line of sight towards the source. Since visual magnitudes are more affected by the dust extinction, stars will look fainter and redder in the CMD. Thus, a source of known intrinsic magnitude and color, known as standard candles, would be ideal to trace the reddening effects by comparing its intrinsic and observed colors. Once extinction effects have been corrected from the observed magnitude of the standard candle, this can be compared to its intrinsic magnitude to determine its distance.

In an old population, such as that of the Bulge, red clump (RC) giants are core-helium burning, metal-rich stars, equivalent of the horizontal branch stars in old metal-poor populations, and are easily identified in color-magnitude diagrams. Their intrinsic magnitude has a fairly well understood dependence on population properties such as age or metallicity (Girardi & Salaris 2001), and reddening effects in color can be clearly identified. The fixed luminosity and temperature of RC stars, for a given stellar population, is therefore an ideal tracer of these effects.

The RC feature is clearly visible in the CMD and its photometric properties can be well constrained. Indeed, Stanek & Garnavich (1998) determined that the dispersion in the I magnitude of RC stars is only ~ 0.15 mag. Later observations have provided enough support for the RC as a reliable distance indicator also in the near-IR (K , $J - K$) CMDs (Alves 2000; Grocholski & Sarajedini 2002; Pietrzyński et al. 2003; Laney et al. 2012) in good agreement with the expectations from theoretical models (Girardi & Salaris 2001; Salaris & Girardi 2002). Figure 4.1 shows the near-IR CMD in the absolute plane ($M_{K,(J-K)_0}$) for stars with known distances from Hipparcos satellite and 2MASS magnitudes (Casetti-Dinescu et al. 2011), where the RC is clearly observed

as an overdensity of stars at $(J - K_s)_0 \sim 0.68$ and $M_K \sim -1.5$.

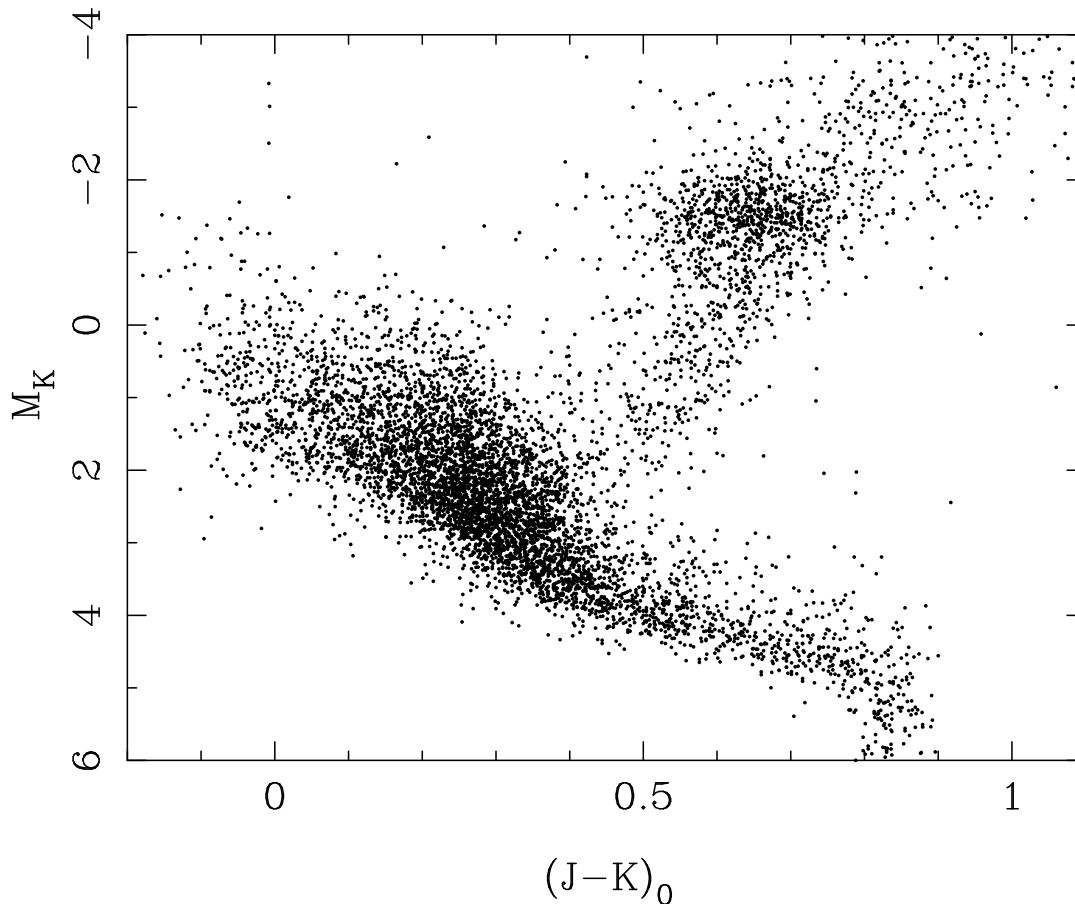


Figure 4.1: Near-IR Color-Magnitude diagram for a sample of disk stars with measured distances from the Hipparcos satellite and 2MASS magnitudes. This is Figure 2 from Casetti-Dinescu et al. (2011), reproduced by permission of the AAS.

The RC has therefore been used in several studies to derive extinction and distances in the edge of the Milky Way disk (Minniti et al. 2011), bar (Stanek et al. 1997; Babusiaux & Gilmore 2005; Rattenbury et al. 2007; Cabrera-Lavers et al. 2007), as well as distances to other galaxies such as M 33 (Kim et al. 2002), or IC 1613 (Dolphin et al. 2001). For old and relatively metal-rich population such as found in the Galactic bulge (e.g. Brown et al. 2010, and references therein) the population corrections for red clump absolute K-band magnitude are of the order of 0.1 mag (Salaris & Girardi 2002). In the following chapters, we use the near-IR photometric properties of RC giants to trace simultaneously extinction and relative distances in the Milky Way bulge, with an unprecedented resolution and coverage.

4.1 The VVV survey data

The VISTA Variables in Via Lactea (VVV)¹ is the Galactic near-IR ESO VISTA public survey that started collecting data in 2010. The VVV area covers $\sim 520 \text{ deg}^2$ and will be imaged repeatedly in K_s -band with the aim to search for variable stars such as RR Lyrae in the Milky Way bulge, as well as Cepheids and eclipsing binaries across the plane. In addition to the main variability campaign, the survey area is fully imaged in 5 photometric bands: Z, Y, J, H, and K_s .

The VVV survey has two main components: the $\sim 300 \text{ sq. deg}$ VVV Galactic bulge survey area covering $-10^\circ < l < +10^\circ$ and $-10^\circ < b < 5^\circ$, and the $\sim 220 \text{ sq. deg}$ VVV plane survey area spanning between $295^\circ < l < 350^\circ$ and $-2^\circ < b < 2^\circ$. In the first observing season in 2010 95% of the total area has been imaged in J, H and K_s wavebands, while the YZ imaging covered 84% of the disk and 40% of the bulge areas. The variability campaign has also started, but mostly it will be carried out in the upcoming observing seasons. The survey is expected to span 5 years of observations, enabling to characterize well both short and long period variable stars in the Milky Way bulge and the plane.

Here we describe only data used in the analysis in this thesis: the single-epoch JHKs coverage of the bulge. The more complete description of the whole survey and the observation strategy is available in Minniti et al. (2010), while the data release from 1 year observations and some first results are presented in Saito et al. (2010).

The observations are carried out in service mode with the VIRCAM camera on VISTA 4.1m telescope (Emerson et al. 2004; Emerson & Sutherland 2010) located at ESO Cerro Paranal Observatory in Chile on its own peak, some 1.5km away from the Very Large Telescope. The bulge survey area consists of 196 tiles, each $1.48 \times 1.18 \text{ sq. deg}$ in size. VIRCAM focal plane is sparsely populated with 4×4 Raytheon VIRGO 2048×2048 pixel arrays, and 6 exposures (so called pawprints) are needed to fully cover the 1.5 square degree field (so called tile). The mean pixel scale is 0.34 arcsec, and the point spread function delivered by the telescope and camera has $FWHM \sim 0.51$ arcsec. The median image quality measured on the reduced VVV tile images ranges between 0.8'' for K_s , 0.9'' for J band, and up to 1.0'' for Z-band.

VVV tiles are made combining 12 (two per pawprint) images for H , K_s and J band tiles. Each H and K_s image is a single 4 sec exposure, while J band images are sums of two 6 sec exposures. Each pixel in a tile has therefore a minimum of 16 sec exposure in H and K_s and 24 sec in J , and is an average of at least 4 individual exposures. VISTA data are processed through the VISTA Data Flow System (VDFS) by the Cambridge Astronomical Survey Unit (CASU). The basic data reduction steps consist of reset correction, dark subtraction, linearity and flat field correction, sky background subtraction, destriping step, jitter stacking and tiling. Finally the astrometric and photometric calibration are applied using 2MASS sources in the images, and the single band catalogues are produced (Lewis et al. 2010). In this work we use the single band tile images and catalogues version 1.1².

The list of the analyzed tiles is given in the Appendix B. They correspond to the tiles located in the Bulge region, covering $-10^\circ < l < +10^\circ$ and spanning $-10^\circ < b < +5^\circ$.

¹<http://vvvsurvey.org>

²More details about VISTA data processing is available from

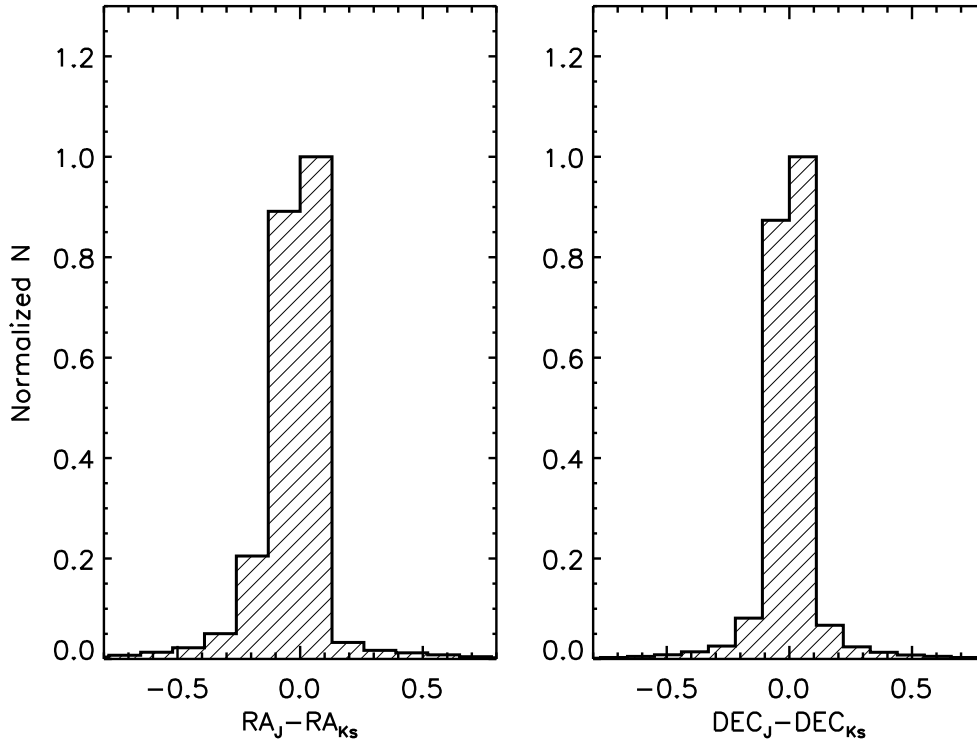


Figure 4.2: Distributions of the RA and DEC differences in arcsec between matched sources of single band, J and Ks, photometric catalogs. Crossmatching for field b278 is shown here as an example

4.1.1 Multiband catalogs

Target coordinates and J, H, K_s magnitudes were extracted from the single band catalogs produced by the CASU. These catalogs were then matched using the code STILTS (Taylor 2006). In particular, the routine *tskymatch2* is used to perform a match based on the proximity of sky positions of stars in each catalog. Several tests were carried out by modifying the maximum separation radius to match detections between J, H and K_s catalogs. The majority of stars were always found within a separation smaller than $0.5''$, in good agreement with the astrometric precision expected from CASU pipeline. Therefore, a maximum allowed separation of $1''$ was used to ensure that our matched catalogs contain most of the sources without risk of including wrong matches at a larger separation, and at the same time we still leave the possibility for some minor astrometry distortions in the large VIRCAM field of view. Figure 4.2 shows the distributions of the RA and DEC difference for J and Ks catalogue matches in the VVV field b278.

The single band tile catalogs produced by CASU contain a flag which identifies detections as stellar or non-stellar sources. We decided to only use sources with the stellar flag in all three

bands. Although this cleaning procedure implies that only $\sim 75\%$ of the original number of detections remain in the final multiband catalog, it allows us to work with as clean as possible sample of bulge stars, which is ideal for our purpose, and it does not bias our results.

4.1.2 Photometric calibration

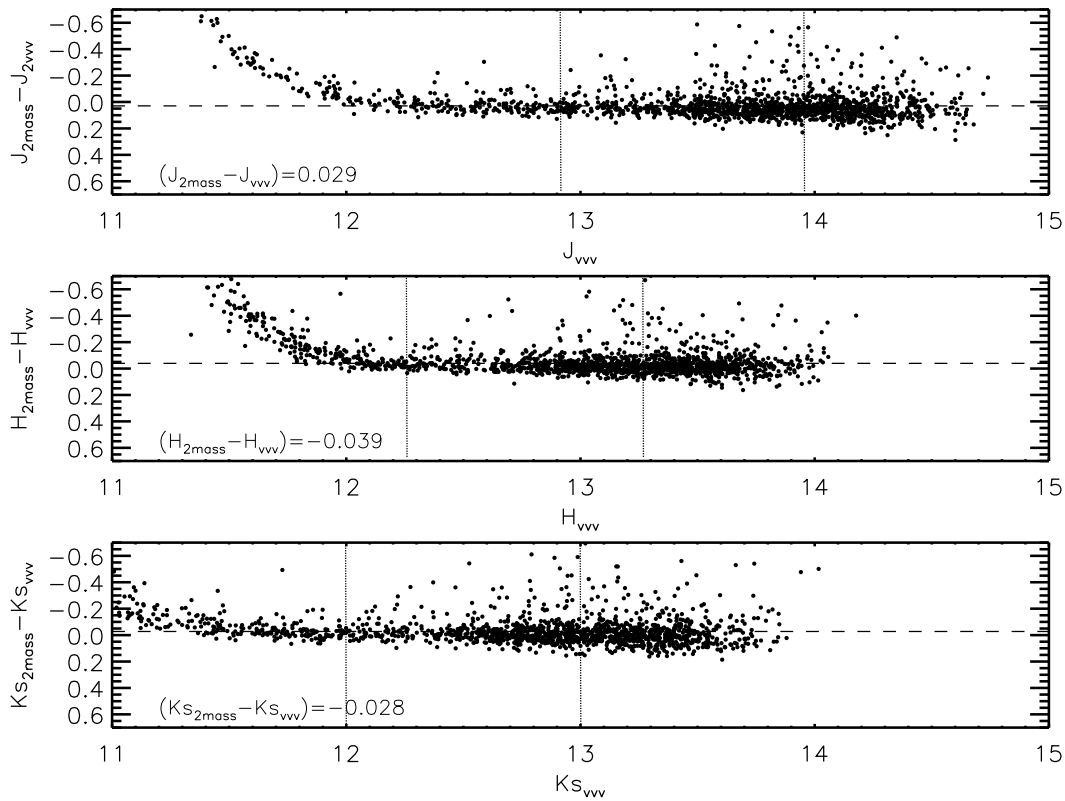


Figure 4.3: J , H and K_s magnitudes differences between VVV catalogs and 2MASS. Dashed lines show the mean difference between both catalogs in the range denoted by the solid lines

The VVV images extend about 4 mag deeper than 2MASS³ in spite of the short exposure times because of the difference in telescope apertures and spatial resolution. However, the larger telescope aperture of VISTA results in saturation for brightest stars. For this reason 2MASS photometry is required to complete the bright end of the VVV catalogs. Figure 4.3 shows the J , H and K_s magnitude differences between VVV and 2MASS sources in a common 10×10 arcmin window within the tile b278. We only adopted 2MASS sources with best photometric quality (flag AAA). Two important points can be observed from Fig. 4.3: i) The saturation magnitude in the VVV photometry is clearly observed at $K_{s,vvv} < 12$; and ii) there is a very small offset

³The exact difference between VVV and 2MASS photometry depth depends strongly on the stellar density in the field.

between the zero points of both catalogs. Still, we must ensure that both catalogues are in the same photometric system to be able to complete the saturated bright end of the VVV photometry with 2MASS. In doing this, only stars common to both surveys and with $13 > K_{s,\text{vvv}} > 12$ (see Fig.2) were used to bring the VVV catalogues onto the 2MASS photometric system. The magnitude range selected for the calibration ensures that the differences are not affected by larger errors in the photometry for 2MASS or saturation for VVV measurements. This procedure was carried on independently for each VVV tile and zero points were calculated for each one of the catalogs. Once calibrated, stars brighter than $K_s \sim 12$ from 2MASS were used to complete the bright end of our final VVV catalog. These catalogs, corrected for saturation and calibrated to 2MASS zero points were used in further analysis. Hence, hereafter we refer to the usual J, H, K_s magnitudes corresponding to the 2MASS photometric system.

4.2 Characterizing the Red Clump in the Bulge color-magnitude diagram

Figure 4.4 shows the $K_s, J - K_s$ color-magnitude diagram (CMD) of a selected region in the field b278. The photometry samples the entire RGB from the base up to the tip ($K_s \sim 8$). The RGB is quite bent as expected for metal-rich populations and its relatively large width is due to metallicity spread (Zoccali et al. 2003), depth effects and some differential reddening. The red clump is located at $K_s \sim 13$, and it is partially merged with the RGB bump. Although the photometry is deep enough to properly sample the sub giant branch, the almost vertical bluer sequence at $(J - K_s) \sim 0.4$ due to foreground disk stars prevents to detect its exact location.

Studies of the chemical abundances and age measurements of the Bulge towards Baade's Window, have shown that the Bulge is predominantly old (~ 10 Gyr) (Ortolani et al. 1995; Zoccali et al. 2003; Brown et al. 2010; Clarkson et al. 2011) and that it shows a broad metallicity distribution with a peak near Solar metallicity (McWilliam & Rich 1994; Zoccali et al. 2008; Johnson et al. 2011). Stellar evolutionary models can thus provide specific constraints on the expected intrinsic color of stars along the different evolutionary stages. The observed color can then be compared to that expected from models and its difference can be linked to an external factor, such as extinction. The metallicity of the Bulge is not spatially uniform, but it shows a gradient along its minor axis (Zoccali et al. 2008). Furthermore, the extent of these gradients towards other regions is not yet clear. For this reason, uncertainties may arise from direct comparison of the observed red giant branch (RGB) stars' colors with respect to those expected from models. Fortunately, this effect can be minimized by the use of RC giants, as the mean color of these stars has a small dependence on these parameters.

The influence of the population effects on the RC magnitudes and color has been investigated both theoretically (Girardi & Salaris 2001; Salaris & Girardi 2002) and observationally (Alves 2000; Grocholski & Sarajedini 2002; Pietrzyński et al. 2003; Laney et al. 2012). In both cases, RC stars appear as reliable standard distance indicator, considering the possible variations in the general Bulge population properties. While the age of the bulge is expected to be homogeneously old (~ 10 Gyr), the metallicity is known to change at least along the minor axis (Zoccali et al.

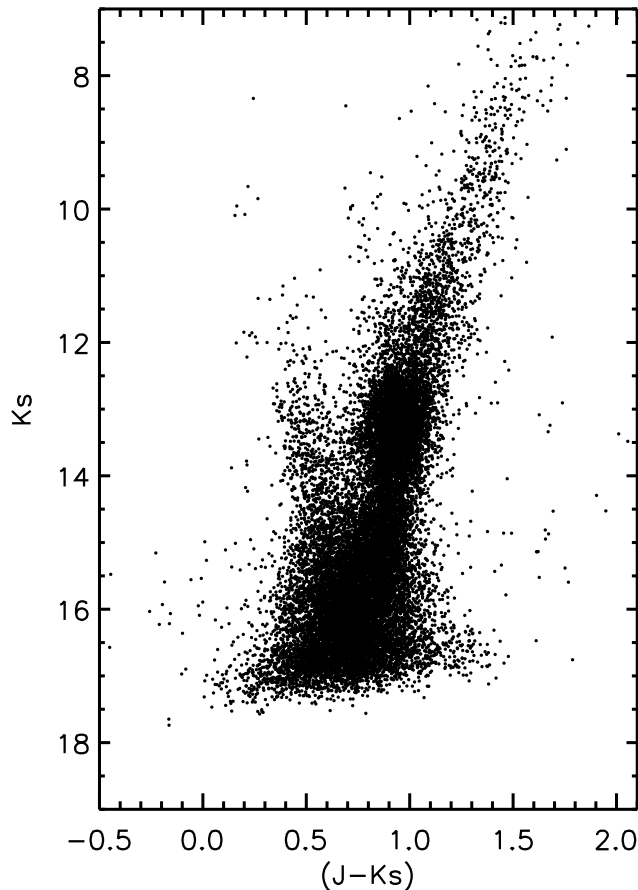


Figure 4.4: VVV observed $(J - K_s, K_s)$ CMD of a $20' \times 20'$ region within the tile b278 calibrated and completed with 2MASS photometry.

2008). If we consider this variation of the mean Bulge metallicity to be $\Delta[\text{Fe}/\text{H}] = -0.4$ (Rich et al. 2007; Zoccali et al. 2008, see also Chapter 7 of this thesis), we expect an error in the mean RC color of ~ 0.08 mag, equivalent to a variation of $A_{K_s} = 0.06$ mag assuming the Cardelli et al. (1989) extinction law and $A_{K_s} = 0.04$ mag for Nishiyama et al. (2009) law.

4.2.1 Red clump color in the reference Bulge field: Baade's Window

Here, we use the multiband VVV catalogs to determine extinction values by measuring the mean $(J - K_s)$ color of the RC stars and comparing it to that of a region of known extinction, named Baade's Window. A selection box in the CMD of each tile is chosen to include only Bulge red clump stars. The limits of this box vary for each line of sight depending on the amount of extinction and were therefore inspected by eye and modified accordingly. A Gaussian fit to

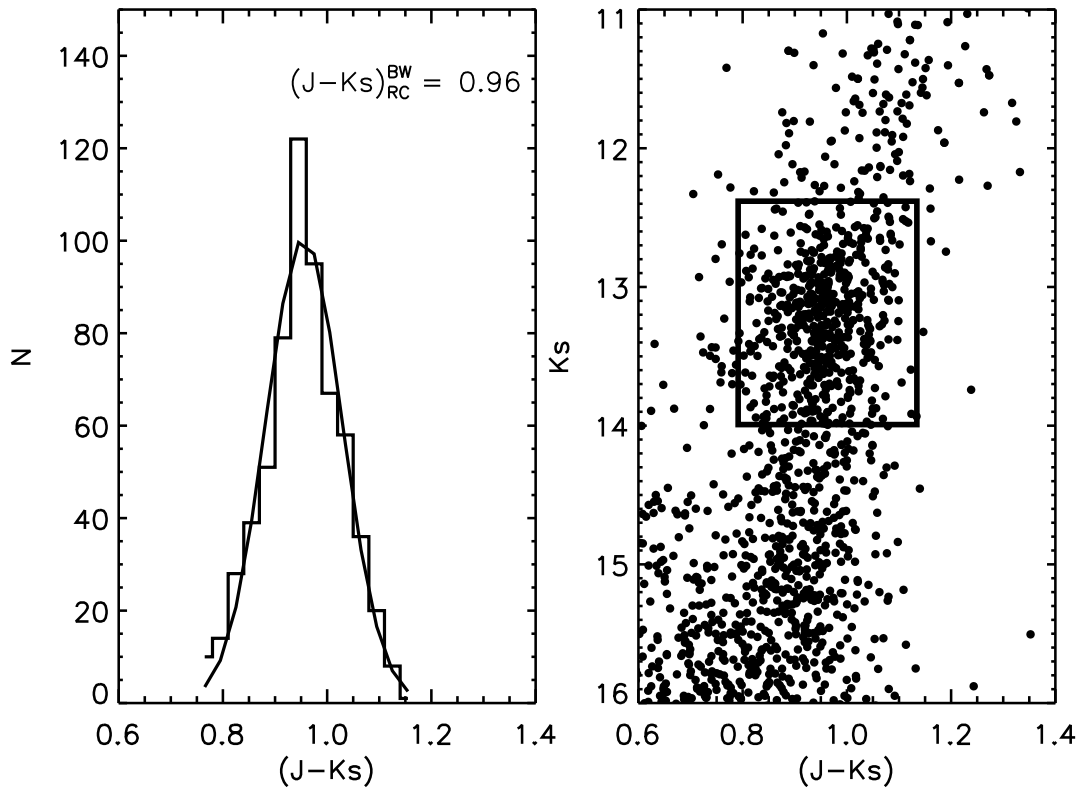


Figure 4.5: Right panel shows the observed color magnitude diagram for a 4×4 arcmin region centered in Baade’s Window and a selection box corresponding to the red clump. Left panel shows the color distribution of these red clump stars. Overplotted is the best fit Gaussian curve with the mean RC color.

$(J - K_s)$ color distribution is then used to determine the mean color of the red clump, as shown in Fig. 4.5. For a $4' \times 4'$ region in Baade’s Window centered on coordinates $\alpha_{2000} = 18 : 04 : 51.2$ and $\delta_{2000} = -30 : 03 : 26.5$, VVV photometry yields a $(J - K_s) = 0.96$ mag. Using the measured extinction of this field of $E(B - V) = 0.55 \pm 0.01$ mag (Sumi 2004; Kunder et al. 2008; Zoccali et al. 2008), we obtain a dereddened mean color of $(J - K_s)_0 = 0.68$ for the RC stars in this region. We use this value as a reference for the intrinsic mean color of the RC, and its difference with respect to the measured RC color in any other region will be an indicator of extinction, meaning $E(J - K_s)$. In the next chapter, we use this technique to obtain a the complete extinction map of the Bulge for the VVV survey region.

4.2.2 The absolute magnitude of the red clump

The dereddened RC magnitudes can then be used in to derive the mean distances for each of our subfields through comparison of the measured values with the intrinsic RC magnitude for a 10 Gyr, near-solar metallicity population, of $M_{K_s} = -1.55$ based on Pietrinferni et al. (2004)

Teramo stellar evolution models (see also van Helshoecht & Groenewegen 2007). As we already discussed in the case of the reddening calculations, the assumption of homogeneous stellar populations on the bulge are the main source of uncertainties. The intrinsic magnitude of the RC is known to have a dependence on age and metallicity (Salaris & Girardi 2002; Pietrzyński et al. 2003). Teramo stellar evolution models indicate that a 0.2 dex variation in metallicity would affect the intrinsic magnitude of the RC by ~ 0.10 mag, consistent as well with Salaris & Girardi (2002). If for a solar metallicity population at 8 kpc from the Sun we assume a main metallicity 0.20 dex lower, our method will result in measurement of distance of ~ 8.2 kpc instead. Therefore, although this introduces a small error into our calculations we are still able to trace the large scale structure of the bulge.

Chapter 5

The extinction towards the Milky Way bulge

The Bulge is one of the major components of the Galaxy and it can be studied at a unique level of detail, in comparison to those of external galaxies, thanks to its proximity which enables properties of individual stars to be measured. Bulge stars hold the imprints of how our Galaxy formed and evolved. The Bulge star formation and chemical enrichment history can be investigated in detail through analysis of stellar ages and chemical abundances (McWilliam & Rich 1994; Zoccali et al. 2003; Fulbright et al. 2007; Rich et al. 2007; Lecureur et al. 2007; Zoccali et al. 2008; Clarkson et al. 2008; Brown et al. 2010; Bensby et al. 2010b, 2011; Johnson et al. 2011; Gonzalez et al. 2011b, chapter 3 of this thesis).

Our current understanding of the Milky Way Bulge structure and stellar content can be summarized as follows: i) the Bulge structure is dominated by the Bar (Stanek et al. 1994) which appears to have a peanut or X-shape in the outer regions (McWilliam & Zoccali 2010; Nataf et al. 2010; Saito et al. 2011); ii) there is a radial stellar metallicity gradient (Zoccali et al. 2008; Johnson et al. 2011) that most likely flattens in the inner regions (Rich et al. 2007); iii) in addition to the population associated with the bar, there are hints for a second chemically and kinematically distinct component (Babusiaux et al. 2010; Hill et al. 2011; Gonzalez et al. 2011b; Bensby et al. 2011); and iv) the bulge is dominated by old stars (Zoccali et al. 2003; Brown et al. 2010; Clarkson et al. 2011), although there are indications for a possible younger population of metal-rich stars as traced by Bulge microlensed dwarfs (Bensby et al. 2011). However, the general view of these properties, based on a more complete coverage, is expected to provide the final picture of the Milky Way bulge formation history. Several projects aiming to obtain this general view of the Bulge are either ongoing or planned for the near future (e.g. Minniti et al. 2010; Feltzing 2011; Ness & Freeman 2012; Elia Garcia Perez et al. 2012). The interpretation of these observations is challenged by the variations in the dust extinction properties on small scales towards the different Bulge regions.

The currently available extinction maps of the Bulge regions have different resolutions and coverages. The most commonly used extinction maps were those of Burstein & Heiles (1982), later superseded by Schlegel maps (Schlegel et al. 1998). The Schlegel extinction maps are full-sky maps of the dust color temperature based on IRAS and DIRBE experiments which are then

normalized to $E(B-V)$ values using a calibration of colors of background galaxies. Unfortunately, these maps suffer from large uncertainties in regions towards the Bulge. Specifically, as stated in the appendix C of Schlegel et al. (1998), the temperature structure of the Galaxy towards latitudes $|b| < 5^\circ$ is not well defined and contaminating sources have not been completely removed. Furthermore, as we show below, the resolution of these maps is too coarse. As a result, the Schlegel reddening values towards the Bulge are unreliable.

Clearly, an extinction map covering $|b| < 5^\circ$, with sufficient resolution to resolve the small spatial scale variations of extinction, is important for an understanding of the general properties of the inner Galactic regions. Using red giant branch (RGB) stars from the near-IR photometric survey DENIS, Schultheis et al. (1999) provided a high resolution ($2'$) map in the inner regions of the Bulge ($|b| < 2^\circ$). This map provides the sufficient resolution to analyze such inner Galactic regions, but its coverage is too limited to permit the study of the *global* Bulge stellar populations and structural properties.

More recently, Marshall et al. (2006) provided a full 3D extinction map of the Bulge. 3D maps are indeed of high importance for Galactic studies towards the inner Galaxy as they hold the additional distance information. However, in order to build 3D extinction maps, a sufficient number of stars is required in each resolution element, which implies that only a modest resolution can be achieved. The method in Marshall et al. (2006) is based on a comparison of 2MASS photometry to the Besançon model (Robin et al. 2003). At low Galactic latitudes ($|b| < 3^\circ$) 2MASS suffers strongly from incompleteness and blending due to too low resolution and high stellar density, limiting the ability to derive correct star counts and extinction. The resolution of Marshall's 3D extinction map is $15'$, which is again too coarse to fully overcome the differential reddening problems at lower latitudes $|b| < 4^\circ$.

Other important extinction maps are available with a partial coverage of the Bulge such as those of Kunder et al. (2008) and Sumi (2004). However, for detailed studies of the Bulge, a high resolution and homogeneous extinction map covering the complete area of interest is missing. The deep and near-IR photometry of the VVV ESO public survey of the Bulge (Minniti et al. 2010) provides the ideal dataset to create such a map. We describe here an effective technique, based on the color of red clump (RC) stars, to trace the effects of extinction (published in Gonzalez et al. 2011a, later referred to as Paper I). This technique is then used to analyze the complete Bulge region covered by the survey and derive the first complete extinction map of the Bulge, using a homogeneous population, at a resolution of $2'$ – $6'$. We compare our map to extinction maps in the literature in the corresponding overlap regions (Sect. 5.2), and we discuss the importance of high resolution extinction map in future Bulge studies (Sect. 5.3).

5.1 Determination of A_K values and the complete extinction map of the Bulge

We computed the mean RC ($J-K_s$) color in small subfields towards the complete Bulge region of VVV. We adapt the resolution to provide a sufficient number of RC stars (> 200) to populate the color distribution with enough statistics, and at the same time to minimize the effect of differential

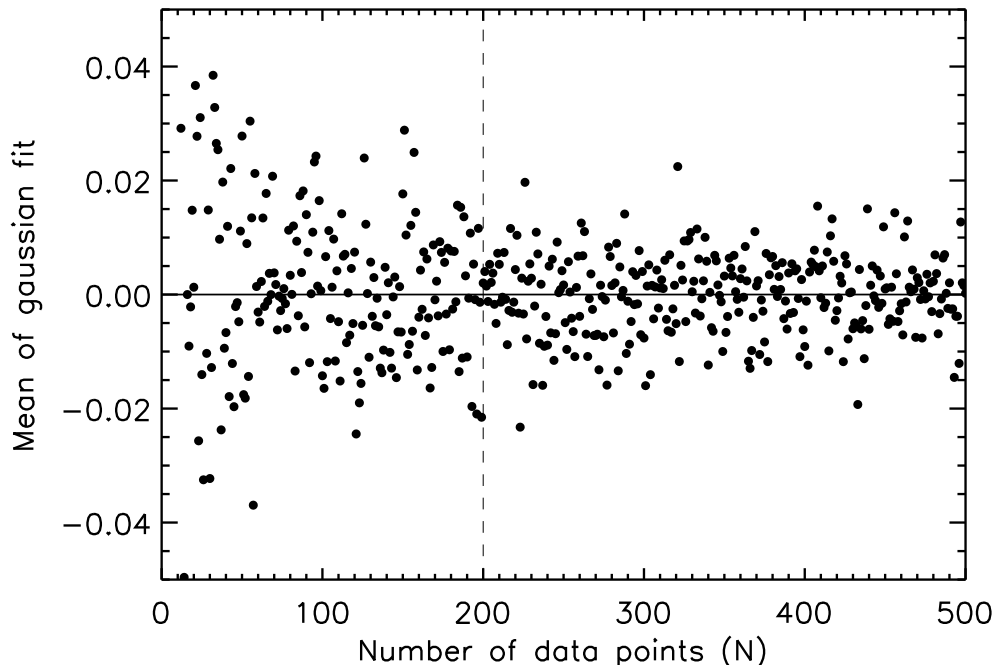


Figure 5.1: The mean value obtained from a Gaussian fit to a set of N data points randomly distributed following a Gaussian distribution centered on zero (solid horizontal line) and with a sigma of 0.10. The dashed vertical line shows the limit of 200 points adopted as the minimum number of stars in each subfield.

extinction as discussed in Paper I. The minimum number of 200 stars for each subfield was determined following the result shown in Fig. 5.1. The vertical axis of Fig. 5.1 shows the mean value obtained from a Gaussian fit to a set of N random values that follow a Gaussian distribution centered on zero and with a sigma of 0.10. The vertical dashed line shows the limit of 200 stars. The dispersion on the mean value from the Gaussian fits increases significantly for a number of data points below this limit. The resulting resolution of the complete map depends on latitude, as shown in Fig. 5.2. For the latitude range $-3.5^\circ < b < +5^\circ$ the density of Bulge stars allowed the highest resolution of $2'$ to be used. As the density of Bulge stars drops at higher distances from the plane, the resolution had to be reduced to $4'$ for $-7^\circ < b < -3.5^\circ$ and to $6'$ for $-10^\circ < b < -7^\circ$. The mean measured RC color is compared to the intrinsic value measured in Baade's Window to derive the reddening value $E(J - K_s)$. From $E(J - K_s)$, the A_{K_s} extinction values are obtained by applying a specific extinction law.

A zoom in the CMD centered on the red clump region in the tile b306 at $l \sim -0.25$, $b \sim -2$ is shown in Fig.5.3. The reddening determination was done in subfields of $2' \times 2'$ and this reduces the spread in color of the RC stars in the full $1.5 \times 1 \text{ deg}^2$ tile region, after applying the reddening correction, as shown in the right panel of Fig.5.3.

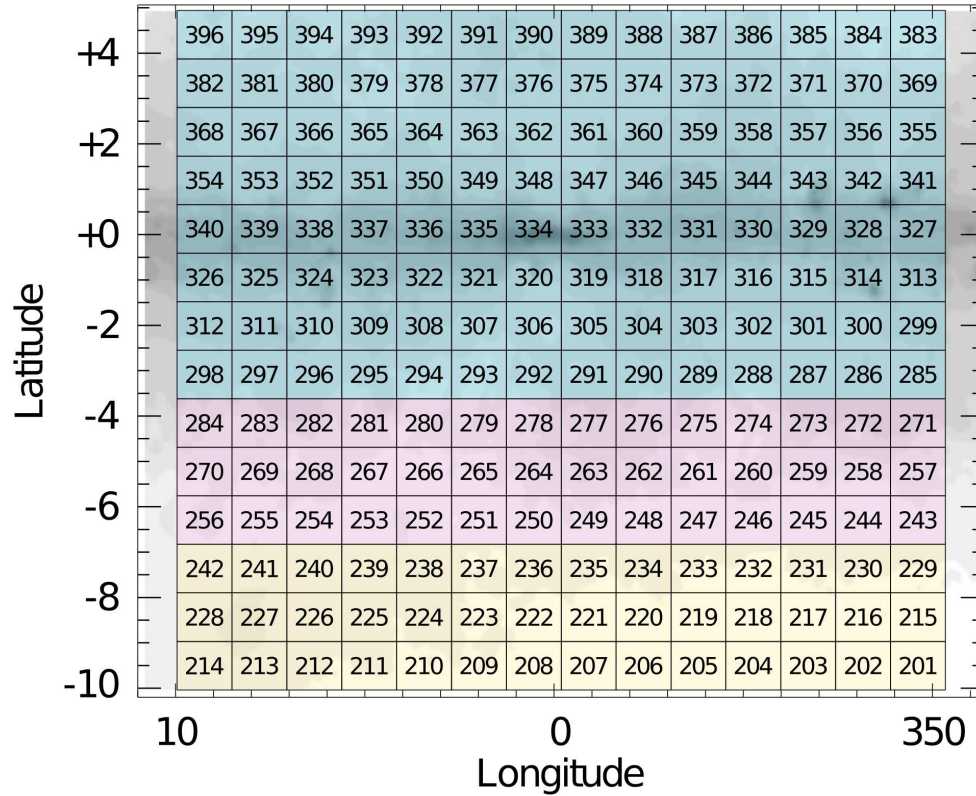


Figure 5.2: VVV coverage of the Bulge in Galactic coordinates. Each small square shows the coverage by individual $1^\circ \times 1.5^\circ$ tile from the VVV. Tile numbering for the VVV survey is described in Saito et al. (2012) and the coordinates of the center of each tile are listed in the Appendix B. The different color shading of the tiles depends on the spatial resolution ($2'$, $4'$ and $6'$, respectively) used to derive reddening from the mean color of the red clump stars (see text for details).

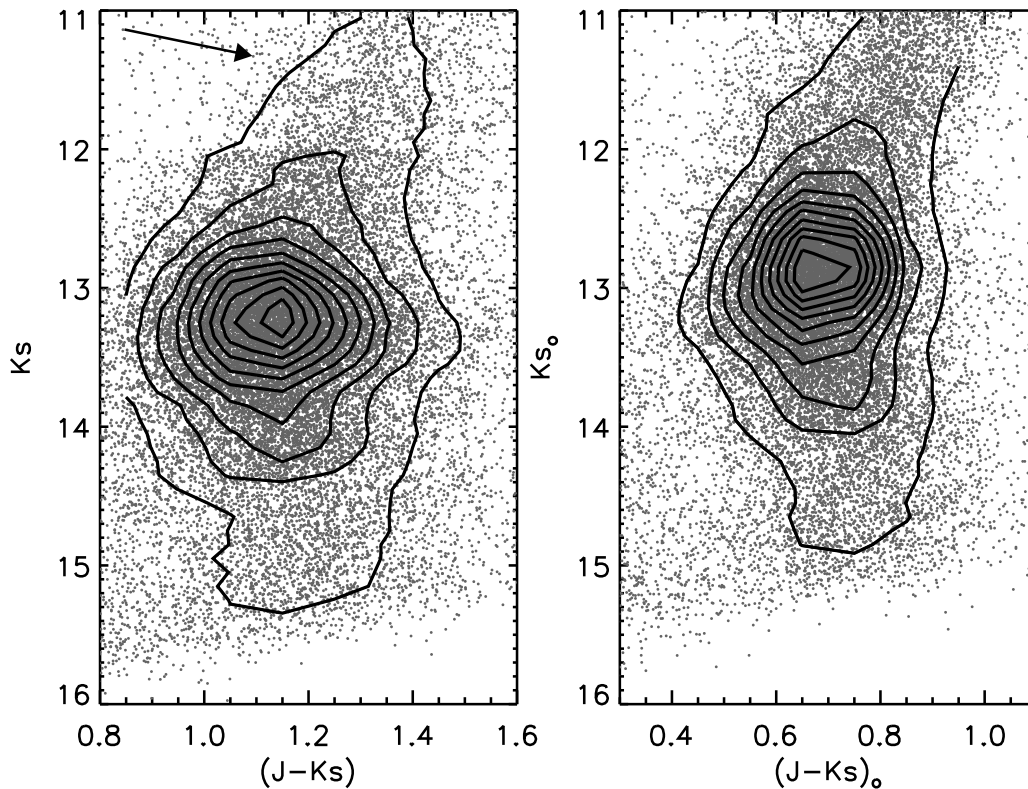


Figure 5.3: Red clump region of the observed color magnitude diagram for tile b306 (right panel) compared to the de-reddened one obtained by our procedure (left panel). Only a subsample of the stars are plotted in each CMD and contour levels are shown to mark the clump position and shape. The arrow in the right panel shows the reddening vector for a change in $E(B-V)$ of 0.5 magnitudes.

Figure 5.4 shows the complete A_{K_s} extinction map for the Bulge VVV region based on Cardelli et al. (1989) extinction law. The extinction variations in the inner 2° from the Galactic plane are better appreciated in the upper panel of Fig. 5.8 where the highest values of extinction reach $A_{K_s} = 3.5$.

In a small number of regions the differential reddening is too strong even over $2'$ resulting in large errors for reddening measurements, or even in extreme cases preventing the identification of RC feature. Some of these regions are visible as small white dots/squares in the upper panel of Fig. 5.8. They are less obvious in Fig. 5.4, because of the resampling in the inner most regions in the presentation of the figure. All these regions are clearly identified as having large errors in our extinction database.

Our extinction maps show clearly the small scale variations, as produced by the strong dust features traced, in particular at low latitudes. These features are now seen in great detail thanks to the high resolution and large coverage of our study.

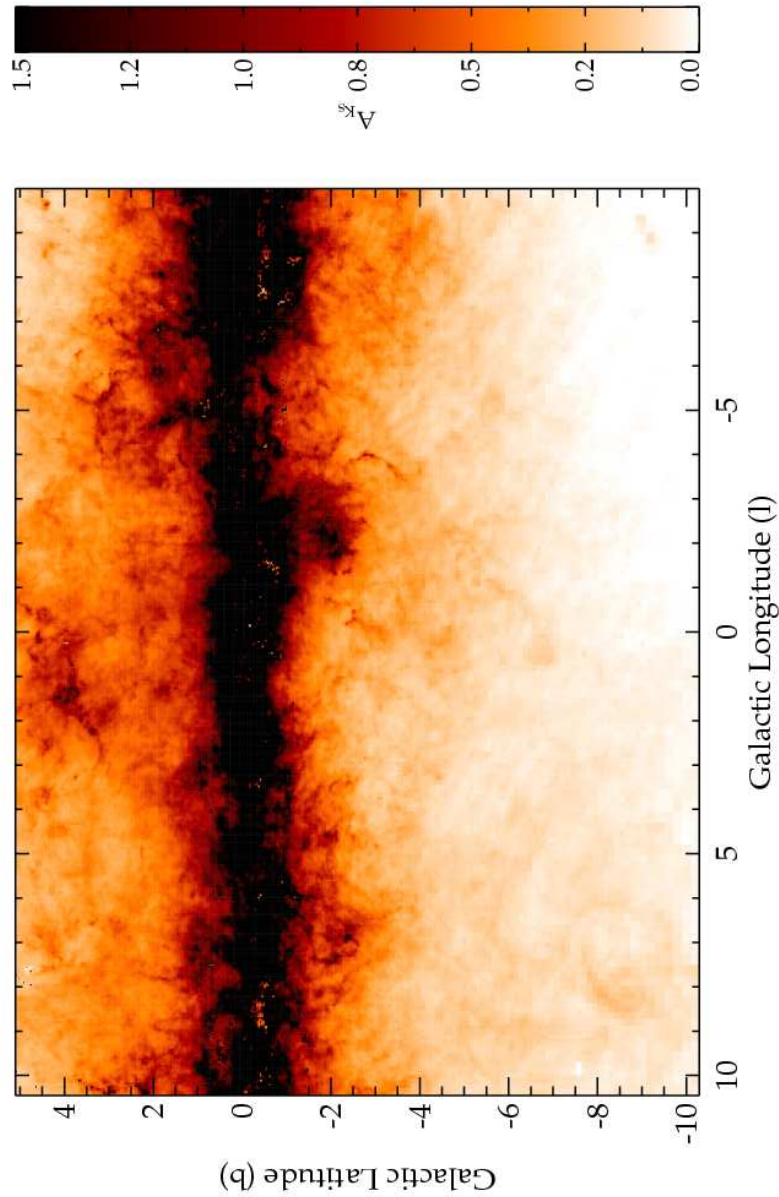


Figure 5.4: Extinction map of the Galactic Bulge for the complete region covered by the VVV survey. The A_{K_s} values are computed from $E(J - K_s)$ measurements assuming Cardelli et al. (1989) extinction law for all tiles. At A_{K_s} values larger than 1.5 mag the color scale saturates. The details of the extinction variation in the inner highly extinct regions, where A_{K_s} reaches up to 3.5 mag, are better seen in the upper panel of Fig. 5.8.

5.1.1 A note about the extinction law

At present, there is no real consensus on which is the correct extinction law to be used for studies towards the inner Galactic bulge. Reddening maps are related to a given extinction law which can vary between different studies. Recent results suggest that extinction properties might vary in different locations and possibly depend on the amount of extinction and dust properties. In particular, Nishiyama et al. (2006, 2008, 2009) presented a detailed study of the interstellar extinction law towards the inner regions of the Bulge ($|l| < 2^\circ$, $|b| < 1.0^\circ$) concluding that this varies significantly depending on the line of sight.

Nishiyama et al. (2006) also provided ratios of total to selective extinction which differ from a $R_V \sim 3.1$ standard extinction law as obtained towards other regions.

The problem of the correct extinction law towards the Galactic bulge is not addressed here, but will be part of another article (Chen et al. 2012, in prep) based on GLIMPSE and VVV datasets. However, in order to obtain extinction values from the reddening map presented here, $E(J - K_s)$ values need to be transformed into an absolute extinction through a given extinction law. Here, we decided to adopt two different extinction laws. The first is the more commonly used extinction law from Cardelli et al. (1989). Adopting 1.240, 1.664, 2.164 micron as the effective wavelengths of a K2 giant (typical of red clump stars) for 2MASS from Indebetouw et al. (2005), the coefficients corresponding to the Cardelli et al. (1989) extinction law are:

$$A_J = 1.692E(J - K_s) \quad (5.1)$$

$$A_H = 1.054E(J - K_s) \quad (5.2)$$

$$A_{K_s} = 0.689E(J - K_s) \quad (5.3)$$

The second is the extinction law from Nishiyama et al. (2009):

$$A_J = 1.526E(J - K_s) \quad (5.4)$$

$$A_H = 0.855E(J - K_s) \quad (5.5)$$

$$A_{K_s} = 0.528E(J - K_s) \quad (5.6)$$

which has been determined, for the 2MASS photometric system, in the inner regions of the Bulge closer to the Galactic plane.

In order to test which extinction should be preferred, we performed the following exercise. We measured the colors $(J - K_s)$ and $(J - H)$ in our 4' control field in Baade's window, where we find mean values of $(J - K_s) = 0.96$ and $(J - H) = 0.73$. We then measure these colors for a set of regions with different latitudes and compare them to those in our control field. The $E(J - K_s)$ and $E(J - H)$ color difference for each line of sight are shown in Fig. 5.5. The relation between these color differences can be obtained from the corresponding coefficients of each extinction law. Our

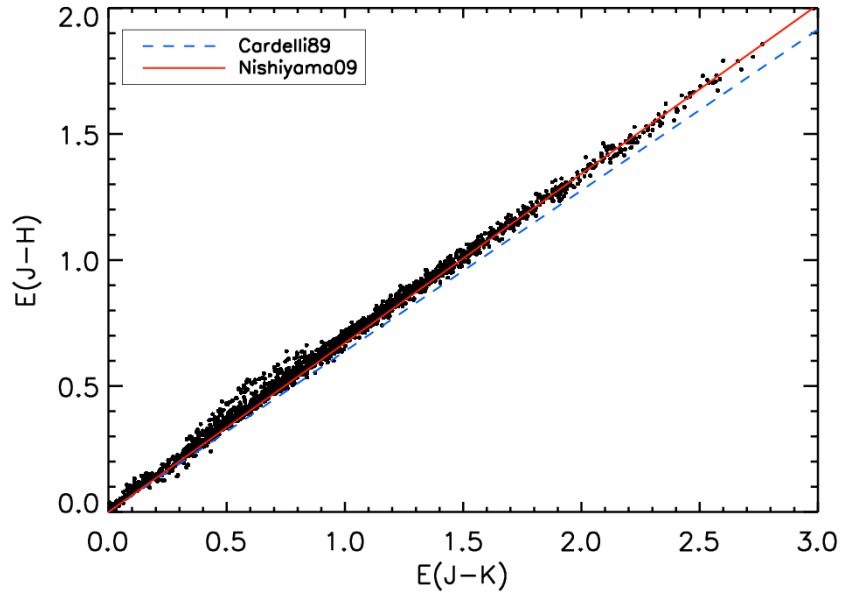


Figure 5.5: $(J - K_s)$ and $(J - H)$ color difference between our control field and those measured in the subfields of tiles b317, b303 and b275. The size of the subfields corresponds to the same resolution described in Fig. 2. The blue dashed line shows the relation $E(J-H) = 0.638E(J-K_s)$ corresponding to the extinction law from Cardelli et al. (1989) and red solid line to $E(J-H) = 0.671E(J-K_s)$ from Nishiyama et al. (2009)

Welcome to BEAM:
A VVV and 2MASS Bulge Extinction And Metallicity Calculator

[back to Oscar A. Gonzalez Homepage](#)

EXTINCTION MAPS.
 Calculates the mean **EXTINCTION** A_K based on the method described in [Gonzalez et al. 2011](#) and [Gonzalez et al. 2012](#). As described in the article, A_K extinctions are calculated using coefficients from Cardelli et al. 1989 and the user should use those to remain consistent. $E(J-K_s)$ values are also returned so that the user can adopt a different extinction law if required. A_K values using Nishiyama et al 2009 can also be obtained. Be aware that extinction maps have a maximum resolution of 2 arcmin and are insensitive to variations on smaller scales.
 A description of the extinction law and corresponding coefficients [HERE](#).
 All regions now have open access as published in Gonzalez et al. 2012: $0.2 \leq l \leq 1.7$ and $-8 \leq b \leq 0.5$
 Please contact O. A. Gonzalez if you request any additional information (ogonzalez AT eso.org).

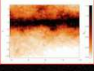
Single target

l (deg):
 b (deg):
 Box size ("):
 Extinction law:

Upload a file

File:
 NOTE: Each line in the file must have the following format:
 l(deg) b(deg) boxsize(") N
 where N=1 means Cardelli89 and N=2 means Nishiyama09

Here is an image of the complete reddening map.
 Note that it is saturated at $A_K=1.5$ for visualization.



METALLICITY MAPS:
 Calculates the mean **METALLICITY** based on [Gonzalez et al. 2011](#). Extinctions were calculated using extinction laws from Cardelli et al. 1989 and the $(J-K_s)$ colors of RGB stars where used to derive $[Fe/H]$ by interpolation between globular cluster ridge lines from Valenti et al. 2007.
 Note that metallicities are only significant within a reasonable box size (≈ 30 arcmin)
 IMPORTANT: Maps are still under construction. Last update 28/07/2011. Maps covering $0.2 \leq l \leq 1.7$ and $-8 \leq b \leq -3$

Single target

l (deg):
 b (deg):
 Box size ("):
 Password: * Required for querying new public regions

Upload a file

File:
 Password: * Required for querying new public regions
 NOTE: Each line in the file must have the following format:
 l(deg) b(deg) boxsize(")

Figure 5.6: Screen-shot of the BEAM calculator web-page. The user provides the center coordinates and field size to retrieve the reddening values and/or photometric metallicities.

measurements are in good agreement to those with the Nishiyama et al. (2009) extinction law, where $E(J-H) = 0.671E(J-K_s)$. However, since the implications discussed in Sect. 5.3 do not depend strongly on the adopted extinction law, we proceeded our analysis following the more commonly used law from Cardelli et al. (1989).

5.1.2 BEAM calculator

As described in the following, our high resolution extinction map of the Bulge provides a valuable tool for future studies. In order to make it available to the community, we developed a web based tool named BEAM (Bulge Extinction And Metallicity) calculator Fig. 5.6¹. This tool, provides the user with an easy access to our measurements, both for the extinction values presented here, as well as for the photometric metallicities. The complete metallicity map and its analysis is the subject of Chapter 7 (Gonzalez et al. 2012, in preparation).

The tool allows the user to input a set of coordinates and the corresponding size of the field of interest, retrieving the mean extinction (A_{K_s}) towards these set of coordinates. The extinction values are computed using either Cardelli et al. (1989) or Nishiyama et al. (2009) extinction law.

¹<http://mill.astro.puc.cl/BEAM/calculator.php>

However, the measured $E(J - K_s)$ values are always provided as well, so that the user can adopt any other extinction law of preference.

5.2 Comparison with existing extinction maps of the Bulge

Other studies have addressed the problem of extinction towards the Bulge. Reddening maps providing a similar Bulge coverage as the one presented here are the 3D maps of Marshall et al. (2006) and the Schlegel et al. (1998) maps. As described in the introduction, it is well known that Schlegel maps are not trustable for regions closer to the galactic plane ($|b| < 5^\circ$) due to contaminating sources and uncertainties in the dust temperatures. In order to quantify these effects, we compared our extinction values to a set of lines of sight at different latitudes. We retrieved A_V values from the Schlegel maps for 1000 regions of $30' \times 30'$ size, randomly distributed across latitudes of $-8^\circ < b < -1^\circ$ for $0^\circ < l < 2^\circ$. Although the relative difference between A_{K_s} values from Schlegel maps and ours will not depend on the adopted extinction law, we converted their A_V values into A_{K_s} following Cardelli et al. (1989) law and then retrieved our own A_{K_s} values from the BEAM calculator for the same target fields, again selecting the Cardelli et al. (1989) extinction law. Figure 5.7 shows the comparison between our extinction results and those of Schlegel et al. (1998) as a function of latitude. The difference is already visible at $b < -6^\circ$ and becomes much larger for latitudes closer to the plane. Interestingly, we observe a negative difference between our A_{K_s} values and those of Schlegel et al. (1998) for $b < -2^\circ$ while it becomes positive at $b > -2^\circ$. The source of this sign variation is not obvious given the uncertainties in the Schlegel maps at those latitudes.

Marshall et al. (2006) provide an extinction map for the complete Bulge, obtained by comparing the 2MASS photometry to the Besançon model, including the model dependent extinction as a function of distance in each line of sight. Unfortunately, this technique only allows to calculate the maps with a lower resolution ($15'$), which is insufficient to resolve the small scale extinction variations in the inner Bulge regions.

Studies of Schultheis et al. (1999, 2009) provided very high resolution maps ($2''$), obtained using DENIS and Spitzer data respectively for the inner $|b| < 2^\circ$. Since in these regions the small scale extinction variations become particularly strong, these datasets are ideal to compare with our extinction maps and study possible systematics between the methods. The Spitzer map of Schultheis et al. (2009) covers specifically the $\sim 1^\circ$ of the very central regions of the Galaxy. This region is also included in the DENIS map and the extinction derived from DENIS and Spitzer observations agree very well.

In order to produce the DENIS extinction maps, Schultheis et al. (1999) used a method based on comparison of bulge RGB colors in $2'$ subfields with model isochrones from Bertelli et al. (1994). They adopted a Solar metallicity population at a distance of 8 kpc with an age of 10 Gyr in the model isochrones. Same process was adopted to produce the Spitzer extinction maps from Schultheis et al. (2009). This method has the benefit of using the bright Bulge stars, thus minimizing problems arising from photometric errors and (in-)completeness. However, the colors of RGB stars are much more strongly affected by population effects, in particular metallicity and to less extent age, when compared to RC stars in our method. In fact, the color of RGB

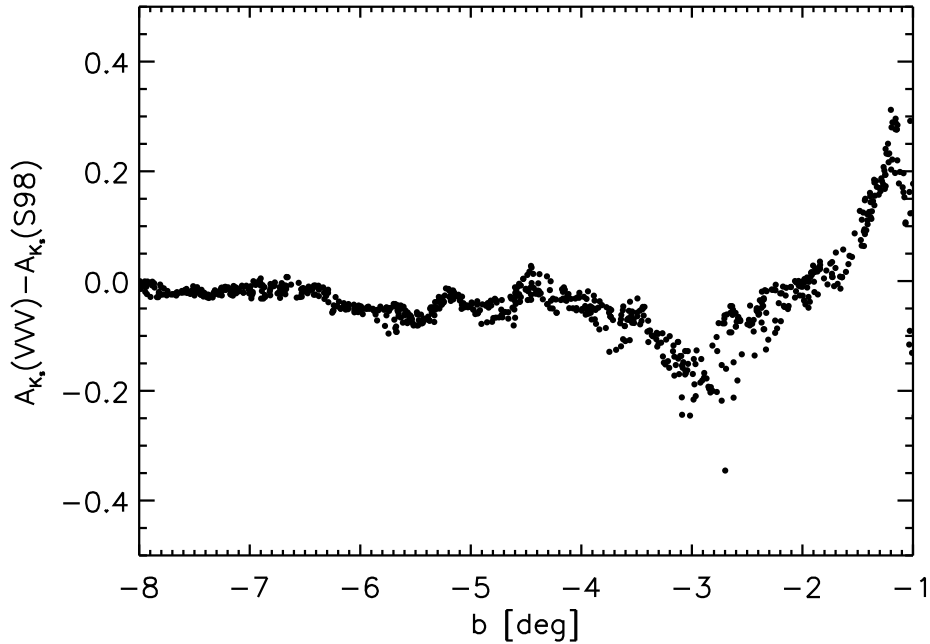


Figure 5.7: Difference between the A_{K_s} values obtained in this work and those of Schlegel et al. (1998), as a function of Galactic latitude, for 1000 randomly distributed $30' \times 30'$ regions between $(-8^\circ < b < -1^\circ)$.

stars is frequently used to derive the metallicity distribution function of stellar populations when spectroscopy of individual stars is not available.

The extinction maps of Schultheis et al. (1999), based on the magnitudes of RGB and AGB stars, were produced at latitudes $b < 2^\circ$ where no or only very weak metallicity gradient seems to be present (Rich et al. 2007). Thus, extinctions obtained from isochrone comparison to red giant stars should be reliable for the regions studied by Schultheis et al. (1999) with errors dominated by the distance uncertainty of the RGB population towards each line of sight. However, this method would have a considerable problem when used to construct a global extinction map, such as the one presented here.

Figure 5.8 compares our extinction map with that of Schultheis et al. (1999) using DENIS photometry. A_V values from Schultheis et al. (1999) were converted to A_{K_s} following the extinction law of Cardelli et al. (1989) for comparison purposes. Their similarity is remarkable, with both maps tracing the same dust concentrations in the inner regions. We can also directly compare the extinction values retrieved from the BEAM calculator to those of Schultheis et al. (1999) and Schultheis et al. (2009). This comparison is shown in Fig. 5.9. A_{K_s} values of both methods are in good agreement with a scatter of the order of 0.2 mag, which is expected from the different methods and photometric errors. The scatter becomes larger, up to 0.6 mag, in the regions of higher extinction ($A_{K_s} > 2$), where for a significant number of lines of sight we find a lower extinction value than Schultheis et al. (2009). A possible explanation for this difference is that, in these highly reddened regions, the extinction is large enough to bring RC stars to magni-

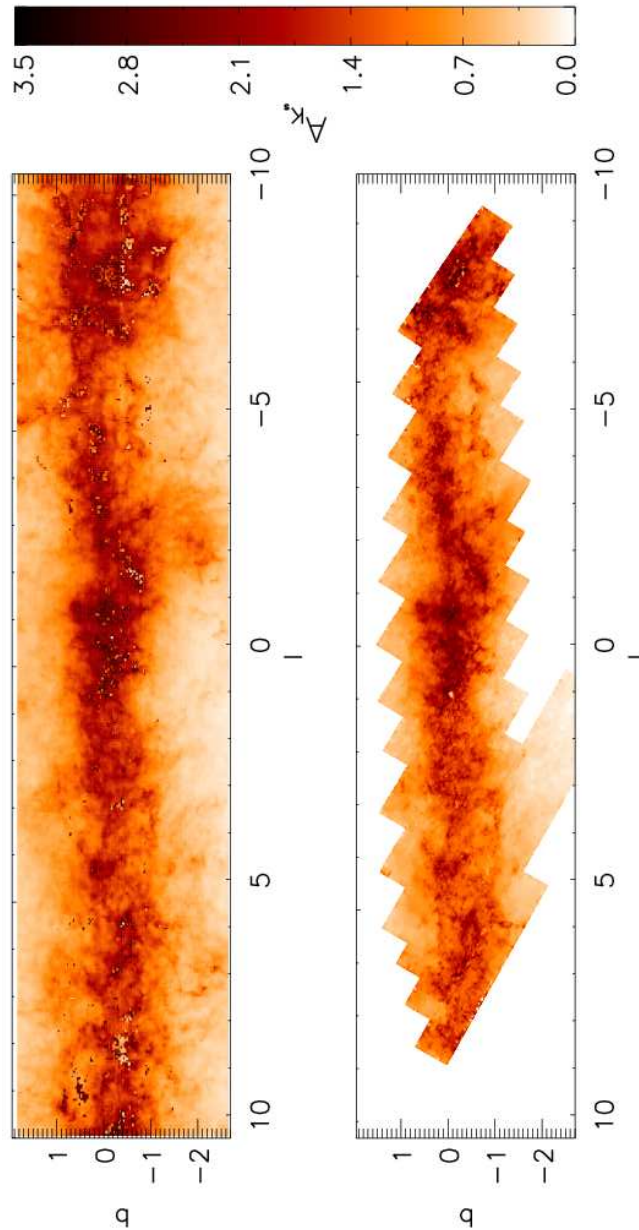


Figure 5.8: The upper panel shows the inner $\sim \pm 2^\circ$ region around the Galactic plane of our VVV extinction map. A_{K_s} values are based on Cardelli et al. (1989) extinction law. Part of this region was also covered by the DENIS survey, used in Schultheis et al. (1999) to build an extinction map shown in the lower panel.

tudes fainter than $K_s \sim 17$ where the completeness of VVV is of the order of 60% (Saito et al. 2012) and therefore our reddening values could be underestimated. However, we emphasize that this difference is observed in the inner $1^\circ \times 1^\circ$ of the Bulge where extinction determinations are certainly more complicated. Moreover, the overall agreement is remarkable considering the different techniques, data sets and stellar populations (RC vs RGB) of our studies.

5.3 Implications for Bulge studies

Extinction corrections are a fundamental parameter for essentially all studies of stellar populations, as well as for distances and the determination of structural parameters. In this section we highlight the advantages provided by our new high resolution and large area extinction map for the studies of color magnitude diagrams and for determination of stellar parameters in spectroscopic abundance studies. We also discuss the determination of distances and the study of the Bulge structure which is the subject of Chapter 6.

5.3.1 The Color-Magnitude diagram of the inner Bulge

The VVV color magnitude diagrams are de-reddened using our new extinction map of the Bulge. In Figure 5.10 we compare the observed, extinction corrected, inner Bulge CMD with the predictions from the population synthesis model of the Milky Way from the Besançon group including the thin disk, thick disk and bulge populations. This model is described in detail in Robin et al. (2012). It uses the Marshall et al. (2006) extinction map and when compared with the observations such as 2MASS star counts it can be used to study the structure of the Milky Way. As already mentioned above, in the innermost regions of the Bulge, 2MASS is severely incomplete and affected by strong crowding and blending, thus limiting the predicting power of the model in the inner regions. With the superior spatial resolution of VVV survey (median seeing is better than $0.9''$ in J , H and K_s images) and its deeper photometry, it is now possible to make direct comparisons with the simulations and thus validate some of the assumptions adopted in the model.

Figure 5.10 shows an observed HESS diagram of a $40' \times 40'$ region centered at Galactic coordinates $(l, b) = (1.0, -1.0)$ (VVV tile b320) in the left panel. In the right panel is the CMD obtained from the Besançon model for the same region. There is a remarkable similarity between our dereddened data and the model. The major difference is for the blue plume of stars at $(J - K_s)_0 \sim -0.2$ in the left diagram, which is much stronger, brighter, and bluer in the VVV CMD, than the blue sequence at $(J - K_s)_0 \sim 0.1$ in the model. This part of the CMD contains the disk stars, which are found all along the line of sight towards the Bulge, and therefore they have a range of reddening values, some having significantly lower reddening than derived for the Bulge red clump stars. Therefore after applying the extinction correction appropriate for the Bulge stars the colors of the disk stars cannot be correctly reproduced in our CMDs, but the colors and magnitudes of the major Bulge features, the RC and the RGB are in excellent agreement with the model. This provides evidence that VVV dereddened color-magnitude diagrams can be used to investigate the stellar populations properties, such as age and metallicity distributions

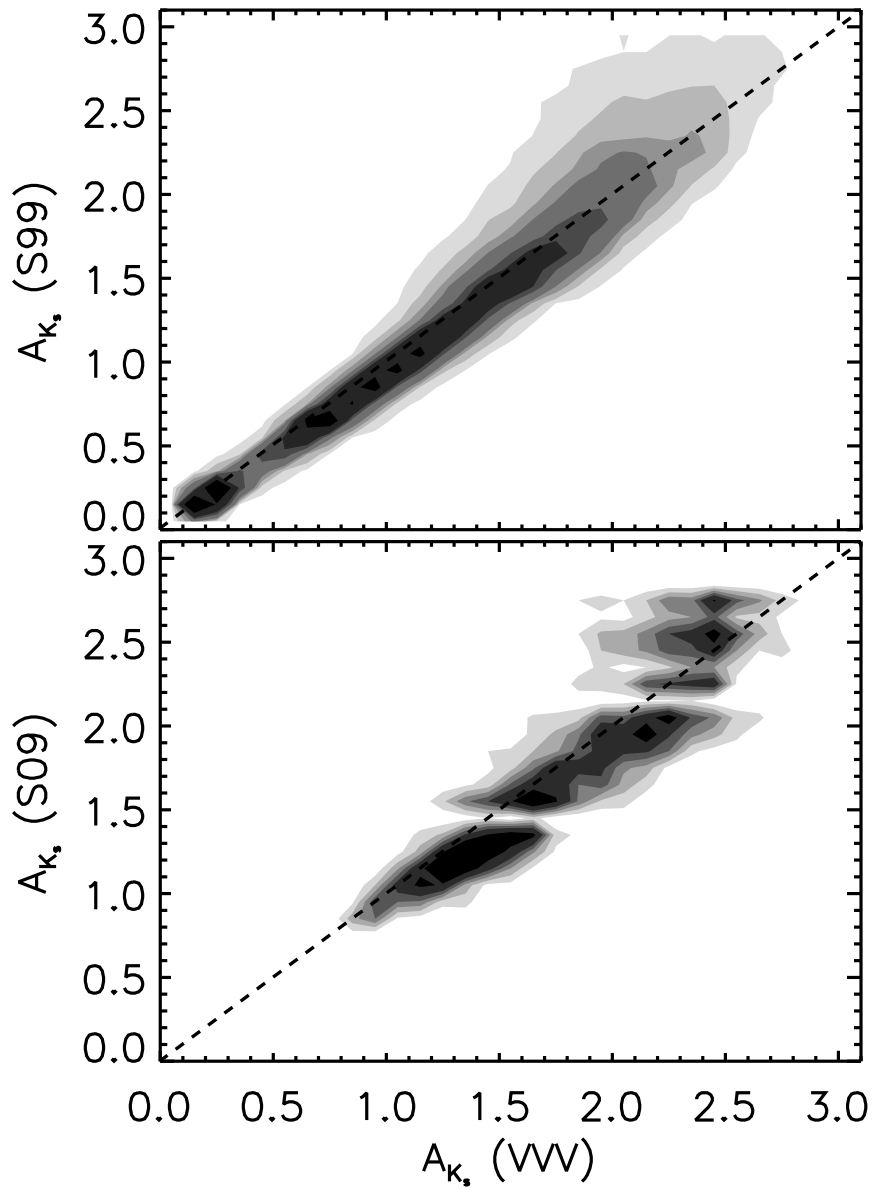


Figure 5.9: Upper panel shows the comparison of the A_{K_s} values obtained in this work and those of Schultheis et al. (1999) for the common inner Bulge region ($-2^\circ < b < +2^\circ$). Lower panel shows the comparison with the SPITZER extinction map of Schultheis et al. (2009) for the central 1° of the Galaxy. Both plots are shown as density contours due to huge number of data points.

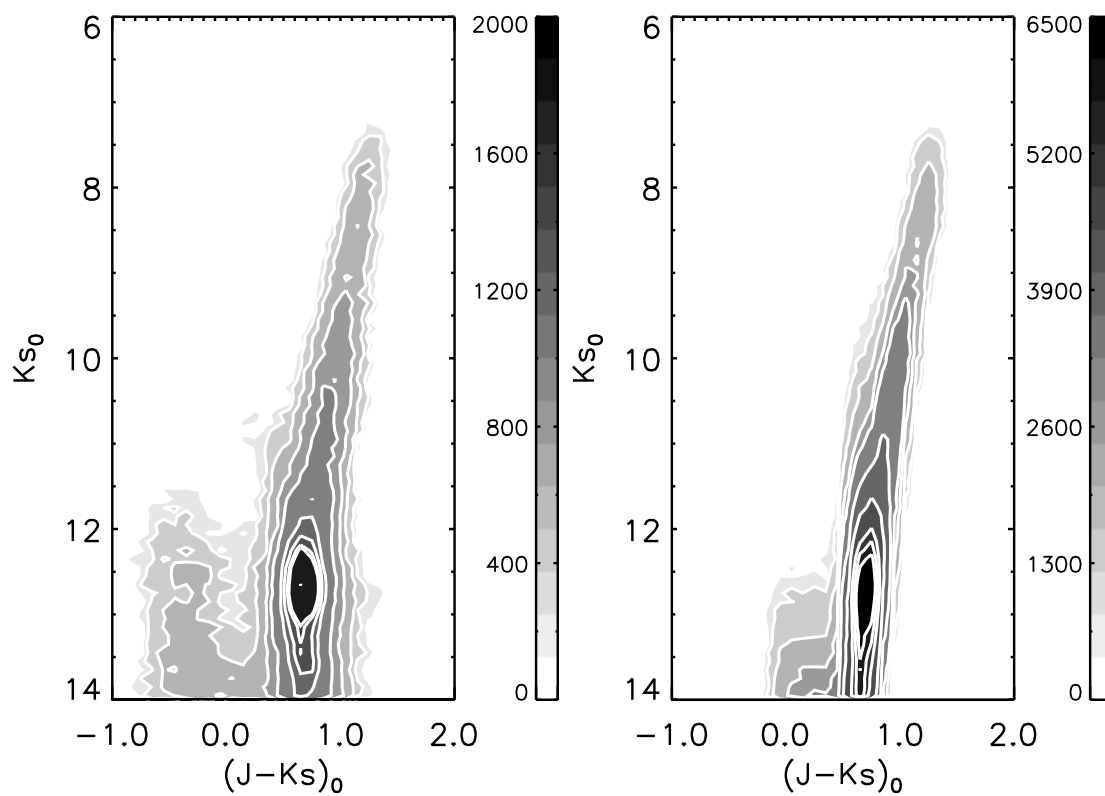


Figure 5.10: Left panel shows the VVV observations based HESS diagram of a 40' region in the inner Bulge $(l, b) = (-1.0, -1.0)$. The right panel shows the diagram for the same region as obtained from the Besancon model.

of stars even in the inner Bulge regions. Additionally, the good agreement between the model and the observations indicates that we could use the Besançon model in comparison to observed VVV data, in order to obtain 3D extinction maps such as the one from Marshall et al. (2006). The high spatial resolution and photometric depth of VVV CMDs offer the possibility to derive the 3D extinction map of the Bulge with a resolution of up to 6' for the inner regions (Chen et al. 2012, in preparation). Although this resolution, limited by the number of stars needed for the comparison, is lower than that of the map presented here, it will add the important 3D information, allowing more accurate characterization of the structure in the inner Bulge.

5.3.2 Photometric effective temperatures

Low and intermediate resolution spectroscopic studies, where determination of stellar parameters is based on photometric properties of the targets, depend on the adopted extinction corrections. In particular, the critical parameter is the effective temperature which is derived from the color of the stars. Current studies of the Bulge use multi-object fibre spectrographs with large field of view in order to observe simultaneously large number of targets. The field of view can range from 25' radius for the FLAMES spectrograph on the VLT (Pasquini et al. 2003) to 2° field of AAOmega multifibre spectrograph at the AAT (Sharp et al. 2006). Assuming that a single value of extinction is adopted for a single pointing, using our 2' resolution extinction map we can estimate the differential extinction in a typical region of say 30' and derive the effect on the corresponding effective temperatures determined from colors of stars.

The relative effect of differential reddening will not depend significantly on the adopted calibration, and in our experiment we use the photometric calibration from Ramirez & Melendez (2005) for giant stars. A typical Bulge K giant star will have Solar metallicity with an effective temperature of around 4500 K. According to the calibration from Ramirez & Meléndez (2005), this star will have an intrinsic color of $(V - K_s)_0 = 2.625$. We now consider a 30' region located at a latitude of $b = -4^\circ$ along the minor axis ($l = 0^\circ$) and retrieve the extinction values using our BEAM calculator for a set of 200 randomly distributed positions within this region. These individual extinctions will differ from the mean extinction for the whole region depending on the amount of the differential extinction. If we add this difference to the intrinsic color of the star and use the new color to calculate the corresponding effective temperature from the photometric calibration, we obtain an estimation of the effect of differential reddening when adopting a single reddening value for the whole region. The difference between the original effective temperature and the one obtained after including the effect of differential extinction is shown in Figure 5.11 as a function of the variation in A_{K_s} . The amount of extinction A_{K_s} varies by 0.10 mag in the 30' region, which produces an error of up to 300 K in effective temperature. This effect becomes even more important in regions of higher extinction than Baade's Window as shown for the case at latitude $b = -2^\circ$ (red circles in Fig 5.11). Here a 0.30 mag extinction variation is observed within the 30' region which implies errors larger than 600 K in the derived photometric effective temperature.

Clearly all studies relying on photometric determination of the effective temperature need to take these extinction variations into account and correct for them. Otherwise the strong differential reddening in the inner Galaxy may result in large errors for the abundance measurements.

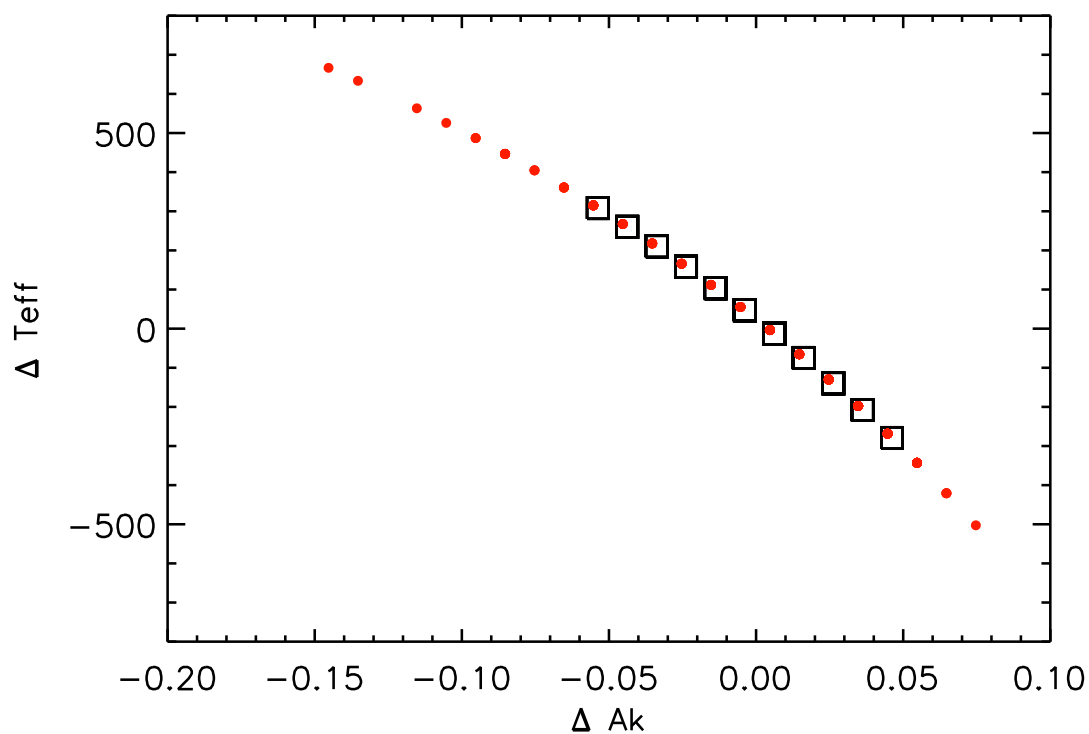


Figure 5.11: The effect of differential reddening towards the Bulge for the determination of photometric effective temperatures. We plot the variations in the A_{K_s} values for a set of 200 random positions in a 30' region towards $b = -4^\circ$ (black squares) and $b = -2^\circ$ (red circles), as obtained from the BEAM calculator, and compare them to variations in the photometric effective temperature.

While the dependence of metallicity error on temperature is not necessarily linear, and will depend on the spectral type of the target, for a reference we recall that already an error of 200 K in effective temperature led to a measurement error in [Fe/H] of 0.1 dex for K giant stars in the Bulge (Zoccali et al. 2008).

5.3.3 Bulge luminosity function and distances

With the de-reddened photometry of VVV obtained as explained in the previous section, we are able to use the RC magnitude as a distance indicator (Paczynski & Stanek 1998; Alves et al. 2002; Grocholski & Sarajedini 2002). We divided each VVV field in four subfields of $\sim 0.4^\circ \times 0.4^\circ$ in which we built the luminosity function (LF) and used it to obtain the mean observed magnitude of the RC, $K_{s_0}^{RC}$, by means of a Gaussian fitting procedure (e.g. Stanek & Garnavich 1998; Babusiaux & Gilmore 2005) following the function:

$$N(K_{s_0}) = a + bK_{s_0} + cK_{s_0}^2 + \frac{N_{RC}}{\sigma_{RC} \sqrt{2\pi}} \exp\left[-\frac{(K_{s_0}^{RC} - K_{s_0})^2}{2\sigma_{RC}^2}\right] \quad (5.7)$$

We first applied a color cut at $(J - K_s) > 0.5$ to minimize the contamination from foreground stars and then fitted the underlying RGB LF using a second order polynomial corresponding to the first 3 terms of Eq. (2). The RC was then fitted with two Gaussians, in the form of the forth term in Eq. (2), in the regions where the two red clumps are observed, i.e for latitudes $b < -5^\circ$ (McWilliam & Zoccali 2010) and with a single Gaussian in the inner regions. An additional Gaussian fit was performed when the red giant branch bump (RGBb) was detected. Upper panels of Fig.5.12 show the final de-reddened CMDs for Baade's Window and the field at $b = -6^\circ$ where the density contours show clearly the single and double RC features in each field. The lower panels of Fig. 5.12 show the de-reddened K_{s_0} band luminosity functions for both fields with overplotted polynomial + Gaussian fits. The polynomial function fits very well the underlying red giant branch population, while Gaussian functions are required to fit RCs and RGBb. A single RC is observed at $K_{s_0} \sim 12.9$ in $b = -4^\circ$, while at $b = -6^\circ$ the RC region shows two components at $K_{s_0} \sim 13.2$ and $K_{s_0} \sim 12.6$. Additionally, the RGBb is observed at $K_{s_0} \sim 13.6$ in $b = -4^\circ$. The latter is in agreement with the measurements of the bulge RGBb by Nataf et al. (2011) using OGLE photometry.

McWilliam & Zoccali (2010) and Nataf et al. (2010) showed for the first time the presence of a double RC observed at large latitudes. McWilliam & Zoccali (2010) argued that this feature could be consequence of a X-shaped Bulge. Furthermore, Saito et al. (2011) mapped the density of RC stars across the bulge using 2MASS photometry and concluded that the X-shape morphology merges to the bar in the inner regions. Our results are in agreement with the measurements in previous studies, showing the clear double peak in the LF of the bulge as can be seen in Fig.5.12. Our method can be then used to map the innermost Bulge regions which are not considered in the work of Saito et al. (2011) because of the limiting depth and blending in 2MASS photometry in these inner regions. This analysis is the subject of the next chapter.

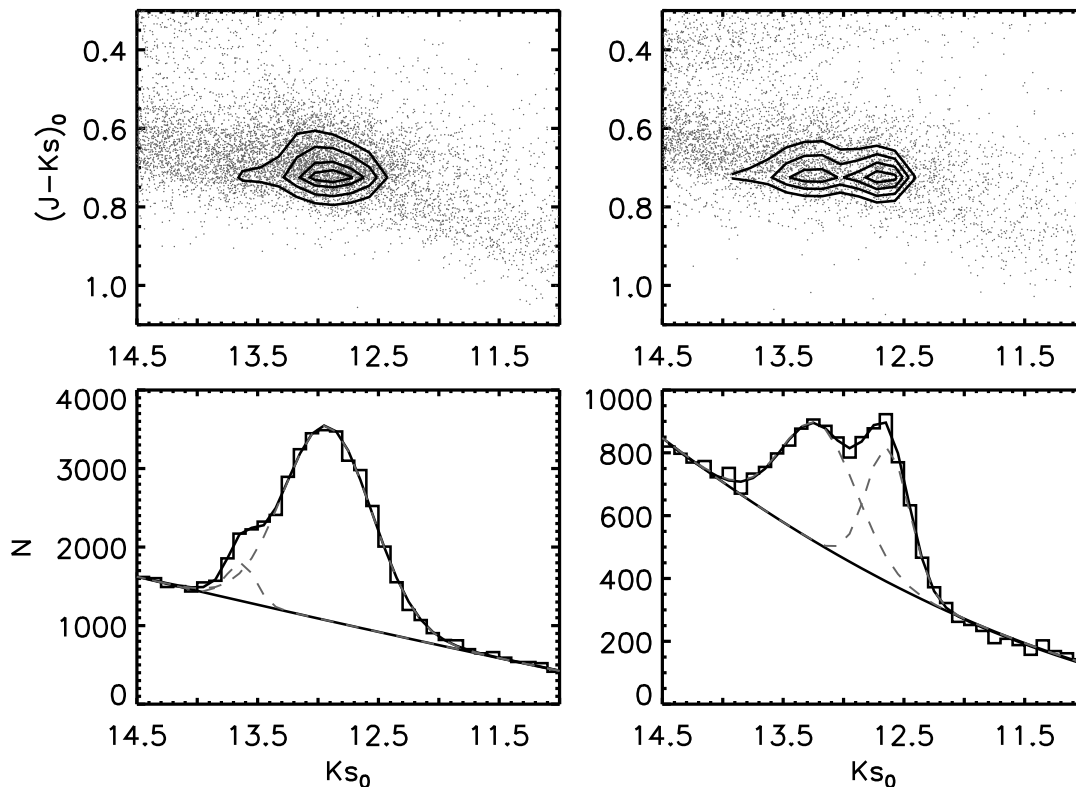


Figure 5.12: Lower panels show the luminosity functions for a subfield in Baade’s Window and at $b = -6$. The underlying RGB is fitted with a second order polynomial and the red clump is fitted with two Gaussians centered at $K_{s0} = 12.9$ and $K_{s0} = 13.2$ for $b = -6$ (right panels) and with a single Gaussian centered at $K_{s0} = 12.9$ for Baade’s Window (left panels). Upper panels show the corresponding CMD for each field, oriented with color along the y-axis and magnitude along the x-axis. Density contours denote the single and double RC in each field. The second gaussian component in BW field is due to the RGB bump.

5.4 Conclusions

We have used the VVV data to obtain a high-resolution extinction map of the galactic Bulge covering ~ 315 sq. deg area: $-10.3^\circ < b < +5.1^\circ$ and $-10.0^\circ < l < +10.4^\circ$. We used the color of RC stars to trace the effect of extinction in subfields of $2' \times 2'$ for $+5^\circ > b > -3.5^\circ$, $4' \times 4'$ for $-3.5^\circ > b > -7^\circ$ and $6' \times 6'$ for $-7^\circ > b > -10^\circ$, providing a first reddening map sensitive to the small scale variations and covering homogeneously the whole Bulge.

An excellent agreement is found when comparing the common regions of our full VVV map with those of DENIS (Schultheis et al. 1999) and Spitzer maps (Schultheis et al. 2009) which cover the very inner regions of the Bulge ($|b| < 2^\circ$). We also have compared our maps with those of Schlegel et al. (1998) at different latitudes and we confirm that Schlegel maps should not be

used for latitudes $|b| < 5^\circ$ towards the Milky Way bulge.

The reddening map presented here becomes particularly important when the global picture of the Bulge is investigated. We presented some of the direct consequences of using a higher resolution map, when studying both the stellar populations and the structure of the Bulge. We show that a typical 30' region at $b = -4^\circ$, for which normally a single extinction value is assumed, has a variation of up to 0.10 magnitudes only due to differential reddening. This effect becomes even more important in the inner regions where differential reddening produces variations of more than 0.35 magnitudes in a similar field size. This has a strong impact in stellar population properties obtained from the color of stars, such as the photometric effective temperature. We show that errors of more than 500 K can be caused by differential extinction in a 30' region if single extinction value is adopted. The current map allows to avoid such errors. Also, we show that the observed CMD of an inner bulge region at $(l, b) = (1.0, -1.0)$ matches very well a CMD produced from the Besançon stellar population model where effects of extinction are obviously not present.

We have also shown how a good treatment of extinction and the dataset such as the one presented here, provides the ideal tool for the inner Galactic structure study based on the luminosity function properties. We find excellent agreement with previous findings of a double red clump for latitudes larger than $b < -5^\circ$ which trace the X-shape of the Galactic bulge (McWilliam & Zoccali 2010; Nataf et al. 2010). We further detect the additional bump in the luminosity function interpreted as the RGBb by Nataf et al. (2011). In the next chapter we use the technique shown here to further investigate the structure of the Galactic bulge.

Our extinction map is available to the community via a web based tool BEAM (Bulge Extinction And Metallicity) calculator (<http://mill.astro.puc.cl/BEAM/calculator.php>). The complete photometric metallicity map (Chapter 7) will also be available from the same site. These maps are an important step towards the understanding of the general properties of the Galactic bulge and they are a particularly valuable tool for the forthcoming spectroscopic surveys of the inner Galaxy.

Chapter 6

The Bulge structure

The presence of bars in spiral galaxies is common (Eskridge et al. 2000) and the Milky Way is no exception. Different studies based on various techniques have suggested that there is a large-scale bar with ~ 2.5 kpc in radius oriented 15-30 degrees with respect to the Galactic center line of sight (e.g. Dwek et al. 1995; Stanek et al. 1997; Bissantz & Gerhard 2002; Babusiaux & Gilmore 2005; Cabrera-Lavers et al. 2007; Rattenbury et al. 2007) with the near end towards positive longitudes.

However, observations of external galaxies have led to the conclusion that the existence of double bars is not unusual (e.g. Laine et al. 2002; Erwin 2011) and have provided observational constraints on their scales. Secondary bars are found to be generally small, with a typical size of ~ 500 pc or a relative length of about 12% of that of the main bar (Erwin 2011). Some observations in the very inner regions of the Milky Way have suggested that there is another structure inside the Galactic bar, namely a nuclear bar (e.g. Alard 2001; Nishiyama et al. 2005). Alard (2001) used 2MASS star counts to show evidence of an excess in the inner regions of the Milky Way, which is interpreted as the presence of a small, lopsided, nuclear bar. In particular, Nishiyama et al. (2005, hereafter N05) used the magnitude of red clump (RC) stars at a latitude of $b = +1^\circ$ to measure the properties of the inner regions ($-10^\circ < l < 10^\circ$) detecting a shallower inclination angle for the Galactic bar at fields with longitudes $|l| < 4^\circ$. This was interpreted by N05 as the effect of a distinct inner bar structure. The existence of such a nuclear bar has strong effects on the gas distribution in the inner parts of the Galaxy. Rodriguez-Fernandez & Combes (2008) concluded that indeed a nuclear bar is likely to be responsible for the observed so-called central molecular zone in the inner Milky Way bulge.

Here, we make use of the ESO public survey Vista Variables in the Via Lactea (VVV) to trace the magnitudes of RC giants in the longitude range $-10^\circ < l < 10^\circ$ at $b = \pm 1^\circ$ to constrain the morphology of the Galactic bar. The technique, based on using RC giants as accurate distance indicators across different lines of sight, was first applied by Stanek et al. (1997) and adopted later by several authors to trace the bar morphology at different Galactic latitudes (e.g. Babusiaux & Gilmore 2005; Rattenbury et al. 2007; Cabrera-Lavers et al. 2007). Minniti et al. (2011) applied this technique to the VVV survey data to detect the edge of the Galactic stellar disk. Here, we use it to test whether the change of the slope in the orientation of the Galactic bar observed by N05 at $b = +1^\circ$ is also evident in VVV data at $b = +1^\circ$, as well as at $b = -1^\circ$. We corroborate

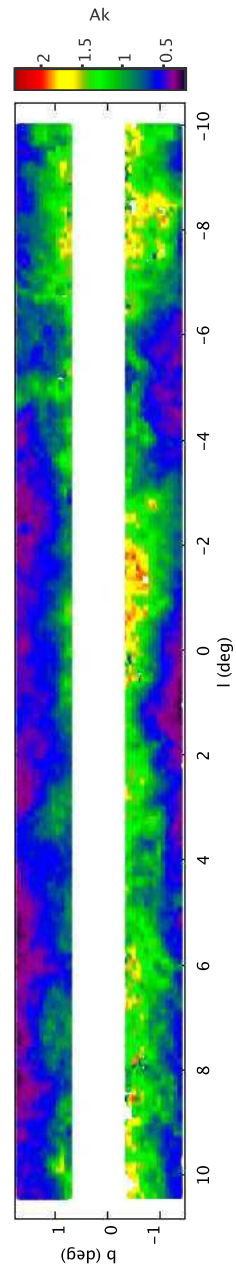


Figure 6.1: K-band extinction map in Galactic coordinates showing the fields analyzed in this study. The 28 VVV tiles cover ranges of longitude $-10^\circ < l < 10^\circ$ and of latitude $-1.4^\circ < b < -0.4^\circ$ and $0.7^\circ < b < 1.7^\circ$.

the measurements of N05, which suggests that there is a distinct structure in the inner regions of the Galactic bar that appears to be symmetric with respect to the Galactic plane. At the end, we also investigate the bar slope changes at higher Galactic latitudes and compare it with the model predictions from Gerhard & Martinez-Valpuesta (2012).

6.1 The data

For this study, we use the near-IR JK photometry from the VVV public survey¹. A detailed description of the survey and the data can be found in Minniti et al. (2010). In particular, the photometric calibration and dereddened magnitudes were calculated as described in Chapter 4 and 5 (Gonzalez et al. 2011c). Multi-band catalogs were produced by a cross-match of sources between single-band catalogs produced at the Cambridge Astronomical Survey Unit (CASU) using the STILTS code (Taylor 2006). For this work, we analyzed a total of 28 tiles, containing about 30 million measured sources, which cover the survey region between $-1.4^\circ < b < -0.4^\circ$ and $+0.7^\circ < b < +1.7^\circ$ at longitudes across the range $-10^\circ < l < 10^\circ$ (Fig.6.1). The photometric calibration was obtained by cross-matching sources of VVV with those of 2MASS flagged with high quality photometry. This produced the final VVV J , H , and K_s photometric catalogs fully consistent with the 2MASS photometric system. The calibrated VVV tile catalogues were then dereddened and used to build the luminosity functions for each of the tiles.

6.2 Tracing the bar in the inner regions

The extinction correction was done following the prescriptions described in Chapter 5 Gonzalez et al. (2011c) used to construct the complete extinction map of the Bulge. For the present analysis, we adopted the Nishiyama et al. (2009) extinction law, where $A_k = 0.528 \cdot E(J - K_s)$ instead of the standard values of Cardelli et al. (1989), as the latter does not seem to be consistent with observations in the high-reddening regions analyzed here. Therefore, the dereddened K_{s_0} magnitudes were obtained as

$$K_{s_0} = K_s + 0.528[(J - K_s)_0 - (J - K_s)], \quad (6.1)$$

where we use the mean intrinsic RC color for the bulge of $(J - K_s)_0 = 0.68$ as measured in Baade's window (Sect. 4.2). We note that by following this procedure we obtain reddening values in subfields of 2×2 arcmin instead of assigning individual extinction values to each star as in N05. Owing to the broadness of the bulge metallicity distribution (e.g. Zoccali et al. 2008; Bensby et al. 2011), a single intrinsic RC color cannot be adopted for all stars but only to the mean of the observed RC color distribution in small subfields where the effects of differential extinction are minimized. Therefore, our procedure allows us to obtain dereddened K_s magnitudes while keeping the imprints of the original bulge stellar population. Figure 6.1 shows the final extinction map and the field coverage for this study.

¹<http://vvvsurvey.org>

We applied a color cut $(J - K_s)_0 > 0.4$ to select the region of the color-magnitude diagram (CMD) dominated by bulge giants and avoid contamination from disk stars. Using the dereddened K_{s_0} magnitudes of bulge giants, we then built the luminosity function for each tile and followed the method introduced by Stanek et al. (1997) to measure the RC mean magnitudes in order to trace the mean distance of the bulge population. The base of the luminosity function was fitted with a second order polynomial and a Gaussian fit was then applied to measure the RC mean magnitude, as given in Equation 5.7.

The results of the Gaussian fits for each RC are listed in Table 6.1. We also included an additional Gaussian fit for a peak in the luminosity function, distinct from the RC, which is centered at $K_{s_0} \sim 13.7$. N05 mention the detection of this additional peak at a dereddened magnitude $K_0 \sim 13.5$ but they only performed Gaussian fits up to a magnitude where the RC is unaffected by this fainter peak. Nataf et al. (2011) also presented its detection, based on optical OGLE data, and identified it as an anomalous red giant branch bump (RGBb). In Gonzalez et al. (2011c), the peak was observed using the VVV photometry up to $b = -4^\circ$. For larger distances from the plane, the detection of this peak becomes difficult because of the split in the RC (McWilliam & Zoccali 2010). However, we point out that, while the magnitude of the RC becomes brighter toward positive longitudes according to the bar orientation, the K_{s_0} magnitude of this additional peak changes in the opposite direction. This is not expected if this feature corresponds to the RGBb. A possibility could be that it instead corresponds to RC stars from a more distant population. Assuming an intrinsic RC magnitude of $M_K = -1.55$, the observed fainter RC peak would be at ~ 11.2 kpc from the Sun. Further discussion of this point, such as the number counts of the RC with respect to those of the secondary peak cannot be addressed in this work because of the possible incompleteness at the magnitudes where this peak is observed, in particular for regions affected by high reddening and crowding. However, we assume here that the RC mean magnitudes remain reliable as long as the additional peak is included in the fitting procedure, independently of its origin. Figure 6.2 shows the results for the fits to the $K_{s,0}$ distribution of RC stars in representative fields of the regions studied in this work.

Figure 6.3 shows the measured location of the Galactic bar obtained from the dereddened K_{s_0} magnitude of the RC at $b = \pm 1^\circ$, compared with those of N05 for $b = +1^\circ$ and adopting an intrinsic magnitude of the RC of $M_K = -1.55$ (Sect. 4.1). Along every line of sight, the dispersion in distance was obtained from the measured σ corrected by an intrinsic dispersion in the RC of 0.17 mag (Babusiaux & Gilmore 2005) and a photometric error of 0.05 mag. As discussed in Stanek et al. (1994), the observed orientation angle based on our method differs from the real one by an amount that depends on the thickness of the bar, measuring larger angles for a thicker bar. For this reason, we included in Figure 6.3 examples of the observed orientations of a bar with axis ratios of $x/y = 0.15$ (Cabrera-Lavers et al. 2007) for the true angles of 15° , 30° , and 45° following corrections shown in Stanek et al. (1994). Results are in good agreement with previous studies, which are consistent with the bar being located at 7.6 kpc, oriented at 30° , and with its near end towards positive longitudes. However, the position angle of the bar in the inner ~ 1 kpc is more than 20° larger than measured in the outer regions, which implies that there is an inner central structure.

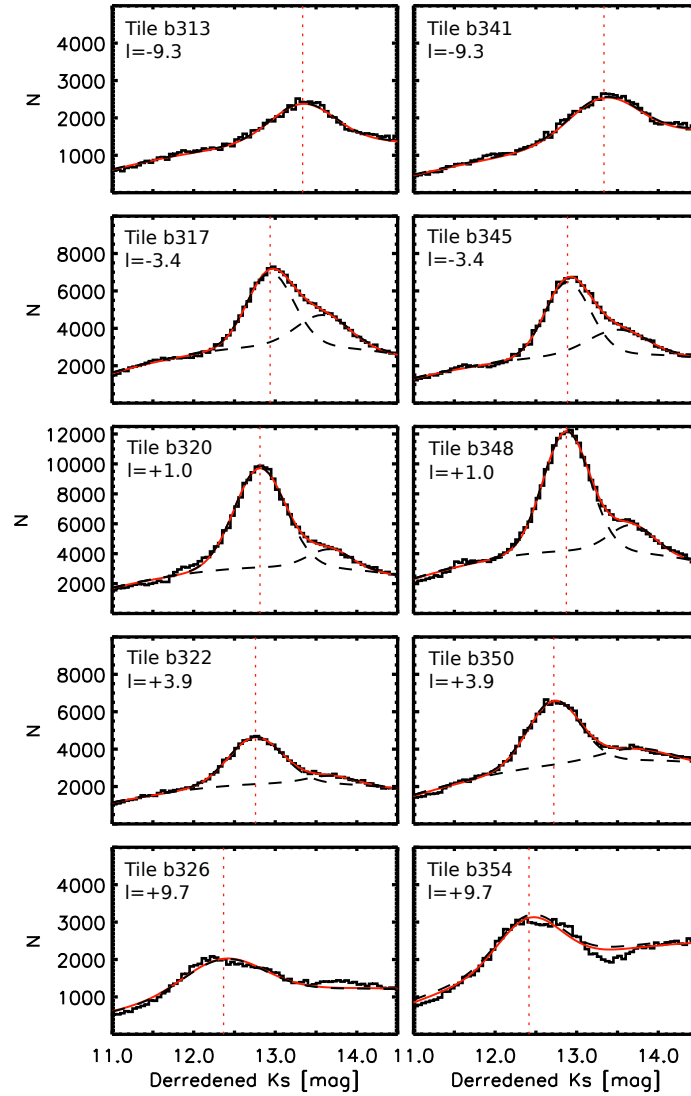


Figure 6.2: $K_{s,0}$ luminosity functions for representative fields at $b = -1^\circ$ (left panels) and $b = +1^\circ$ (right panels). The red solid line shows the best fit to each distribution while the dashed line shows the individual Gaussian fits to the RC and to the additional peak when detected.

Table 6.1: Listed are the mean dereddened (K_{s_0}), sigma (σ) and peak of the Gaussian used to fit the RC in each one of the tiles. $K_{s_{0,2}}$, peak_2 and σ_2 are the parameters used fo fit the secondary peak.

Tile	l	K_{s_0}	peak	σ	$K_{s_{0,2}}$	peak_2	σ_2
	[deg]	[mag]		[mag]	[mag]		[mag]
<i>b = -1</i>							
b313	-9.3	13.36	1004.40	0.39	*	*	*
b314	-7.8	13.29	1219.88	0.42	*	*	*
b315	-6.3	13.25	2451.44	0.44	*	*	*
b316	-4.9	12.99	2569.64	0.30	13.53	1638.15	0.36
b317	-3.4	12.94	3944.79	0.28	13.59	1683.01	0.32
b318	-2.0	12.93	3894.66	0.29	13.68	930.18	0.22
b319	0.5	12.87	5241.86	0.30	13.69	821.97	0.21
b320	1.0	12.81	6658.11	0.31	13.68	1262.40	0.26
b321	2.4	12.80	4209.59	0.30	13.59	756.11	0.27
b322	3.9	12.76	2531.18	0.33	13.70	421.59	0.29
b323	5.3	12.69	1562.18	0.39	13.76	280.90	0.23
b324	6.8	12.57	978.848	0.39	*	*	*
b325	8.3	12.42	793.638	0.40	*	*	*
b326	9.7	12.37	980.697	0.48	*	*	*
<i>b = +1</i>							
b341	-9.3	13.33	1142.66	0.43	*	*	*
b342	-7.8	13.23	1605.09	0.46	*	*	*
b343	-6.3	13.16	2013.17	0.49	*	*	*
b344	-4.9	13.10	2659.84	0.44	*	*	*
b345	-3.4	12.89	3930.44	0.28	13.51	1293.89	0.36
b346	-2.0	12.92	7113.72	0.28	13.68	1817.71	0.29
b347	-0.5	12.89	8410.80	0.27	13.66	1923.11	0.26
b348	1.0	12.87	8029.82	0.29	13.68	1829.86	0.27
b349	2.4	12.80	5536.06	0.30	13.66	1199.78	0.30
b350	3.9	12.72	3473.53	0.32	13.74	642.58	0.40
b351	5.3	12.71	3069.82	0.32	*	*	*
b352	6.8	12.63	2062.99	0.36	*	*	*
b353	8.3	12.53	1643.23	0.37	*	*	*
b354	9.7	12.42	1321.51	0.39	*	*	*

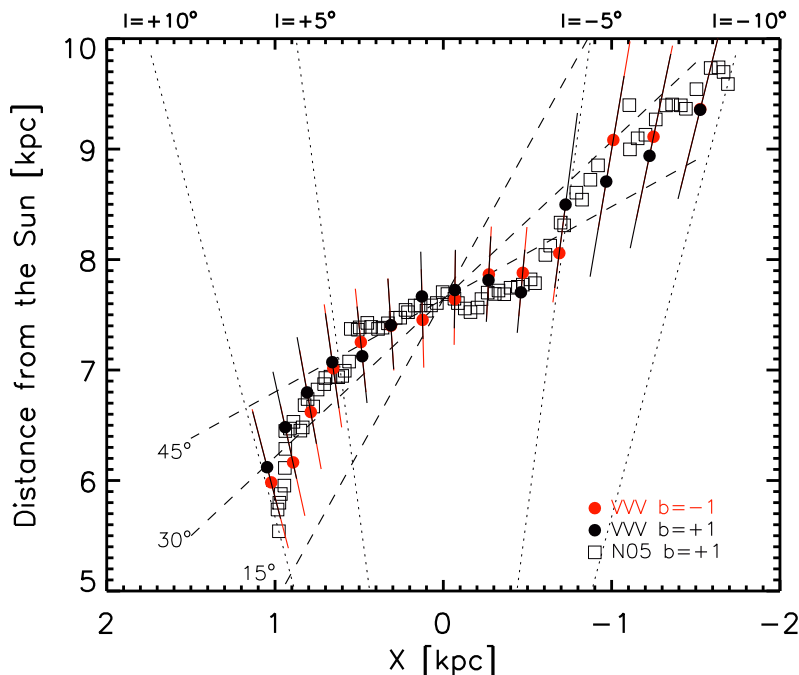


Figure 6.3: Position of the Galactic bar with respect to the Sun as measured with the RC method assuming a mean RC magnitude of $M_K = -1.55$. Red and black filled circles show the results for VVV data at latitudes $b = -1^\circ$ and $b = +1^\circ$, respectively. Solid lines show the distance spread along each line of sight correcting for an intrinsic bulge dispersion of 0.17 mag and photometric errors. Black open squares are the results from N05 at $b = +1$. Dashed lines represent the observed orientation angles for true orientations of 15° , 30° , and 45° following Stanek et al. (1994). Dotted lines show the lines of sight for longitudes $l = \pm 5$ and $l \pm 10$.

6.3 Is there a secondary inner bar in the Milky Way?

Recent studies seem to point out that secondary bars in barred spirals are a common phenomenon, with at least 29% of barred galaxies having a secondary bar (e.g. Laine et al. 2002). Therefore, it would not be surprising that our Milky Way hosts such an inner structure. In this work, we have presented further evidence of the detection of an inner structure in the Galactic bar, as previously suggested by N05, identified by a change in the orientation angle of the bar measured at both positive ($b = +1$) and negative ($b = -1^\circ$) latitudes. Since our results have been obtained independently and based on a different dataset from that of N05, we confirm that the detection is not an artifact owing to possible issues with either the photometry or calibrations.

However, we note that both studies are based on the use of the observed magnitude of the RC to trace distances across different regions of the bar. Therefore, one point to consider is the dependence of metallicity for the intrinsic magnitude of the RC (Girardi & Salaris 2001). As discussed in Sect. 4.2, this dependence can produce changes of ~ 0.1 mag for 0.2 dex changes

in [Fe/H]. However, these gradients in [Fe/H] have only been observed along the minor axis in the outer bulge (Zoccali et al. 2008) and are even more likely to be absent from the inner regions around $b \sim -1^\circ$ (Rich et al. 2007). Even if gradients are indeed present also along the major axis for the inner regions considered here, to produce a similar effect to what we see in Fig. 6.3, the [Fe/H] gradient could not be *radial*, but should go from one extreme of the bar to the other with a slope that changes in the inner longitudes $|l| < 4^\circ$. These particular properties for the stellar populations of the Milky Way bar are very unlikely and in the next Chapter, our photometric metallicity map shows that this is indeed not the case for the Bulge.

A second point to consider is the adopted extinction law for the determination of dereddened K_{s_0} magnitudes. For a consistent comparison with N05 measurements, we have used the same extinction law based on Nishiyama et al. (2009). However, we note that this extinction law, which differs from the more commonly adopted laws (e.g. Cardelli et al. 1989; Savage & Mathis 1979; Rieke & Lebofsky 1985), was derived for the highly reddened inner bulge fields ($|b| < 2^\circ$), while this does not seem to be the case for the whole bulge. In the study of RR Lyrae in the bulge from Kunder et al. (2008), variations with respect to the standard reddening law were observed in a few directions. However, they conclude that, on average, the extinction law of $R_V \sim 3.1$ is consistent with the observations of the bulge at larger distances from the Galactic plane. Given this uncertainty in the correct extinction law with line of sight, a variation of it from standard values to that of Nishiyama et al. (2009) could produce a change of up to 0.1 magnitudes in K_{s_0} for the regions with the highest reddening ($A_k \sim 2.5$), as seen in Fig. 6.1. However, these variations are likely to be randomly distributed along different lines of sight. That the same change in the bar orientation is now observed at both positive and negative latitudes, where reddening patterns differ greatly (Fig. 6.1), leads us to conclude that our results are not an effect of extinction.

At larger Galactic latitudes ($|b| > 3^\circ$), the flattening of the bar within $|l| < 4^\circ$ is not observed. This, combined with the symmetric change in slope, leads us to suggest that we are detecting an inner second bar in the Milky Way. We cannot however exclude that the observed flattening is due to a particular change in the density distribution of RC stars in the inner bulge. Indeed, Gerhard & Martinez-Valpuesta (2012) used the galactic model from Martinez-Valpuesta et al. (2006) to investigate the simulated RC distance modulus towards the same regions investigated here. The model of Martinez-Valpuesta et al. (2006) consists on a central boxy-bulge formed through the buckling instability of a bar embedded in an exponential disk. This model does not have a secondary inner bar component, however, the simulated luminosity functions and RC maxima reproduce our observations very well. Their results suggest that the flattening of the bar orientation observed here is the result of a transition from highly elongated bar to a nearly axisymmetric central concentration of stars and not necessarily to the presence of a secondary inner bar.

6.4 The bar at higher latitudes

In the previous section we studied the bar orientation in the inner regions ($b = \pm 1^\circ$) by measuring the mean RC magnitudes as a function of longitude. Using the homogeneous extinction map

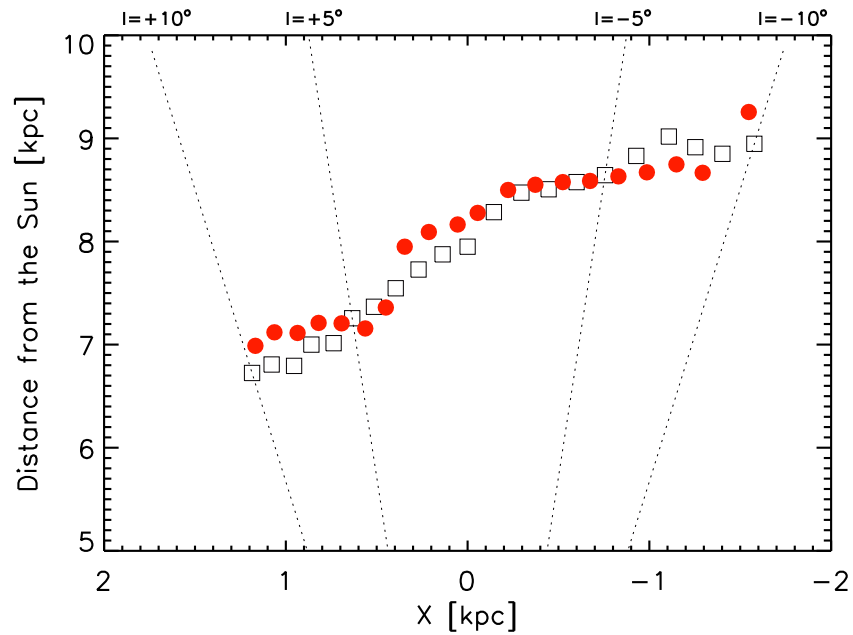


Figure 6.4: Position of the Galactic bar with respect to the Sun as measured with the RC method from the dereddened K_s magnitudes using our extinction map (red filled circles) at a latitude of $b = -5^\circ$. Also shown, are the measurements from the Galactic model as presented in Gerhard & Martinez-Valpuesta (2012) at the same latitude, corresponding to a bar with an angle of 25° with respect to the Sun-Galactic center line of sight (black empty squares). Dotted lines mark the lines of sight for longitudes $l = \pm 5^\circ$ and $l = \pm 10^\circ$

presented in Chapter 5, the study can now be extended to other regions of the Bulge. Ideally, these measurements should be compared to a galactic model such as the one of Martinez-Valpuesta et al. (2006). Interestingly, although this model has not been fine-tuned in any way to reproduce the Milky way properties, in Gerhard & Martinez-Valpuesta (2012) the model was shown to nicely reproduce the observed structural properties of the Bulge, including the change in the bar inclination in the inner regions, as obtained by Nishiyama et al. (2005) and us from VVV data in the previous section. This model also provides predictions for higher latitudes which can now be validated using our extinction-free magnitudes. Figure 6.4 shows position of the bar with respect to the Sun as measured from the mean dereddened K_s VVV magnitudes and from the model of Gerhard & Martinez-Valpuesta (2012) at higher Galactic latitude $b = -5^\circ$. The agreement between our observations and the model is remarkable, confirming that the Milky Way bar is inclined at 25 deg with respect to the Sun-Galactic center line of sight. The correction for differential extinction from our new map allows to extend this comparison of the model and observations to the complete Bulge, including the characterization of the stellar density profile, the observed X-shape, and other structural indicators.

6.5 Conclusions

With our full extinction map it is possible to recover the global Bulge structural information. We have used the VVV data at $b = \pm 1^\circ$ and $b = -5^\circ$ to build the bulge luminosity functions along different lines of sight, and to measure the mean dereddened K_{s_0} magnitude, which can be used as a distance indicator. The RC is clearly detected in all fields, and within $|l| < 5^\circ$ a second component is detected in the K-band luminosity function. Given that the average magnitude shift of this second peak does not follow the primary RC, it could be an independent structure detected at ~ 11.2 kpc from the Sun e.g. a spiral arm behind the bulge.

At $b = \pm 1^\circ$, the main RC traces the mean orientation for the Galactic bar, which produces a magnitude variation from $K_{s_0} \sim 13.4$ (~ 9.6 kpc) at $l = -10$ to $K_{s_0} \sim 12.4$ (~ 6.2 kpc) at $l = +10^\circ$. However, a different position angle is observed for the central ~ 1 kpc regions with longitudes $-4^\circ < l < 4^\circ$. This is in excellent agreement with the results of N05, which show the same change in the orientation of the bar at positive latitudes $b = +1^\circ$. These results suggest an evidence of a possible secondary inner bar with a semi-major axis of ~ 500 pc, that is symmetric to the Galactic plane and has an orientation angle that differs from the large scale bar. Our measurements are consistent with an angle of the inner bar larger than 45° , although in these regions we measure the superposition of both the inner and the large scale bar and therefore detailed models are required to constrain the geometry and structure in the inner bulge. Gerhard & Martinez-Valpuesta (2012) have shown how the Galactic model of Martinez-Valpuesta et al. (2006) reproduces our observations in the inner Bulge ($b = \pm 1^\circ$). This offers an alternative interpretation for the inner flattening of the bar due to changes in the density distribution of stars forming the bar. Their orbits in the innermost regions create a higher concentration, leading to an axisymmetric structure which is not necessarily a second inner bar.

Furthermore, we show that the model of Martinez-Valpuesta et al. (2006) also reproduces our observations at larger latitudes ($b = -5^\circ$). We find a remarkable agreement between our

measurements and those from the model of Martinez-Valpuesta et al. (2006) for a bar at 25° with respect to the Sun-Galactic center line of sight. This study will be extended to the complete 300 deg^2 bulge region and will provide a consistent trace of the structure of the bulge including the inner regions.

Chapter 7

Towards the complete picture of the Milky Way bulge metallicity gradients

7.1 Bulge photometric metallicity distributions

The final goal of our work is to use the information obtained in the previous chapters such as reddening and mean distance to study stellar population metallicity gradients in the bulge. We compare the derived field CMDs with an empirical grid of RGB ridge lines of globular clusters in the $[M_{K_s}, (J - K_s)_0]$ absolute plane. The empirical templates of Galactic halo and bulge globular clusters (M92, M55, NGC 6752, NGC 362, M 69, NGC 6440, NGC 6528 and NGC 6791), with well known metallicity, is selected from the sample of Valenti et al. (2004). We then derive a metallicity value for each field RGB star from its $(J - K_s)_0$ color interpolating within the empirical grid. This procedure has been proven to be effective in bulge globular clusters (Valenti et al. 2007), field (Zoccali et al. 2003; Johnson et al. 2011) as well as in studies of more distant galaxies (e.g. Rejkuba et al. 2005; Lianou et al. 2011).

To transform the observed field CMDs into the absolute plane we use the distance and reddening values derived in the previous sections, while for the cluster ridge lines we adopt the estimates listed in Table 3 of Valenti et al. (2004). It is worth to mention that the cluster templates are derived from a homogeneous photometric database calibrated onto the 2MASS photometric system (see Valenti et al. 2004, for more details) and they have been selected in order to span a large metallicity range, between -2.16 and +0.35. In particular, we have included in our empirical grid the RGB ridge line of NGC6791 which is one of the oldest (age 6-12Gyr, Carney et al. 2005, and references therein) and most metal-rich ($[Fe/H]=0.35$, (Origlia et al. 2006, and references therein) open clusters. Furthermore, we notice that the alpha-abundance patterns of the selected templates - enhanced for metallicity up to that of NGC6528 and solar for higher metallicities - match very well the abundance patterns observed in the Bulge fields (Gonzalez et al. 2011b; Alves-Brito et al. 2010; Lecqueur et al. 2007; Fulbright et al. 2007). This implies that there is no need to adjust the fiducial ridge line of the clusters to match the alpha-abundances of the fields. In the interpolation, stars brighter than $M_{K_s} = -4.5$ were used to include only the RGB region most sensitive to metallicity variations, and to avoid the use of red clump stars (See Zoccali et al.

2003, for a detailed discussion). Additionally, a color cut was applied including only stars with $(J - K_s)_0 > 0.6$ to minimize the disk contamination.

Although this method has been shown to work well in specific cases (i.e. single stellar population and distant galaxies), here a problem may arise from the assumed distance modulus along different latitudes. First, as discussed in the previous sections, the distance estimates are derived assuming an intrinsic RC magnitude which depends on the metallicity. However, the expected error of 0.10 mag for RC stars due to metallicity gradient has small effect on our photometric metallicity measurements because these are based on RGB morphology which has significantly larger sensitivity to metallicity variations. To show that we compare in the next section our photometrically determined metallicity distributions with iron abundances from high resolution spectroscopy.

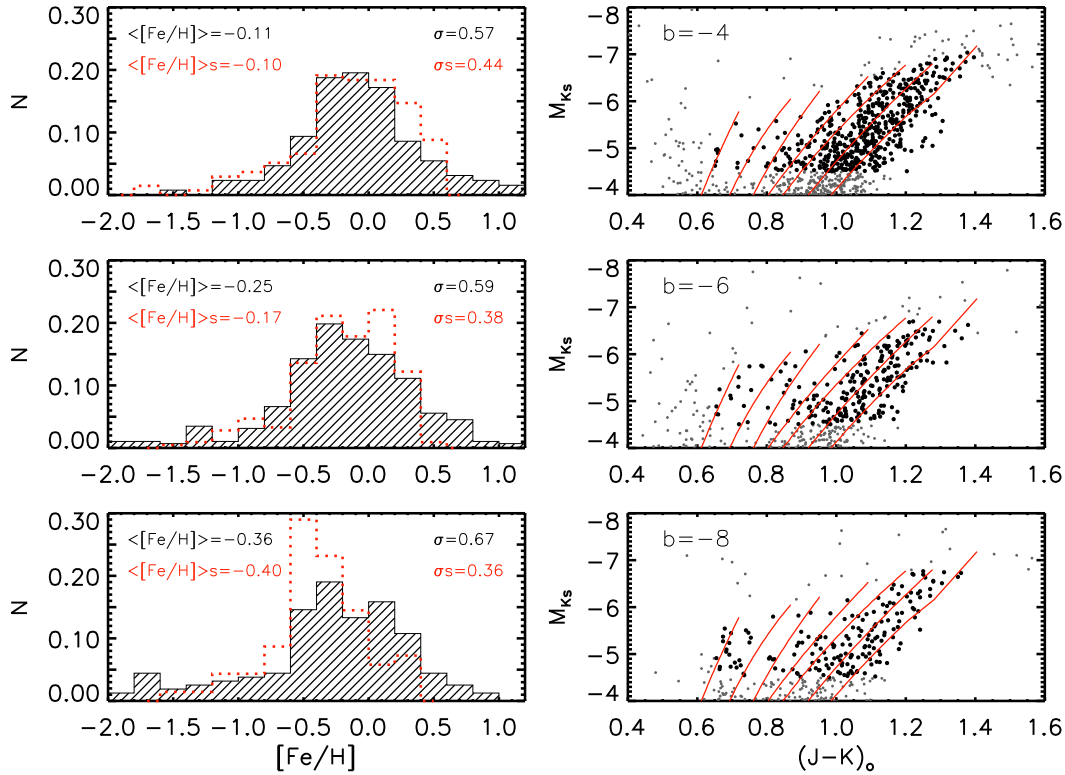


Figure 7.1: *Left panels:* Comparison of the photometric (hashed histogram) and spectroscopic (red dotted histogram) MDFs along the Bulge minor axis at $b = -4^\circ$, -6° and -8° . The average $[Fe/H]$ and dispersion σ_s are also shown for all MDFs. *Right panels:* CMDs in the absolute plane of the fields located along the minor axis at $b = -4^\circ$, -6° and -8° with overplotted the empirical RGB templates. Thick black circles refer to the stars used to derive the photometric MDFs.

A second and more important problem arises from the observed double red clump in the luminosity function, which traces the X shape of the bulge. The choice of the bright or the

faint RC as the observed value to obtain the absolute magnitudes has a strong impact on the results because it implies a change of up to 1.0 mag along the minor axis. Clearly, whichever RC we assume to be the dominating population, RGB stars from the population corresponding the other RC will have an error in magnitude as large as the separation of both clumps. Since it is impossible to distinguish the two populations on the RGB, we adopt the weighted average magnitude of the two RCs as the observed magnitude to calculate the distance modulus for the RGB stars in that field. This magnitude was calculated as:

$$K_{s_0}^{RC} = (K_{s_0}^{RC1} N_{RC1} + K_{s_0}^{RC2} N_{RC2}) / (N_{RC1} + N_{RC2}) \quad (7.1)$$

where N_{RC1} and N_{RC2} are the number of stars in each clump with mean magnitudes $K_{s_0}^{RC1}$ and $K_{s_0}^{RC2}$ respectively.

Therefore, the errors for metallicities for individual stars obtained using our interpolation method are expected to be significantly larger than those based on high resolution spectroscopy. However, the photometric metallicity method provides two unique benefits: (i) the large number statistics, and (ii) most importantly the large coverage, which allows us to investigate gradients.

7.2 Spectroscopic vs. photometric metallicity distributions along the minor axis of the Bulge

The implications of the errors in the photometric metallicity determination method due to assumptions on the reddening law, on the selection of stars on the RC and the assumptions on population corrections for RC absolute magnitude, are hard to take into account within our calculations rigorously and therefore a direct comparison with a more precise method such as high resolution spectroscopy is particularly useful. Several spectroscopic studies have been carried out in fields along the minor axis of the bulge. In particular the metallicity distributions of Zoccali et al. (2008) presented the evidence for metallicity gradient between latitudes -4° , -6° and -12° . The study of Johnson et al. (2011) provided the metallicity distribution of a field at $b = -8^\circ$, which is consistent with the expectation from the metallicities and gradient observed by Zoccali et al. (2008). To check the reliability of our photometric metallicity distribution functions (MDFs), we compare the MDFs from our photometric method in $\sim 30' \times 30'$ fields with those from spectroscopic studies of Zoccali et al. (2008) at $b = -4^\circ$ and $b = -6^\circ$ and of Johnson et al. (2011) at $b = -8^\circ$.

Figure 7.1 shows the remarkable agreement for the photometric (hashed histograms) and spectroscopic (red dotted histograms) MDFs. The metallicity gradient is clearly observed in our data, and the shape of the photometric distributions resemble very well those from spectroscopic studies. The dispersion values in the photometric $[\text{Fe}/\text{H}]$ distributions are larger than the spectroscopic ones. This may be produced by a combination of factors. In particular, our method relies on extrapolation for stars with metallicities larger than 0.35, the value of the most metal-rich template corresponding to the open cluster NGC6791. This could generate a metal rich tail with no reliable abundances, which might increase the dispersion. On the other hand, the metal-poor tail has a possible disk contamination which could end up also increasing the dispersion of our

distributions. However, we do not exclude that such metal-poor stars could actually belong to the bulge. Altogether, we demonstrate that our metallicity determinations are as reliable *in the mean* as the high resolution spectroscopic studies. This presents a powerful tool to trace how metallicity varies not only in discrete fields along the minor axis, but all across the outer bulge.

7.3 The complete metallicity map of the Bulge

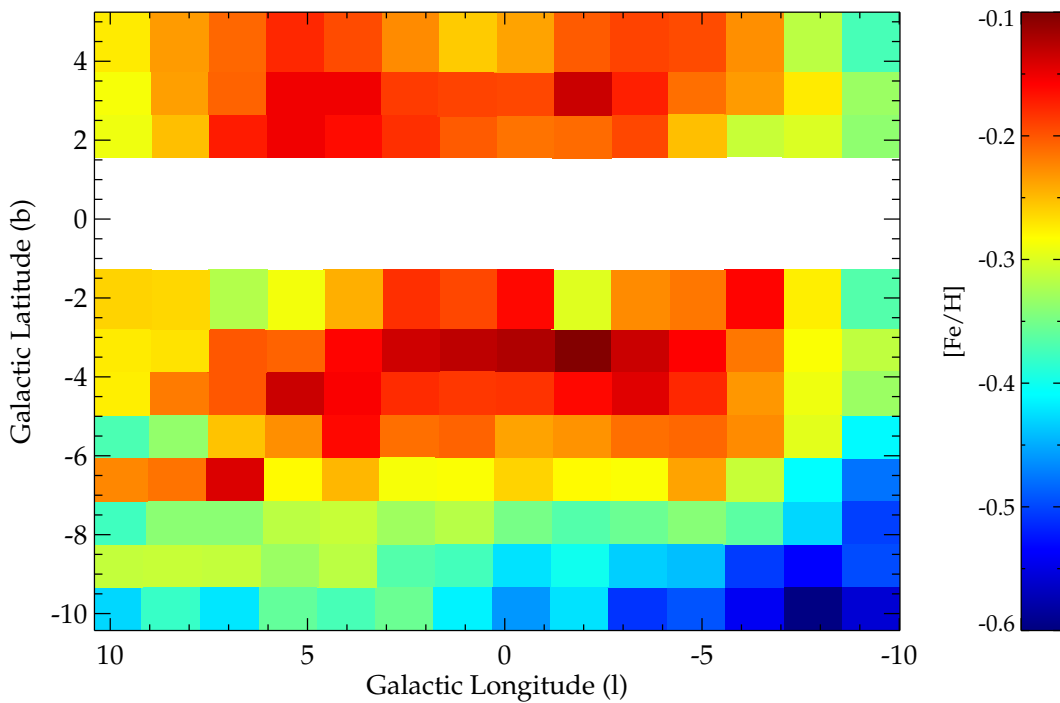


Figure 7.2: Map of the mean values of the metallicity distributions for the complete region of the Bulge covered by the VVV survey.

Having proven the reliability of the mean metallicity measurements from the VVV+2MASS photometry we can now present in Figure 7.2 the first complete map of mean metallicity in bins of $\sim 1.5^\circ \times 1^\circ$. This map is restricted to $|b| > 3^\circ$ as the upper RGB in our dataset corresponds to 2MASS photometry which is limited by crowding in the inner regions. This map provides, for the first time, the general view of metallicity gradients in the Bulge. The gradient along the minor axis, observed from high-resolution studies, is clearly seen in our map and it is the result of a central concentration of metal-rich stars in the region $-5^\circ < b < 5^\circ$ and $-7^\circ < l < 7^\circ$. This concentration of near-solar metallicity stars seems to follow a radial gradient of ~ 0.06 dex/deg, going from more metal-poor stars in the outer Bulge to more metal-rich stars towards the inner regions.

The presence of a radial metallicity gradient is commonly considered to be a strong argument for the classical bulge scenario. In our complete metallicity map we could be observing such gradient. However, we point out that whether boxy-bulges can also show such gradients is still not clear. Furthermore, in Sect. 3 we have shown how the chemodynamical properties of the Bulge are consistent with a change of the dominating population between the outer and inner bulge. A metal-poor, α -rich component with spheroid kinematics which is homogeneous along the minor axis and a metal-rich, α -poor bar population dominating the inner bulge. This is fully consistent with the general view seen in our complete metallicity map.

Another factor which must be considered when interpreting the metallicity map is the observations suggesting a X-shaped bulge structure. McWilliam & Zoccali (2010) presented the observations of a double RC feature (see Sect. 5.3.3) in the luminosity function of the bulge and interpreted it as two concentration of stars at different distances. Later on, Saito et al. (2011) mapped the double clump for the regions $|b| > 4$, using 2MASS photometry, and concluded that it is the result of the a X-shaped Bulge. To explain this, we recall our description of different bulges in chapter 1, in particular that of boxy-bulges. Simulations show how bar suffering from bucking instabilities result in the formation of a peanut or X-shaped structure (Athanasoula 2005; Debattista & Williams 2004; Debattista et al. 2006; Martinez-Valpuesta et al. 2006). When these bars are observed with an orientation exactly perpendicular to the line of sight, they are seen as peanut-bulges. When bars are aligned at an intermediate angle, they appear as boxy-bulges. Observationally, this interpretation has been corroborated by the stellar kinematics, light profiles and morphology of boxy/peanut bulges (Kuijken & Merrifield 1995; Bureau & Freeman 1999; Patsis et al. 2002; Bureau et al. 2006) being in good agreement with the simulations of the formation and buckling of galactic bars.

The Milky Way has a bar oriented $\sim 25^\circ$ with respect to the line of sight (see previous chapter), with the near side towards positive longitudes and shows the corresponding cylindrical rotation (Shen et al. 2010). This scenario fits the picture of its boxy shape being the result of the peanut/X shape bar seen at an intermediate inclination angle. If stars require a longer time to be reach higher orbits above the plane, we could expect to see the older, metal-poor, stars dominating the populations at large latitudes and thus producing the observed metallicity gradient. Furthermore, we see from Fig. 7.2 that stars at larger latitudes are more metal-rich at positive longitudes with respect to negative ones. Following the discussion in (Saito et al. 2011), at a given latitude, stars at negative longitudes are further away from us, because of the X-shaped bar inclination, and therefore their actual vertical distance from the plane will be larger than those stars at the near side of the bar. The observed metallicity map would then be the result of a vertical metallicity gradient along the peanut/X-shaped bulge.

The final observational ingredient, needed to disentangle the origin of the metallicity gradient, will be obtained from radial velocities combined with the metallicities and α -abundances for individual stars. Such a sample will be available from our ongoing FLAMES@VLT ESO large program to obtain a sample of low (LR) and high (HR) resolution spectra of red clump giants mapping the Bulge with 27 fields across both major and minor axis at different Galactic latitudes. LR spectra will provide a screening of accurate radial velocities and metallicities based on CaII Triplet analysis while from HR spectra we will obtain kinematics, metallicities and α -element abundances for ~ 1000 stars along the Bulge major axis.

Chapter 8

Conclusions and outlook

The Bulge is one of the major components of the Galaxy and it can be studied at a unique level of detail, in comparison to those of external galaxies, thanks to its resolved stellar populations which hold the imprints of how our Galaxy formed and evolved. Thus, a better understanding of the Milky Way bulge will provide solid constraints to interpret observations of extragalactic bulges as well as for detailed galaxy formation models. However, to obtain a complete characterization of the Bulge is not straightforward. A large coverage is required in order to study its global properties. Observations in discrete regions less affected by extinction have recently been found not to be representative due to an apparently very complex Bulge nature. A large scale mapping of the Bulge is necessary to make significant progress.

Important constrains for the formation scenario of the Bulge are obtained from the observed alpha-element abundances in the Bulge. In particular the $[\alpha/\text{Fe}]$ ratio is used as indicator of its timescale of formation. We analyzed the α -element abundances for a large number of red giants in the Bulge across different regions as well as for thin and thick disk giants, thus comparing in a homogeneous way distinct Galactic components.

We used the VVV survey data to obtain reddening maps with the highest resolution to date (up to $2'$ in the inner regions), covering the $\sim 320 \text{ deg}^2$ of the Galactic bulge. We showed that we are able to trace small scale variations in extinction with an unprecedented level of detail including the very inner regions. Additionally, we showed that the improved control over extinction allows to accurately trace the Bulge/bar structure and to obtain photometric metallicities.

We used the red clump (RC) giants as a standard candle to build a reddening map and determine distances. This allowed us to construct the color magnitude diagrams in the absolute plane ($M_{K_s}(J - K_s)_0$) and then to obtain individual photometric metallicities for RGB stars in the bulge through interpolation on the RGB ridge lines of cluster sample from Valenti et al. (2004). The final metallicity distributions were compared to those obtained in the spectroscopic studies of Zoccali et al. (2008) and Johnson et al. (2011) showing a remarkable agreement. We demonstrated clearly the possibility to track the observed metallicity gradient along the minor axis and extend the study to the complete region covered by the survey. This provides, within the errors of the method, the opportunity to obtain clues for metallicity gradients along other regions of the bulge.

Our current understanding of the Milky Way bulge can now be summarized as follows:

1. The Milky Way bulge has, at least, two components. The metal-poor component is alpha-enhanced and it is chemically indistinguishable from the thick disk. This hints for a fast and early formation for both the bulge and the thick disk. Such a component shows no variation, neither in abundances nor kinematics, among bulge regions along the minor axis. An additional metal-rich component shows low $[\alpha/\text{Fe}]$, similar to those of the thin disk, and kinematics corresponding to a bar component. This metal-rich component disappears at larger latitudes along the minor axis.
2. The morphology of the Bulge is complex. For latitudes $|b| < 5$ the red clump traces the Galactic bar with an inclination angle of 25° . At lowest galactic latitudes ($b = \pm 1$), we observe a change in the inclination angle, both above and below the plane, for the inner $\pm 4^\circ$ in longitude as traced by the RC. Although this suggests the presence of an inner bar, models of a boxy-bulge, without a nested inner bar, successfully reproduced these results as a consequence of an axisymmetric concentration of RC stars in the inner bulge. At high Galactic latitudes ($|b| > 5$) the double RC observed in the luminosity function is interpreted as two structures at different distances which trace the peanut-X shaped Bulge. This is in agreement with the scenario of the Galactic bulge being a boxy-bulge resulting from the buckling instability of the Galactic bar.
3. The complete metallicity map is consistent with a vertical metallicity gradient ($\sim 0.06\text{dex/deg}$), with metal-rich stars ($[\text{Fe}/\text{H}] \sim 0$) dominating the inner bulge in regions closer to the galactic plane ($|b| < 5$). At larger scale heights, the mean metallicity of the bulge population becomes more metal-poor. This fits in the scenario of older, metal-poor stars dominating at higher scale heights above the plane as stars would require larger time to reach the higher orbits of a boxy-bulge formed from the buckling instability of a, more metal-rich, present day Galactic bar. An additional classical component might be present as suggested from our alpha-element abundance analysis and kinematics.

This work presents an important step forward in our understanding of the general properties of the Milky Way bulge. With our complete high-resolution extinction map, we can now access the previously obscured regions and improve the accuracy of our spectroscopic studies across a larger area. This way we can complement the general photometric metallicity map presented here with the chemical and kinematic information of individual stars. The large scale mapping of the stellar populations and structure of the Galactic bulge, based on the results presented in this thesis, provides a valuable reference for the study of extragalactic bulges. It also allows the current dynamical and chemical evolution models to be tested, for the first time, using global constraints. We may now have the opportunity to finally unfold the formation history and evolution of the Milky Way bulge.

Appendix A

Abundances of 650 bulge red giants

Listed are the metallicities and [Mg/Fe], [Ca/Fe], [Ti/Fe] and [Si/Fe] abundance ratios for 650 K giants in four fields of the Galactic Bulge analysed in Chapter 3. Abundances were measured using standard local thermodynamic equilibrium MARCS models and spectral synthesis using MOOG.

Table A.1: Full table listing Mg, Ca, Ti and Si abundances for stars in the four bulge fields. Metallicities are those presented in Z08 and listed here for reference.

star ID	[Fe/H]	[Mg/Fe]	[Ca/Fe]	[Ti/Fe]	[Si/Fe]	Field
423342	+0.46	-0.04	+0.13	+0.03	-0.08	1
423323	-0.48	+0.43	+0.15	+0.23	+0.26	1
412779	-0.37	+0.23	+0.29	+0.48	+0.22	1
423359	-1.23	+0.34	+0.30	+0.48	+0.43	1
433669	+0.54	-0.02	+0.01	-0.04	-0.10	1
412752	-0.80	+0.15	+0.34	+0.51	+0.30	1
412794	+0.13	-0.04	+0.28	+0.30	-0.08	1
402327	+0.15	+0.08	+0.36	+0.20	-0.17	1
412924	+0.48	-0.04	+0.07	+0.17	-0.13	1
575317	+0.22	+0.14	+0.16	+0.07	+0.03	1
92600	+0.05	+0.20	+0.15	+0.29	+0.08	1
412759	-0.39	+0.24	+0.26	+0.31	+0.16	1
423331	+0.18	-0.02	-0.06	-0.14	-0.02	1
564797	+0.24	+0.02	-0.01	+0.08	-0.11	1
564792	-0.68	+0.28	+0.32	+0.36	+0.30	1
412931	-0.15	+0.25	+0.25	+0.31	+0.11	1
564988	-0.24	+0.32	+0.19	+0.43	+0.14	1
412792	-0.26	+0.29	+0.20	+0.43	+0.18	1
564762	-0.63	+0.35	+0.19	+0.49	+0.36	1
564757	+0.38	+0.04	+0.17	-0.07	-0.08	1
564807	-0.67	+0.34	+0.26	+0.34	+0.32	1

Table A.1: continued.

star ID	[Fe/H]	[Mg/Fe]	[Ca/Fe]	[Ti/Fe]	[Si/Fe]	Field
575293	+0.41	+0.09	+0.34	+0.11	-0.02	1
92537	-0.56	+0.40	+0.37	+0.51	+0.31	1
575303	-0.27	+0.35	-0.03	+0.33	+0.26	1
240260	-0.26	+0.29	+0.27	+0.35	+0.09	1
82762	+0.31	+0.09	+0.30	-0.06	+0.01	1
92565	-0.05	+0.06	+0.06	+0.16	+0.01	1
240210	-0.04	+0.23	+0.31	+0.28	+0.22	1
554722	-0.44	+0.20	+0.12	+0.36	+0.26	1
82725	-0.70	+0.30	+0.16	+0.37	+0.41	1
231262	-0.10	+0.16	+0.07	+0.30	+0.10	1
231099	-0.22	+0.09	+0.16	+0.34	+0.09	1
82747	-0.26	+0.14	+0.27	+0.44	+0.20	1
63856	+0.33	+0.03	+0.01	-0.06	+0.00	1
231144	-0.20	+0.24	+0.22	+0.47	+0.01	1
231364	+0.27	+0.01	+0.10	+0.04	-0.11	1
82742	+0.17	+0.09	+0.03	-0.11	+0.04	1
73506	-0.24	+0.30	+0.10	+0.29	+0.09	1
222451	-0.33	+0.22	+0.08	+0.32	+0.24	1
73504	-0.16	+0.25	+0.20	+0.38	+0.10	1
82761	-0.21	+0.20	+0.32	+0.41	+0.13	1
73490	+0.49	+0.08	+0.04	+0.00	-0.04	1
222618	-0.33	+0.28	+0.31	+0.44	+0.17	1
357480	+0.32	-0.12	+0.08	+0.00	-0.10	1
554664	-0.48	+0.33	+0.29	+0.54	+0.31	1
73514	-0.41	+0.35	+0.29	+0.50	-0.04	1
205243	+0.31	+0.16	+0.28	+0.30	-0.13	1
82705	-0.19	+0.24	+0.32	+0.42	+0.23	1
205257	-1.10	+0.29	+0.00	+0.19	+0.42	1
82831	+0.33	+0.09	+0.22	+0.16	+0.07	1
205436	+0.16	+0.05	+0.10	+0.28	-0.10	1
82798	-0.06	+0.21	+0.26	+0.29	+0.03	1
73515	-0.45	+0.30	+0.38	+0.45	+0.18	1
214035	+0.26	+0.08	+0.20	+0.10	-0.01	1
63794	-0.31	+0.16	+0.39	+0.31	+0.29	1
63792	-0.15	+0.39	+0.25	+0.34	+0.17	1
54167	-0.38	+0.25	+0.14	+0.30	+0.41	1
54104	-0.28	+0.28	+0.00	+0.20	+0.00	1
54132	-0.11	+0.27	+0.11	+0.35	+0.18	1
44560	-0.23	+0.14	+0.16	+0.21	+0.12	1
205356	-0.19	+0.11	+0.01	+0.01	+0.17	1

Table A.1: continued.

star ID	[Fe/H]	[Mg/Fe]	[Ca/Fe]	[Ti/Fe]	[Si/Fe]	Field
63800	+0.31	+0.16	+0.25	+0.12	-0.14	1
63849	-0.92	+0.35	+0.33	+0.48	+0.41	1
537070	-1.03	+0.38	+0.35	+0.49	+0.30	1
63823	-0.04	+0.16	+0.07	+0.23	+0.03	1
545401	+0.01	+0.11	+0.18	+0.14	+0.02	1
545440	-0.60	+0.43	+0.31	+0.30	+0.34	1
54311	+0.26	+0.06	+0.09	+0.22	-0.03	1
537101	-0.67	+0.14	+0.28	+0.23	+0.31	1
554655	-0.34	+0.13	+0.11	+0.24	+0.17	1
392918	+0.05	+0.11	+0.24	+0.32	+0.10	1
63839	-0.22	+0.24	+0.21	+0.25	+0.09	1
554700	-0.17	+0.11	+0.14	+0.31	+0.15	1
554787	-0.58	+0.31	+0.39	+0.36	+0.31	1
63855	+0.40	+0.14	-0.04	-0.04	+0.10	1
402294	-0.50	+0.43	+0.38	+0.53	+0.31	1
63820	-0.14	+0.11	+0.31	+0.27	+0.10	1
393015	-0.06	+0.41	+0.36	+0.35	+0.02	1
554663	-0.72	+0.40	+0.36	+0.33	+0.44	1
63834	+0.16	+0.21	+0.19	+0.25	+0.01	1
402361	-1.05	+0.24	+0.30	+0.40	+0.41	1
402307	+0.40	+0.05	+0.17	+0.10	-0.11	1
402414	-0.21	+0.39	+0.11	+0.49	+0.29	1
545288	+0.13	+0.19	+0.20	+0.15	+0.11	1
554889	-0.10	+0.12	+0.33	+0.30	+0.13	1
402315	-0.17	+0.25	+0.31	+0.41	+0.08	1
554811	+0.17	+0.04	+0.30	+0.05	+0.00	1
234671	+0.06	+0.04	+0.05	+0.05	-0.03	1
402332	-0.31	+0.26	+0.19	+0.41	+0.28	1
402322	-0.94	+0.36	+0.36	+0.35	+0.32	1
564743	+0.21	+0.12	+0.03	+0.06	-0.04	1
402311	+0.08	+0.12	+0.15	+0.26	+0.00	1
244582	-0.81	+0.21	+0.33	+0.30	+0.20	1
244504	-0.25	+0.26	+0.22	+0.35	+0.27	1
402607	-0.82	+0.23	+0.28	+0.40	+0.39	1
402531	-0.85	+0.26	+0.28	+0.51	+0.36	1
402325	-0.32	+0.23	+0.13	+0.36	+0.29	1
585982	-0.08	+0.41	+0.15	+0.28	+0.09	1
575308	+0.27	+0.16	+0.26	+0.27	+0.08	1
575289	-0.50	+0.49	+0.29	+0.45	+0.21	1
423298	-0.08	+0.12	+0.28	+0.24	+0.20	1

Table A.1: continued.

star ID	[Fe/H]	[Mg/Fe]	[Ca/Fe]	[Ti/Fe]	[Si/Fe]	Field
433830	+0.17	+0.25	-0.08	+0.00	-0.04	1
564963	+0.34	+0.19	+0.14	+0.14	-0.05	1
554980	+0.31	+0.03	+0.03	+0.08	-0.18	1
423304	+0.22	+0.02	+0.06	+0.24	-0.09	1
102833	+0.29	+0.11	+0.24	+0.17	-0.15	1
102853	+0.15	+0.14	+0.27	+0.27	+0.00	1
564768	-0.30	+0.06	+0.28	+0.42	+0.28	1
586077	+0.21	+0.07	+0.04	+0.08	-0.16	1
586005	+0.29	+0.00	+0.08	+0.09	-0.18	1
564789	-0.15	+0.03	+0.10	+0.42	+0.04	1
596502	+0.28	+0.19	+0.03	+0.10	+0.10	1
564991	+0.19	+0.05	+0.09	+0.19	+0.00	1
82760	+0.25	-0.06	-0.05	+0.03	-0.20	1
82727	+0.17	+0.05	+0.15	+0.11	-0.16	1
92557	-0.07	+0.18	+0.18	+0.46	-0.05	1
231128	+0.17	-0.03	+0.03	+0.10	-0.08	1
82717	+0.28	+0.15	-0.03	+0.18	-0.18	1
240216	+0.19	+0.11	+0.31	+0.21	+0.04	1
240459	-0.39	+0.31	+0.28	+0.54	+0.41	1
240394	+0.14	+0.16	+0.04	+0.01	-0.08	1
231369	+0.29	+0.07	+0.01	-0.01	-0.16	1
231367	-0.01	+0.11	+0.12	+0.27	+0.01	1
231310	+0.30	+0.11	+0.31	+0.08	-0.10	1
374186	+0.20	+0.05	+0.08	+0.17	+0.04	1
231325	+0.34	-0.11	-0.09	+0.05	+0.00	1
222627	+0.13	+0.13	+0.13	+0.08	+0.03	1
231185	+0.19	-0.04	+0.21	+0.15	-0.10	1
231233	-0.16	+0.26	+0.13	+0.08	+0.12	1
365797	-0.19	+0.34	+0.26	+0.56	+0.17	1
222412	-0.11	+0.20	+0.28	+0.46	+0.17	1
222408	+0.31	+0.25	+0.04	+0.03	+0.00	1
357466	+0.43	+0.07	-0.09	+0.27	+0.01	1
350527	-0.65	+0.37	+0.33	+0.56	+0.30	1
222523	+0.01	+0.24	-0.03	+0.09	+0.30	1
222543	+0.34	-0.12	+0.14	+0.18	-0.04	1
357436	+0.44	-0.10	+0.13	+0.01	-0.09	1
357459	-0.01	+0.06	+0.10	+0.29	+0.04	1
73607	+0.28	+0.07	+0.03	+0.13	-0.01	1
73483	+0.16	+0.01	+0.04	+0.08	+0.02	1
73609	+0.28	+0.03	-0.10	+0.08	-0.09	1

Table A.1: continued.

star ID	[Fe/H]	[Mg/Fe]	[Ca/Fe]	[Ti/Fe]	[Si/Fe]	Field
214192	+0.11	+0.22	+0.18	+0.24	-0.02	1
73472	+0.49	-0.17	+0.01	+0.02	-0.25	1
64005	-0.25	+0.36	+0.17	+0.39	+0.16	1
205265	+0.02	+0.03	+0.16	+0.33	+0.03	1
214042	+0.38	+0.14	+0.08	-0.01	-0.06	1
350483	+0.14	+0.13	+0.09	+0.13	+0.03	1
64018	+0.15	+0.12	+0.08	+0.01	+0.22	1
63859	+0.25	+0.23	+0.11	+0.13	+0.00	1
545445	+0.13	-0.01	+0.02	+0.05	+0.01	1
63840	+0.31	+0.15	+0.22	+0.19	-0.01	1
54108	+0.46	-0.09	-0.02	+0.03	-0.26	1
54125	+0.07	+0.18	+0.19	+0.28	+0.22	1
73467	+0.12	+0.08	+0.01	+0.19	-0.02	1
54078	+0.09	+0.01	+0.26	+0.08	-0.01	1
63829	-0.01	+0.17	+0.06	+0.09	+0.01	1
537095	+0.31	+0.05	+0.17	+0.04	+0.00	1
545222	+0.16	+0.12	+0.12	+0.19	+0.02	1
545438	+0.12	+0.16	+0.05	+0.19	-0.04	1
545233	+0.31	+0.07	+0.09	+0.17	-0.03	1
545313	+0.19	+0.16	-0.08	+0.30	-0.05	1
537092	-0.25	+0.39	+0.33	+0.46	+0.00	1
402415	+0.01	+0.18	+0.00	+0.31	-0.05	1
554670	-0.26	+0.25	+0.18	+0.48	+0.26	1
554748	+0.39	+0.07	+0.01	+0.09	-0.08	1
392952	+0.13	+0.16	+0.12	+0.09	-0.14	1
392896	-0.12	+0.20	+0.06	+0.38	+0.16	1
393083	+0.03	+0.19	+0.02	+0.22	-0.02	1
393053	+0.49	+0.09	+0.04	+0.03	-0.15	1
392931	-0.04	+0.19	+0.03	+0.09	-0.03	1
545269	+0.45	+0.09	+0.04	+0.06	-0.09	1
554683	-0.20	+0.21	+0.31	+0.49	+0.11	1
554668	+0.08	+0.17	+0.04	+0.17	+0.03	1
78106	-0.17	+0.40	+0.19	+0.49	+0.11	1
402498	+0.55	+0.06	+0.05	-0.05	-0.18	1
234704	-0.18	+0.26	+0.21	+0.36	+0.09	1
234701	+0.12	+0.24	+0.27	+0.26	-0.05	1
234888	+0.28	-0.60	+0.03	+0.00	-0.17	1
554713	+0.20	+0.16	+0.09	+0.13	+0.05	1
554956	-0.01	+0.19	+0.30	+0.49	+0.03	1
392951	+0.10	+0.11	+0.04	+0.32	-0.17	1

Table A.1: continued.

star ID	[Fe/H]	[Mg/Fe]	[Ca/Fe]	[Ti/Fe]	[Si/Fe]	Field
412750	+0.11	+0.14	+0.25	+0.29	-0.04	1
411479	-0.30	+0.09	+0.34	+0.39	+0.23	1
402656	-0.32	+0.31	+0.33	+0.54	+0.10	1
554694	+0.15	+0.07	+0.04	+0.31	+0.05	1
402375	+0.05	+0.22	+0.20	+0.25	+0.02	1
244829	-1.09	+0.43	+0.36	+0.50	+0.47	1
244738	-0.25	+0.27	+0.34	+0.48	+0.08	1
402347	+0.19	+0.06	+0.03	+0.39	-0.04	1
564772	-0.07	+0.21	+0.06	+0.33	+0.15	1
423286	+0.05	+0.11	+0.18	+0.29	+0.04	1
267974	+0.31	-0.04	+0.07	+0.18	-0.19	1
412753	+0.33	+0.09	+0.09	+0.21	-0.17	1
256345	+0.33	+0.06	+0.04	+0.02	+0.00	1
41958c3	+0.05	+0.20	+0.11	+0.32	-0.10	2
157820c3	-0.73	+0.40	+0.25	+0.37	+0.27	2
32799c3	-1.25	+0.44	+0.22	+0.29	+0.40	2
76187c3	-0.42	+0.44	+0.26	+0.48	+0.26	2
38354c3	-0.61	+0.33	+0.29	+0.43	+0.22	2
203158c3	-0.04	+0.29	+0.09	+0.38	+0.01	2
39802c3	-0.50	+0.17	+0.22	+0.26	+0.18	2
43054c3	-1.03	+0.32	+0.29	+0.33	+0.44	2
46885c3	+0.00	+0.15	+0.17	+0.04	+0.10	2
1604c2	-1.13	+0.38	+0.39	+0.47	+0.46	2
36989c3	+0.05	+0.23	+0.10	+0.12	+0.09	2
36067c3	+0.08	+0.19	+0.09	+0.15	+0.12	2
77454c2	-0.38	+0.30	+0.20	+0.31	+0.10	2
43562c2	-0.81	+0.37	+0.18	+0.34	+0.40	2
32832c2	-0.03	+0.17	+0.09	+0.19	-0.01	2
62009c2	-0.39	+0.37	+0.21	+0.36	+0.37	2
38565c2	-0.26	+0.27	+0.13	+0.42	+0.08	2
204270c3	+0.02	+0.25	+0.28	+0.20	-0.02	2
69429c3	-0.76	+0.41	+0.24	+0.36	+0.39	2
56671c3	-0.20	+0.24	+0.30	+0.14	+0.11	2
25213c2	+0.09	+0.14	+0.05	+0.03	+0.06	2
35428c2	-1.16	+0.13	+0.24	+0.40	+0.35	2
31338c2	-0.55	+0.28	+0.10	+0.49	+0.20	2
53477c2	-0.55	+0.30	+0.28	+0.40	+0.22	2
56410c2	-1.10	+0.41	+0.26	+0.30	+0.30	2
4799c2	-0.12	+0.26	+0.41	+0.42	+0.26	2
43239c2	-1.26	+0.31	+0.20	+0.46	+0.30	2

Table A.1: continued.

star ID	[Fe/H]	[Mg/Fe]	[Ca/Fe]	[Ti/Fe]	[Si/Fe]	Field
14297c2	-0.66	+0.51	+0.11	+0.41	+0.29	2
17437c2	-0.50	+0.39	+0.29	+0.53	+0.25	2
30173c2	-0.90	+0.21	+0.23	+0.44	+0.38	2
45160c2	-0.56	+0.41	+0.32	+0.47	+0.09	2
13661c2	-0.09	+0.20	+0.14	+0.25	+0.04	2
212324c6	-0.32	+0.35	+0.39	+0.41	+0.10	2
10381c2	-0.14	+0.11	+0.23	+0.25	+0.30	2
14893c2	-0.47	+0.34	+0.05	+0.16	+0.36	2
204828c2	-0.22	+0.27	+0.27	+0.38	+0.11	2
203913c2	-0.24	+0.35	+0.29	+0.30	+0.08	2
33058c2	-0.35	+0.41	+0.26	+0.40	+0.09	2
212175c6	-0.47	+0.38	+0.33	+0.55	+0.26	2
213150c6	-0.02	+0.06	-0.04	+0.16	+0.07	2
1678c2	-0.95	-0.03	+0.22	+0.40	+0.30	2
874c2	-0.32	+0.32	+0.24	+0.42	+0.00	2
7694c2	+0.15	+0.09	+0.06	+0.19	-0.04	2
8312c2	-0.32	+0.17	+0.11	+0.25	+0.22	2
19402c1	-0.61	+0.32	+0.29	+0.38	+0.20	2
23483c1	-0.52	+0.33	+0.38	+0.31	+0.24	2
98692c6	+0.07	+0.17	+0.23	+0.30	-0.03	2
94324c6	-0.39	+0.38	+0.28	+0.51	+0.19	2
99147c5	-0.60	+0.29	+0.13	+0.38	+0.29	2
96158c6	-0.37	+0.35	+0.31	+0.54	+0.16	2
100047c6	-0.33	+0.31	+0.14	+0.43	+0.14	2
102180c6	-0.39	+0.26	+0.15	+0.38	+0.23	2
211484c6	-0.60	+0.31	+0.35	+0.48	+0.24	2
106969c6	-1.00	+0.30	+0.33	+0.52	+0.33	2
91438c6	-0.62	+0.33	+0.37	+0.10	+0.30	2
74262c6	-0.32	+0.29	+0.33	+0.30	+0.22	2
79869c6	-0.48	+0.22	+0.29	+0.50	+0.24	2
98974c6	-0.39	+0.22	+0.24	+0.43	+0.08	2
99069c6	-0.26	+0.14	+0.14	+0.24	+0.08	2
100384c6	-0.57	+0.45	+0.30	+0.40	+0.10	2
108928c6	-0.88	+0.28	+0.36	+0.42	+0.35	2
101274c6	-0.06	+0.14	+0.20	+0.48	+0.00	2
71769c6	-0.22	+0.22	+0.23	+0.23	+0.11	2
62520c6	-0.84	+0.25	+0.25	+0.32	+0.30	2
60577c6	-0.18	+0.30	+0.18	+0.44	-0.05	2
43679c6	-0.59	+0.28	+0.23	+0.44	+0.20	2
54561c6	-0.25	+0.27	+0.29	+0.37	+0.23	2

Table A.1: continued.

star ID	[Fe/H]	[Mg/Fe]	[Ca/Fe]	[Ti/Fe]	[Si/Fe]	Field
80281c6	-0.08	+0.16	+0.24	+0.34	+0.03	2
66376c6	+0.19	+0.28	+0.26	+0.17	+0.04	2
205837c7	-0.36	+0.38	+0.28	+0.54	+0.23	2
75097c7	-0.09	+0.16	+0.06	+0.36	-0.02	2
63747c7	-0.09	+0.23	+0.10	+0.39	+0.15	2
46642c7	+0.21	+0.06	+0.07	+0.14	-0.06	2
57883c7	-0.25	+0.23	+0.33	+0.38	+0.13	2
51688c6	-0.42	+0.37	+0.33	+0.59	+0.19	2
209695c7	-0.11	+0.39	+0.14	+0.49	+0.16	2
90337c7	-0.27	+0.20	+0.33	+0.30	+0.07	2
87232c7	-0.21	+0.29	+0.21	+0.42	+0.09	2
54480c7	-0.40	+0.36	+0.31	+0.40	+0.11	2
64860c7	+0.09	+0.18	+0.08	+0.19	-0.07	2
79003c7	-0.40	+0.20	+0.22	+0.46	+0.17	2
50439c7	-0.08	+0.34	+0.28	+0.46	-0.01	2
80144c7	-0.05	+0.22	+0.10	+0.14	-0.01	2
97618c7	-0.91	+0.21	+0.20	+0.47	+0.41	2
102010c7	-0.56	+0.38	+0.34	+0.56	+0.14	2
87242c8	+0.00	+0.24	+0.26	+0.10	+0.13	2
88768c7	-0.25	+0.27	+0.20	+0.50	+0.15	2
86105c7	-0.14	+0.25	+0.35	+0.51	-0.01	2
77209c7	-0.43	+0.35	+0.33	+0.50	+0.31	2
98458c7	-0.02	+0.26	+0.06	+0.07	+0.30	2
5685c3	-1.15	+0.20	+0.20	+0.50	+0.44	2
5118c4	+0.06	+0.16	+0.05	+0.25	-0.05	2
110465c7	+0.00	+0.20	+0.01	+0.33	+0.02	2
212654c8	+0.39	+0.04	+0.25	+0.02	-0.10	2
108191c7	-0.77	+0.32	+0.35	+0.55	+0.30	2
23017c3	+0.09	+0.15	-0.02	+0.17	+0.01	2
101167c8	+0.05	+0.22	+0.16	+0.30	-0.02	2
202633c3	+0.31	+0.14	+0.01	+0.11	+0.05	2
32080c3	-0.17	+0.28	+0.06	+0.39	+0.06	2
43791c3	+0.00	+0.07	+0.06	+0.18	+0.04	2
11653c3	+0.13	+0.18	+0.38	+0.41	-0.14	2
21259c2	-0.08	+0.29	+0.25	+0.54	-0.10	2
34058c3	+0.21	+0.13	+0.00	+0.09	+0.02	2
40528c3	-0.48	+0.39	+0.08	+0.40	+0.30	2
29280c3	+0.18	+0.08	+0.01	+0.00	+0.00	2
12982c3	+0.01	+0.09	+0.10	+0.35	+0.11	2
108051c7	-0.09	+0.24	+0.15	+0.36	+0.13	2

Table A.1: continued.

star ID	[Fe/H]	[Mg/Fe]	[Ca/Fe]	[Ti/Fe]	[Si/Fe]	Field
20863c2	+0.08	+0.20	+0.12	+0.09	+0.02	2
31220c2	-0.02	+0.20	-0.07	+0.03	+0.20	2
50086c2	+0.32	+0.08	+0.18	+0.11	-0.04	2
208608c3	-0.56	+0.25	+0.16	+0.38	+0.28	2
58159c3	-0.09	+0.15	+0.10	+0.23	+0.06	2
205096c2	-0.15	+0.14	+0.12	+0.07	+0.07	2
42348c2	-0.09	+0.19	+0.09	+0.07	+0.10	2
149531c2	-0.38	+0.20	+0.03	+0.09	+0.24	2
31090c2	-0.26	+0.35	+0.12	+0.39	+0.09	2
69986c2	-0.27	+0.38	+0.19	+0.53	+0.14	2
139560c2	+0.26	+0.05	+0.04	+0.07	-0.08	2
145595c2	+0.44	-0.06	+0.07	+0.09	-0.08	2
22905c2	-0.45	+0.37	+0.19	+0.32	+0.24	2
47298c2	-0.51	+0.48	+0.25	+0.41	+0.27	2
33601c1	+0.29	-0.02	+0.07	+0.03	-0.16	2
43023c2	-0.46	+0.30	+0.32	+0.30	+0.20	2
31176c2	-0.22	+0.29	+0.19	+0.29	+0.06	2
17038c2	+0.29	+0.08	+0.09	-0.13	+0.05	2
959c2	-0.58	+0.37	+0.24	+0.33	+0.25	2
10584c2	-0.38	+0.29	+0.13	+0.35	+0.10	2
15094c1	-0.19	+0.20	+0.23	+0.51	+0.02	2
95371c6	-0.27	+0.29	+0.25	+0.46	+0.01	2
103413c6	+0.24	+0.11	+0.08	-0.16	+0.13	2
85625c5	+0.15	+0.08	+0.09	+0.05	+0.03	2
91631c6	-0.28	+0.32	+0.21	+0.49	+0.26	2
95545c6	-0.45	+0.44	+0.25	+0.42	+0.42	2
96460c6	+0.25	+0.07	+0.21	+0.17	-0.06	2
83500c6	+0.09	+0.12	+0.08	+0.46	-0.06	2
72513c6	-0.48	+0.34	+0.20	+0.39	+0.12	2
69731c6	-0.19	+0.28	+0.19	+0.39	+0.07	2
73072c6	+0.12	+0.27	+0.04	-0.10	+0.14	2
56641c6	+0.17	+0.08	+0.10	-0.04	+0.04	2
208907c6	-0.17	+0.30	+0.16	+0.25	+0.08	2
99166c6	+0.04	+0.24	+0.29	+0.26	+0.16	2
71832c6	-0.09	+0.20	+0.14	+0.19	+0.18	2
77481c6	-0.28	+0.33	+0.19	+0.46	+0.19	2
91776c6	+0.23	+0.11	+0.14	+0.15	-0.09	2
93621c6	-0.22	+0.21	+0.29	+0.38	+0.19	2
99940c6	-0.25	+0.33	+0.08	+0.16	+0.24	2
53554c6	+0.08	+0.26	+0.23	+0.26	-0.02	2

Table A.1: continued.

star ID	[Fe/H]	[Mg/Fe]	[Ca/Fe]	[Ti/Fe]	[Si/Fe]	Field
63690c6	+0.03	+0.07	+0.12	+0.37	-0.10	2
205097c6	+0.26	-0.04	+0.03	+0.00	-0.13	2
52922c6	-0.30	+0.33	+0.16	+0.27	+0.09	2
51954c6	+0.03	+0.12	+0.08	+0.03	+0.15	2
56533c6	+0.13	+0.16	+0.03	-0.11	+0.14	2
94909c7	-0.11	+0.17	+0.26	+0.28	+0.19	2
73484c7	+0.31	-0.22	+0.30	+0.55	-0.17	2
90995c7	-0.03	+0.21	+0.24	+0.20	-0.08	2
41505c7	-0.48	+0.36	+0.19	+0.46	+0.18	2
34034c7	+0.04	+0.16	+0.29	+0.37	+0.10	2
205852c7	+0.06	+0.22	+0.08	+0.22	+0.03	2
64944c7	+0.08	+0.11	+0.28	+0.19	+0.02	2
75601c7	-0.08	+0.18	+0.22	+0.20	+0.18	2
60208c7	-0.37	+0.27	-0.02	+0.13	+0.25	2
46088c7	-0.20	+0.20	+0.26	+0.35	+0.05	2
77743c7	+0.25	+0.04	-0.10	-0.05	+0.05	2
85832c7	+0.01	+0.23	+0.11	+0.05	+0.09	2
93881c7	+0.03	+0.14	+0.29	+0.19	+0.00	2
82739c7	-0.45	+0.35	+0.09	+0.43	+0.10	2
88860c7	-0.06	+0.22	+0.31	+0.33	+0.01	2
62874c7	-0.48	+0.36	+0.19	+0.31	+0.19	2
73636c7	-0.22	+0.29	+0.17	+0.27	+0.17	2
56730c7	+0.00	+0.29	+0.22	+0.27	+0.10	2
48678c7	+0.17	+0.22	+0.10	+0.18	+0.01	2
58592c7	+0.17	+0.01	+0.17	+0.27	-0.20	2
77419c7	+0.18	+0.05	+0.14	+0.10	+0.00	2
96001c8	+0.21	+0.15	+0.13	+0.15	+0.06	2
97453c7	+0.02	+0.03	+0.07	+0.23	+0.10	2
105594c7	-0.25	+0.27	+0.18	+0.32	+0.23	2
80262c8	+0.23	+0.11	+0.21	+0.22	-0.08	2
80419c8	+0.18	+0.07	+0.08	+0.04	+0.29	2
98090c7	-0.05	+0.00	+0.04	+0.26	+0.03	2
75382c8	+0.20	+0.07	+0.04	+0.15	+0.01	2
94445c7	-0.29	+0.35	+0.30	+0.39	+0.08	2
8683c4	+0.02	+0.11	+0.13	+0.18	+0.01	2
215027c7	+0.20	+0.29	+0.05	+0.03	+0.23	2
213817c7	+0.27	+0.08	+0.09	+0.17	-0.04	2
110776c7	-0.85	+0.32	+0.26	+0.27	+0.38	2
111007c8	+0.01	+0.14	+0.10	+0.16	+0.02	2
108627c7	+0.02	+0.19	+0.10	+0.39	-0.02	2

Table A.1: continued.

star ID	[Fe/H]	[Mg/Fe]	[Ca/Fe]	[Ti/Fe]	[Si/Fe]	Field
97461c8	+0.31	+0.03	+0.11	+0.26	-0.05	2
19346c3	+0.27	+0.02	+0.08	+0.03	-0.09	2
41112c4	-0.31	+0.36	+0.24	+0.35	+0.14	2
9081c3	-0.25	+0.39	+0.16	+0.51	+0.09	2
35643c4	+0.22	+0.15	+0.35	+0.48	-0.10	2
27350c4	-0.36	+0.25	+0.37	+0.41	+0.15	2
6693c3	-0.03	+0.19	+0.23	+0.33	+0.03	2
2002C3	-0.36	+0.14	+0.28	+0.36	+0.30	3
2374C3	-0.58	+0.17	+0.14	+0.45	+0.35	3
3142C3	-0.15	+0.27	+0.23	+0.38	+0.26	3
2947C3	-0.44	+0.27	+0.34	+0.23	+0.15	3
2200C3	-0.17	+0.14	+0.19	+0.14	+0.14	3
3018C3	-0.61	+0.31	+0.22	+0.40	+0.38	3
3515C5	+0.00	+0.16	+0.18	+0.08	+0.09	3
2769C3	+0.18	+0.13	+0.10	+0.28	-0.06	3
2470C3	-0.06	+0.20	+0.13	+0.25	+0.05	3
3267C3	+0.01	+0.13	+0.17	+0.30	+0.02	3
3161C3	-0.12	+0.21	+0.10	+0.23	+0.00	3
4365C3	-0.66	+0.21	+0.13	+0.39	+0.45	3
6549C6	+0.11	+0.20	+0.30	+0.21	+0.02	3
3733C3	-0.19	+0.16	+0.21	+0.16	+0.02	3
4085C3	-0.38	+0.27	+0.10	+0.30	+0.24	3
2525C2	-0.33	+0.27	+0.33	+0.30	+0.26	3
6505C6	-0.37	+0.27	+0.17	+0.34	+0.27	3
867C3	-0.46	+0.28	+0.24	+0.31	+0.20	3
222C3	-0.38	+0.27	+0.18	+0.28	+0.22	3
650C2	-0.67	+0.40	+0.30	+0.30	+0.31	3
1876C2	-0.86	+0.14	+0.21	+0.39	+0.43	3
2335C2	-0.84	+0.33	+0.31	+0.10	+0.39	3
1814C1	-0.39	+0.28	+0.29	+0.49	+0.28	3
2052C2	-0.94	+0.38	+0.10	+0.43	+0.40	3
1156C2	-0.36	+0.31	+0.11	+0.15	+0.39	3
2407C2	-0.70	+0.37	+0.29	+0.25	+0.34	3
1918C1	-0.36	+0.29	+0.18	+0.33	+0.26	3
1917C1	+0.18	+0.11	+0.03	+0.04	+0.17	3
6080C8	+0.11	+0.17	+0.10	+0.14	+0.22	3
6426C8	-0.39	+0.37	+0.28	+0.22	+0.34	3
6391C8	-0.59	+0.26	+0.31	+0.45	+0.31	3
6637C8	-0.26	+0.21	+0.17	+0.28	+0.27	3
431C2	-0.02	+0.25	+0.25	+0.24	-0.05	3

Table A.1: continued.

star ID	[Fe/H]	[Mg/Fe]	[Ca/Fe]	[Ti/Fe]	[Si/Fe]	Field
455C1	-0.57	+0.23	+0.29	+0.33	+0.39	3
6828C7	+0.17	-0.01	-0.01	-0.10	+0.11	3
608C1	-1.66	+0.09	-0.01	-0.10	+0.11	3
5487C8	-0.27	+0.16	+0.05	+0.17	+0.10	3
4478C8	-0.28	+0.23	+0.20	+0.24	+0.33	3
4740C8	-0.33	+0.25	+0.24	+0.47	+0.09	3
6913C7	-0.21	+0.19	+0.11	+0.24	+0.17	3
5351C8	-0.09	+0.22	+0.21	+0.28	+0.22	3
5400C8	+0.14	+0.09	+0.03	+0.04	+0.09	3
2812C8	-0.62	+0.24	+0.27	+0.30	+0.40	3
2772C7	-0.22	+0.31	+0.18	+0.39	+0.26	3
3191C7	-0.28	+0.39	+0.20	+0.24	+0.17	3
3091C8	-0.36	+0.29	+0.21	+0.41	+0.13	3
3711C7	-0.30	-0.07	+0.33	+0.34	+0.05	3
3035C7	-0.61	+0.18	+0.18	+0.33	+0.39	3
2110C7	-0.09	+0.23	+0.10	+0.37	+0.09	3
2220C7	-0.05	+0.32	+0.19	+0.44	+0.00	3
1554C7	-0.39	+0.22	+0.28	+0.45	+0.15	3
2178C7	-0.02	+0.14	-0.07	-0.16	+0.10	3
2422C7	+0.26	+0.16	+0.05	+0.02	+0.32	3
3101C7	-0.34	+0.25	+0.17	+0.30	+0.35	3
2580C6	+0.42	+0.09	+0.17	+0.30	+0.35	3
3238C6	-0.17	+0.19	+0.18	+0.40	+0.00	3
2532C6	-0.13	+0.28	+0.15	+0.09	+0.30	3
2948C7	+0.02	+0.25	+0.25	+0.01	+0.29	3
3690C7	-1.40	+0.28	+0.31	+0.46	+0.41	3
3796C6	-0.83	+0.31	+0.34	+0.43	+0.36	3
3201C6	-0.05	+0.27	+0.10	+0.20	+0.31	3
4217C6	-0.39	+0.30	+0.17	+0.41	+0.33	3
4333C6	-0.16	+0.21	+0.21	+0.28	+0.07	3
6164C6	-0.17	+0.31	+0.21	+0.36	+0.05	3
3350C6	-0.19	+0.31	+0.18	+0.19	+0.10	3
4263C6	-0.18	+0.44	+0.32	+0.30	+0.18	3
3558C6	-0.02	+0.33	+0.08	+0.18	+0.16	3
6090C6	+0.11	+0.18	+0.10	-0.12	+0.07	3
5543C6	+0.12	+0.22	+0.11	-0.20	+0.13	3
5908C6	-0.67	+0.33	+0.34	+0.43	+0.33	3
4876C6	-0.59	+0.28	+0.25	+0.52	+0.30	3
5319C6	-0.36	+0.34	+0.23	+0.40	+0.25	3
5977C6	+0.09	+0.18	-0.06	-0.04	+0.08	3

Table A.1: continued.

star ID	[Fe/H]	[Mg/Fe]	[Ca/Fe]	[Ti/Fe]	[Si/Fe]	Field
4612C6	-0.82	+0.19	+0.34	+0.46	+0.39	3
5588C6	-0.28	+0.27	+0.23	+0.45	+0.23	3
5664C6	+0.15	+0.26	+0.13	+0.05	+0.01	3
3965C6	-0.20	+0.28	+0.14	+0.32	+0.16	3
6717C6	-0.23	+0.25	+0.22	+0.23	+0.23	3
5980C6	-0.25	+0.15	+0.21	+0.30	+0.10	3
7119C5	-0.33	+0.40	+0.33	+0.44	+0.35	3
6419C5	-0.25	+0.31	+0.30	+0.34	+0.11	3
6230C5	+0.09	+0.11	+0.38	+0.15	-0.04	3
2502C3	-0.39	+0.25	+0.18	+0.43	+0.19	3
1754C3	-0.20	+0.34	+0.34	+0.31	+0.22	3
1407C3	-0.82	+0.37	+0.37	+0.43	+0.39	3
166C3	-0.86	+0.28	+0.09	+0.39	+0.41	3
96341C3	+0.03	+0.23	-0.10	+0.01	+0.42	4
240059C6	-0.66	+0.26	+0.29	+0.52	+0.10	4
77707C3	+0.09	+0.17	+0.10	+0.03	+0.14	4
77186C3	+0.15	+0.13	-0.02	-0.09	+0.05	4
88522C3	+0.15	+0.05	+0.02	+0.02	+0.13	4
135108C4	-0.39	+0.33	+0.21	+0.51	+0.33	4
83525C3	-0.05	+0.27	+0.29	+0.37	+0.14	4
130246C4	-0.21	+0.39	+0.20	+0.37	+0.38	4
127018C4	-0.14	+0.28	+0.09	+0.23	+0.30	4
95424C3	+0.17	+0.11	+0.04	+0.10	+0.06	4
98554C3	+0.09	+0.27	+0.09	+0.23	+0.04	4
101374C3	+0.29	-0.19	+0.15	-0.04	-0.05	4
100606C3	-0.83	+0.24	+0.31	+0.47	+0.35	4
82227C3	+0.08	+0.19	+0.08	+0.13	+0.09	4
83531C3	+0.19	+0.15	+0.03	+0.08	+0.06	4
242039C6	+0.20	+0.17	-0.02	+0.04	+0.05	4
101754C3	+0.30	+0.27	+0.12	+0.23	+0.03	4
80582C3	-0.02	+0.18	+0.16	+0.43	+0.10	4
47188C2	-0.48	+0.30	+0.16	+0.43	+0.35	4
51148C2	+0.11	+0.17	-0.17	+0.06	+0.01	4
52349C2	+0.10	+0.16	+0.07	+0.13	+0.08	4
57824C2	+0.27	+0.09	+0.07	+0.13	+0.08	4
237293C6	+0.18	+0.22	+0.06	-0.06	+0.00	4
45452C2	-0.64	+0.30	+0.34	+0.30	+0.43	4
46830C2	+0.19	+0.06	+0.17	+0.19	+0.08	4
48656C2	+0.31	+0.11	+0.15	-0.03	+0.10	4
77182C3	-0.19	+0.21	+0.08	-0.04	+0.15	4

Table A.1: continued.

star ID	[Fe/H]	[Mg/Fe]	[Ca/Fe]	[Ti/Fe]	[Si/Fe]	Field
49289C2	+0.24	+0.25	+0.03	-0.03	-0.03	4
44556C2	-0.07	+0.26	+0.01	+0.10	+0.35	4
278419C7	+0.03	+0.16	+0.27	+0.34	-0.03	4
279577C7	+0.02	+0.34	+0.12	+0.11	-0.04	4
229507C6	+0.13	-0.08	-0.01	+0.27	-0.21	4
271021C7	-0.18	+0.19	+0.10	+0.29	+0.22	4
230424C6	-0.72	+0.22	+0.23	+0.31	+0.39	4
230208C6	-0.09	+0.17	+0.08	+0.10	+0.09	4
284675C7	+0.02	+0.21	+0.03	+0.13	+0.09	4
225847C6	-0.13	+0.22	+0.21	+0.37	+0.09	4
266670C7	-0.23	+0.30	+0.33	+0.39	+0.19	4
268360C7	-0.21	+0.30	+0.11	+0.35	+0.11	4
270316C7	-0.25	-0.39	+0.38	+0.45	+0.08	4
270055C7	-0.14	+0.23	+0.25	+0.11	+0.12	4
271400C7	-0.09	+0.24	+0.37	+0.46	+0.11	4
270789C7	-0.14	+0.16	+0.36	+0.27	+0.19	4
270767C7	-0.19	+0.35	+0.32	+0.36	+0.10	4
265795C7	-0.19	+0.38	+0.32	+0.27	+0.13	4
255677C7	+0.02	+0.13	+0.09	+0.05	+0.06	4
268493C7	-0.22	+0.22	+0.28	+0.30	+0.18	4
271097C7	-0.24	+0.32	+0.23	+0.43	+0.23	4
261672C7	-0.11	+0.29	+0.28	+0.30	+0.18	4
259922C7	-0.18	+0.29	+0.09	+0.13	+0.21	4
265404C7	-0.14	+0.18	+0.15	+0.16	+0.16	4
224951C6	-0.02	+0.23	+0.17	+0.12	+0.11	4
260308C7	+0.10	+0.03	+0.04	-0.06	+0.09	4
233708C6	-0.05	+0.16	+0.18	+0.37	+0.03	4
208605C6	-0.10	+0.26	+0.10	+0.26	+0.25	4
256560C7	+0.01	+0.13	+0.13	-0.03	+0.11	4
258426C7	-0.34	+0.33	+0.19	+0.44	+0.30	4
259377C7	+0.10	+0.12	+0.09	+0.08	+0.10	4
256294C7	+0.19	+0.05	+0.14	+0.14	-0.02	4
208959C6	-0.12	+0.14	+0.11	+0.34	+0.18	4
209297C6	-0.04	+0.48	+0.08	+0.33	+0.08	4
210397C6	-0.30	+0.40	+0.34	+0.29	+0.25	4
231618C6	+0.01	+0.16	+0.20	+0.24	-0.02	4
228407C6	-0.19	+0.35	+0.27	+0.41	+0.11	4
224206C6	+0.16	+0.08	-0.02	-0.13	+0.14	4
211036C6	+0.24	-0.05	+0.21	-0.13	+0.07	4
226450C6	+0.15	+0.20	+0.02	+0.01	+0.13	4

Table A.1: continued.

star ID	[Fe/H]	[Mg/Fe]	[Ca/Fe]	[Ti/Fe]	[Si/Fe]	Field
178348C5	-0.08	+0.27	+0.18	+0.13	+0.30	4
227867C6	-0.21	+0.32	+0.15	+0.27	+0.25	4
223343C6	-0.06	+0.26	+0.26	+0.34	+0.01	4
223621C6	-0.02	+0.18	+0.04	+0.32	+0.07	4
219909C6	-0.61	+0.16	+0.38	+0.29	+0.42	4
221537C6	+0.14	+0.03	+0.10	+0.11	-0.04	4
213114C6	-0.02	+0.26	+0.08	+0.10	+0.13	4
237513C6	+0.24	+0.15	+0.01	-0.05	+0.06	4
207215C6	-0.25	+0.22	+0.24	+0.33	+0.16	4
223113C6	-0.17	+0.31	+0.18	+0.26	+0.16	4
183783C5	+0.12	+0.13	+0.08	+0.16	+0.03	4
184618C5	-0.32	+0.37	+0.23	+0.44	+0.23	4
225531C6	-0.68	+0.27	+0.21	+0.50	+0.38	4
181349C5	+0.09	+0.18	+0.04	-0.17	+0.20	4
180018C5	+0.02	+0.24	+0.28	+0.28	-0.01	4
226850C6	-0.79	+0.29	+0.28	+0.50	+0.48	4
227379C6	-0.10	+0.15	+0.32	+0.44	+0.19	4
197366C5	+0.01	+0.47	+0.11	+0.11	+0.18	4
193190C5	+0.05	+0.19	+0.26	+0.15	+0.07	4
232493C6	-1.19	+0.29	+0.31	+0.40	+0.41	4
185357C5	+0.22	+0.06	-0.10	-0.10	+0.00	4
187067C5	-0.99	+0.19	+0.22	+0.47	+0.44	4
231379C6	-0.32	+0.37	+0.39	+0.49	+0.12	4
185541C5	+0.15	+0.13	+0.09	+0.17	-0.06	4
129499C4	+0.01	+0.24	+0.06	+0.17	+0.03	4
228466C6	-0.89	+0.28	+0.09	+0.10	+0.53	4
125336C4	+0.04	+0.24	+0.06	+0.21	+0.03	4
125652C4	+0.12	+0.07	+0.07	+0.09	+0.03	4
239284C6	+0.18	+0.11	+0.05	+0.03	-0.09	4
82866C3	+0.16	+0.33	-0.20	+0.10	+0.01	4
240083C6	-0.57	+0.30	+0.28	+0.49	+0.20	4
90428C3	-0.41	+0.25	+0.01	+0.29	+0.39	4
81350C3	+0.27	-0.60	+0.01	+0.29	+0.39	4
81644C3	+0.05	+0.18	+0.07	+0.02	-0.06	4
86757C3	+0.00	+0.14	-0.14	-0.03	+0.08	4
132160C4	-0.58	+0.16	+0.24	+0.51	+0.30	4
85597C3	-0.12	+0.21	+0.21	+0.33	+0.06	4
129738C4	+0.27	+0.07	+0.09	+0.13	-0.17	4
90065C3	+0.21	+0.11	+0.12	+0.09	-0.08	4
238092C6	+0.47	+0.09	+0.12	+0.09	-0.08	4

Table A.1: continued.

star ID	[Fe/H]	[Mg/Fe]	[Ca/Fe]	[Ti/Fe]	[Si/Fe]	Field
286252C7	+0.05	+0.13	+0.17	+0.20	-0.01	4
42031C2	-0.09	+0.27	+0.01	+0.13	+0.11	4
52007C2	-0.33	+0.42	+0.22	+0.43	+0.05	4
53865C2	-0.02	+0.51	+0.05	+0.26	+0.09	4
45512C2	-0.31	+0.25	+0.10	+0.34	+0.28	4
277490C7	-0.50	+0.21	+0.12	+0.32	+0.41	4
46746C2	+0.29	+0.09	+0.12	+0.32	+0.41	4
44230C2	-0.45	+0.27	+0.16	+0.33	+0.30	4
282804C7	-0.07	+0.15	+0.07	+0.03	+0.12	4
50596C2	-0.37	+0.35	+0.28	+0.44	+0.18	4
43617C2	-0.24	+0.44	+0.15	+0.49	+0.23	4
275623C7	+0.06	+0.16	+0.01	+0.13	+0.06	4
275181C7	-0.04	-0.05	-0.10	+0.08	-0.10	4
277711C7	+0.02	+0.12	+0.08	+0.19	+0.00	4
284449C7	-0.50	+0.16	+0.10	+0.29	+0.36	4
276756C7	-0.50	+0.24	+0.17	+0.33	+0.36	4
285690C7	-0.61	+0.48	+0.30	+0.42	+0.49	4
286100C7	+0.25	+0.09	+0.30	+0.42	+0.49	4
267780C7	-0.67	+0.18	+0.35	+0.55	+0.34	4
269704C7	-0.22	+0.14	+0.14	+0.44	+0.11	4
266367C7	-0.44	+0.26	+0.29	+0.49	+0.14	4
274019C7	-0.29	+0.39	+0.29	+0.50	+0.23	4
262018C7	+0.22	+0.06	+0.03	+0.01	-0.02	4
256709C7	-0.18	+0.23	+0.08	+0.24	+0.22	4
261934C7	+0.08	+0.23	+0.03	+0.21	+0.02	4
268100C7	-0.31	+0.26	+0.21	+0.39	+0.20	4
259001C7	-0.63	+0.16	+0.13	+0.19	+0.41	4
262994C7	+0.01	+0.33	+0.06	+0.21	+0.01	4
259050C7	-0.39	+0.20	+0.14	+0.23	+0.22	4
266442C7	-0.37	+0.27	+0.29	+0.51	+0.22	4
263366C7	-0.24	+0.31	+0.29	+0.49	+0.13	4
261361C7	-0.21	+0.22	+0.18	+0.33	+0.22	4
224866C6	-0.37	+0.19	+0.10	+0.50	+0.26	4
215681C6	+0.08	+0.09	+0.03	+0.06	+0.10	4
230483C6	-0.33	+0.18	+0.12	+0.43	+0.14	4
216922C6	-0.07	+0.15	+0.13	+0.34	+0.20	4
249215C7	-0.52	+0.02	+0.10	+0.40	+0.32	4
223722C6	-0.65	+0.24	+0.17	+0.45	+0.39	4
252803C7	+0.04	+0.08	+0.08	+0.36	-0.05	4
257104C7	-0.02	+0.09	+0.11	+0.19	+0.18	4

Table A.1: continued.

star ID	[Fe/H]	[Mg/Fe]	[Ca/Fe]	[Ti/Fe]	[Si/Fe]	Field
223310C6	-0.27	+0.33	+0.11	+0.20	+0.26	4
223238C6	+0.15	+0.23	+0.02	+0.09	-0.04	4
223822C6	+0.22	+0.04	+0.05	+0.15	-0.10	4
210487C6	+0.30	-0.60	+0.01	-0.18	-0.07	4
204733C6	-0.39	+0.18	+0.12	+0.31	+0.37	4
175662C5	+0.12	+0.09	+0.12	+0.31	+0.37	4
172997C5	-0.17	+0.17	+0.22	+0.24	+0.19	4
218198C6	-0.21	+0.12	+0.17	+0.30	+0.21	4
175328C5	-0.12	+0.20	+0.24	+0.38	+0.17	4
169218C5	-0.01	+0.01	+0.13	+0.04	+0.18	4
169674C5	-0.65	+0.11	+0.36	+0.50	+0.34	4
166540C5	+0.19	-0.60	-0.10	+0.10	-0.07	4
166720C5	-0.43	+0.30	+0.14	+0.41	+0.34	4
220214C6	+0.36	+0.09	+0.14	+0.41	+0.34	4
230059C6	-0.54	+0.28	+0.20	+0.42	+0.33	4
213385C6	-0.59	+0.22	+0.17	+0.40	+0.45	4
217943C6	-0.12	-0.04	+0.09	+0.34	+0.09	4
187568C5	+0.10	+0.09	+0.09	+0.34	+0.09	4
185169C5	-0.42	+0.23	+0.23	+0.47	+0.23	4
184088C5	-0.54	+0.27	+0.24	+0.55	+0.30	4
181132C5	-0.07	+0.13	+0.08	+0.14	+0.10	4
178333C5	+0.13	+0.09	+0.08	+0.14	+0.10	4
176772C5	+0.05	+0.19	+0.01	+0.08	+0.06	4
119799C4	-0.38	+0.21	+0.08	+0.22	+0.26	4
233121C6	-0.41	+0.28	+0.07	+0.31	+0.24	4
233560C6	-0.27	+0.23	+0.00	+0.00	+0.17	4
186097C5	+0.52	+0.09	+0.00	+0.00	+0.17	4
84255C3	-0.69	+0.21	+0.24	+0.30	+0.38	4
82485C3	+0.18	+0.30	-0.01	+0.03	+0.01	4

Appendix B

Bulge VVV tile centre coordinates

Here we list the tile centre coordinates for all VVV pointings. There are 196 bulge tiles. For each tile we provide tile centre coordinates in Equatorial and Galactic coordinates. All tiles have been observed using the identical offsetting strategy, combining 6 pawprints to contiguously fill 1.5×1.1 sq. deg area. The second last column lists the filters for which the tile has been completed (i.e., observed within constraints), and the last column lists the number of epochs taken in K_s band within the first observing season (DR1).

Table B.1: VVV Tile centres for the Galactic bulge region.

Tile name	RA (J2000.0) dd:mm:ss.sss	DEC (J2000.0) dd:mm:ss.ss	longitude degrees	latitude degrees	Filters completed	K_s epochs completed
b201	18:04:24.384	-41:44:53.52	350.74816	-9.68974	ZYJHK _s	1
b202	18:08:00.144	-40:27:29.88	352.22619	-9.68971	ZYJHK _s	1
b203	18:11:29.496	-39:09:52.92	353.70409	-9.68973	ZYJHK _s	1
b204	18:14:52.992	-37:52:03.36	355.18207	-9.68974	ZYJHK _s	1
b205	18:18:11.136	-36:34:02.64	356.66012	-9.68976	ZYJHK _s	1
b206	18:21:24.360	-35:15:52.20	358.13813	-9.68975	ZYJHK _s	1
b207	18:24:33.096	-33:57:33.48	359.61607	-9.68977	ZYJHK _s	2
b208	18:27:37.728	-32:39:07.20	1.09399	-9.68974	ZYJHK _s	2
b209	18:30:38.640	-31:20:34.08	2.57200	-9.68971	ZYJHK _s	2
b210	18:33:36.168	-30:01:55.56	4.04998	-9.68973	ZYJHK _s	2
b211	18:36:30.624	-28:43:12.36	5.52796	-9.68978	ZYJHK _s	2
b212	18:39:22.272	-27:24:25.20	7.00593	-9.68975	ZYJHK _s	3
b213	18:42:11.424	-26:05:34.80	8.48396	-9.68974	ZYJHK _s	2
b214	18:44:58.320	-24:46:42.24	9.96193	-9.68974	ZYJHK _s	3
b215	17:59:15.960	-41:13:55.92	350.74595	-8.59756	ZYJHK _s	1
b216	18:02:55.992	-39:57:07.92	352.21956	-8.59753	ZYJHK _s	1
b217	18:06:29.472	-38:40:04.08	353.69327	-8.59756	ZYJHK _s	1
b218	18:09:56.880	-37:22:46.56	355.16684	-8.59757	ZYJHK _s	1
b219	18:13:18.768	-36:05:16.07	356.64051	-8.59760	ZYJHK _s	1

Table B.1: continued.

Tile name	RA (J2000.0) dd:mm:ss.sss	DEC (J2000.0) dd:mm:ss.ss	longitude degrees	latitude degrees	Filters completed	K_s epochs completed
b220	18:16:35.568	-34:47:34.08	358.11423	-8.59759	ZYJHK _s	1
b221	18:19:47.688	-33:29:42.36	359.58781	-8.59757	ZYJHK _s	2
b222	18:22:55.560	-32:11:41.28	1.06151	-8.59755	ZYJHK _s	2
b223	18:25:59.544	-30:53:32.28	2.53522	-8.59757	ZYJHK _s	2
b224	18:28:59.952	-29:35:16.80	4.00880	-8.59759	ZYJHK _s	2
b225	18:31:57.120	-28:16:54.84	5.48250	-8.59755	ZYJHK _s	2
b226	18:34:51.360	-26:58:27.84	6.95620	-8.59757	ZYJHK _s	3
b227	18:37:42.912	-25:39:56.88	8.42977	-8.59756	ZYJHK _s	2
b228	18:40:32.088	-24:21:21.96	9.90350	-8.59757	ZYJHK _s	3
b229	17:54:12.456	-40:42:07.56	350.74383	-7.50542	YJHK _s	1
b230	17:57:56.496	-39:25:54.48	352.21380	-7.50537	JHK _s	–
b231	18:01:33.792	-38:09:24.48	353.68363	-7.50537	JHK _s	1
b232	18:05:04.920	-36:52:38.28	355.15359	-7.50541	JHK _s	1
b233	18:08:30.312	-35:35:38.04	356.62342	-7.50539	JHK _s	1
b234	18:11:50.472	-34:18:24.48	358.09337	-7.50535	JHK _s	1
b235	18:15:05.832	-33:00:59.76	359.56322	-7.50542	JHK _s	2
b236	18:18:16.752	-31:43:24.24	1.03312	-7.50538	ZYJHK _s	2
b237	18:21:23.640	-30:25:39.36	2.50307	-7.50541	ZYJHK _s	2
b238	18:24:26.808	-29:07:46.20	3.97300	-7.50540	JHK _s	2
b239	18:27:26.568	-27:49:45.84	5.44287	-7.50536	JHK _s	2
b240	18:30:23.256	-26:31:39.36	6.91271	-7.50540	JHK _s	2
b241	18:33:17.136	-25:13:27.12	8.38261	-7.50541	JHK _s	3
b242	18:36:08.472	-23:55:10.20	9.85251	-7.50542	JHK _s	2
b243	17:49:13.848	-40:09:29.16	350.74206	-6.41324	YJHK _s	1
b244	17:53:01.608	-38:53:51.72	352.20875	-6.41323	JHK _s	–
b245	17:56:42.504	-37:37:54.84	353.67546	-6.41323	JHK _s	1
b246	18:00:17.064	-36:21:40.32	355.14219	-6.41321	JHK _s	1
b247	18:03:45.792	-35:05:09.96	356.60888	-6.41323	JHK _s	1
b248	18:07:09.120	-33:48:25.20	358.07550	-6.41322	JHK _s	1
b249	18:10:27.504	-32:31:27.12	359.54218	-6.41323	JHK _s	2
b250	18:13:41.328	-31:14:17.16	1.00886	-6.41325	ZYJHK _s	2
b251	18:16:50.952	-29:56:56.04	2.47562	-6.41319	JHK _s	2
b252	18:19:56.736	-28:39:25.92	3.94224	-6.41326	JHK _s	2
b253	18:22:58.968	-27:21:46.80	5.40892	-6.41319	JHK _s	2
b254	18:25:58.008	-26:04:00.12	6.87563	-6.41325	JHK _s	2
b255	18:28:54.072	-24:46:06.60	8.34231	-6.41319	JHK _s	3
b256	18:31:47.496	-23:28:07.32	9.80903	-6.41325	JHK _s	2
b257	17:44:20.112	-39:36:02.16	350.74076	-5.32104	JHK _s	1
b258	17:48:11.328	-38:20:59.64	352.20485	-5.32102	JHK _s	1

Table B.1: continued.

Tile name	RA (J2000.0) dd:mm:ss.sss	DEC (J2000.0) dd:mm:ss.ss	longitude degrees	latitude degrees	Filters completed	K_s epochs completed
b259	17:51:55.560	-37:05:36.24	353.66885	-5.32101	<i>JHK_s</i>	–
b260	17:55:33.360	-35:49:53.40	355.13291	-5.32104	<i>JHK_s</i>	–
b261	17:59:05.184	-34:33:52.92	356.59692	-5.32103	<i>JHK_s</i>	–
b262	18:02:31.512	-33:17:36.24	358.06096	-5.32105	<i>JHK_s</i>	–
b263	18:05:52.752	-32:01:04.80	359.52500	-5.32104	<i>JHK_s</i>	–
b264	18:09:09.288	-30:44:20.04	0.98899	-5.32099	<i>JHK_s</i>	–
b265	18:12:21.528	-29:27:23.40	2.45295	-5.32106	<i>JHK_s</i>	–
b266	18:15:29.784	-28:10:15.24	3.91703	-5.32105	<i>JHK_s</i>	–
b267	18:18:34.368	-26:52:57.36	5.38103	-5.32101	<i>JHK_s</i>	–
b268	18:21:35.616	-25:35:30.48	6.84507	-5.32101	<i>JHK_s</i>	–
b269	18:24:33.792	-24:17:55.68	8.30909	-5.32100	<i>JHK_s</i>	1
b270	18:27:29.184	-23:00:14.04	9.77309	-5.32107	<i>ZYJHK_s</i>	1
b271	17:39:31.128	-39:01:49.44	350.73953	-4.22883	<i>JHK_s</i>	1
b272	17:43:25.536	-37:47:22.20	352.20141	-4.22884	<i>JHK_s</i>	1
b273	17:47:12.888	-36:32:31.92	353.66332	-4.22886	<i>JHK_s</i>	1
b274	17:50:53.688	-35:17:20.76	355.12516	-4.22890	<i>JHK_s</i>	1
b275	17:54:28.416	-34:01:49.80	356.58709	-4.22886	<i>JHK_s</i>	1
b276	17:57:57.528	-32:46:01.20	358.04898	-4.22882	<i>JHK_s</i>	1
b277	18:01:21.456	-31:29:56.40	359.51088	-4.22881	<i>JHK_s</i>	1
b278	18:04:40.584	-30:13:36.84	0.97275	-4.22884	<i>JHK_s</i>	1
b279	18:07:55.272	-28:57:03.60	2.43463	-4.22884	<i>JHK_s</i>	1
b280	18:11:05.880	-27:40:17.76	3.89659	-4.22886	<i>JHK_s</i>	1
b281	18:14:12.696	-26:23:20.76	5.35849	-4.22883	<i>JHK_s</i>	1
b282	18:17:16.056	-25:06:13.68	6.82039	-4.22886	<i>JHK_s</i>	1
b283	18:20:16.224	-23:48:57.60	8.28222	-4.22888	<i>JHK_s</i>	–
b284	18:23:13.488	-22:31:32.88	9.74416	-4.22889	<i>JHK_s</i>	–
b285	17:34:46.896	-38:26:51.72	350.73871	-3.13666	<i>JHK_s</i>	–
b286	17:38:44.256	-37:12:59.40	352.19896	-3.13670	<i>JHK_s</i>	–
b287	17:42:34.488	-35:58:41.88	353.65931	-3.13670	<i>JHK_s</i>	–
b288	17:46:18.096	-34:44:01.68	355.11962	-3.13673	<i>ZYJHK_s</i>	–
b289	17:49:55.536	-33:29:00.24	356.57994	-3.13668	<i>ZYJHK_s</i>	1
b290	17:53:27.288	-32:13:39.72	358.04023	-3.13673	<i>ZYJHK_s</i>	1
b291	17:56:53.736	-30:58:01.20	359.50054	-3.13672	<i>ZYJHK_s</i>	–
b292	18:00:15.264	-29:42:06.12	0.96088	-3.13663	<i>ZY</i>	–
b293	18:03:32.280	-28:25:56.28	2.42120	-3.13666	<i>ZY</i>	–
b294	18:06:45.096	-27:09:32.75	3.88150	-3.13671	<i>ZYJHK_s</i>	–
b295	18:09:54.024	-25:52:56.64	5.34179	-3.13672	<i>ZYJHK_s</i>	–
b296	18:12:59.352	-24:36:09.00	6.80204	-3.13666	<i>ZYJHK_s</i>	–
b297	18:16:01.416	-23:19:10.92	8.26235	-3.13668	<i>ZYJHK_s</i>	1

Table B.1: continued.

Tile name	RA (J2000.0) dd:mm:ss.sss	DEC (J2000.0) dd:mm:ss.ss	longitude degrees	latitude degrees	Filters completed	K_s epochs completed
b298	18:19:00.456	-22:02:03.12	9.72271	-3.13666	<i>JHK_s</i>	1
b299	17:30:07.272	-37:51:11.88	350.73789	-2.04453	<i>JHK_s</i>	–
b300	17:34:07.344	-36:37:53.76	352.19711	-2.04451	<i>JHK_s</i>	–
b301	17:38:00.240	-35:24:09.00	353.65635	-2.04453	<i>ZYJHK_s</i>	–
b302	17:41:46.440	-34:09:59.40	355.11565	-2.04449	<i>ZYJHK_s</i>	–
b303	17:45:26.424	-32:55:27.48	356.57487	-2.04453	<i>ZYJHK_s</i>	1
b304	17:49:00.600	-31:40:34.32	358.03411	-2.04446	<i>ZYJHK_s</i>	1
b305	17:52:29.424	-30:25:22.08	359.49334	-2.04452	<i>ZYJHK_s</i>	–
b306	17:55:53.256	-29:09:51.84	0.95261	-2.04456	<i>ZYJHK_s</i>	–
b307	17:59:12.432	-27:54:05.04	2.41186	-2.04451	<i>ZYJHK_s</i>	–
b308	18:02:27.312	-26:38:03.12	3.87111	-2.04447	<i>ZYJHK_s</i>	–
b309	18:05:38.232	-25:21:47.52	5.33034	-2.04451	<i>ZYJHK_s</i>	–
b310	18:08:45.480	-24:05:18.96	6.78962	-2.04454	<i>ZYJHK_s</i>	–
b311	18:11:49.320	-22:48:38.52	8.24891	-2.04449	<i>ZYJHK_s</i>	1
b312	18:14:50.040	-21:31:47.64	9.70816	-2.04447	<i>JHK_s</i>	1
b313	17:25:32.232	-37:14:49.92	350.73753	-0.95236	<i>JHK_s</i>	1
b314	17:29:34.800	-36:02:05.64	352.19625	-0.95230	<i>JHK_s</i>	1
b315	17:33:30.168	-34:48:52.92	353.65504	-0.95232	<i>JHK_s</i>	1
b316	17:37:18.768	-33:35:14.28	355.11368	-0.95231	<i>JHK_s</i>	1
b317	17:41:01.104	-32:21:10.80	356.57248	-0.95229	<i>JHK_s</i>	1
b318	17:44:37.584	-31:06:45.00	358.03121	-0.95230	<i>JHK_s</i>	1
b319	17:48:08.616	-29:51:58.32	359.48996	-0.95233	<i>JHK_s</i>	1
b320	17:51:34.560	-28:36:52.56	0.94861	-0.95235	<i>JHK_s</i>	1
b321	17:54:55.800	-27:21:28.44	2.40742	-0.95234	<i>JHK_s</i>	1
b322	17:58:12.648	-26:05:48.12	3.86612	-0.95234	<i>JHK_s</i>	1
b323	18:01:25.416	-24:49:52.68	5.32477	-0.95232	<i>JHK_s</i>	1
b324	18:04:34.440	-23:33:42.84	6.78355	-0.95232	<i>JHK_s</i>	1
b325	18:07:39.984	-22:17:20.40	8.24226	-0.95238	<i>JHK_s</i>	–
b326	18:10:42.288	-21:00:45.72	9.70101	-0.95231	<i>JHK_s</i>	–
b327	17:21:01.656	-36:37:48.00	350.73744	0.13984	<i>JHK_s</i>	1
b328	17:25:06.528	-35:25:37.20	352.19621	0.13989	<i>JHK_s</i>	1
b329	17:29:04.152	-34:12:56.52	353.65492	0.13987	<i>JHK_s</i>	–
b330	17:32:55.008	-32:59:47.76	355.11368	0.13984	<i>JHK_s</i>	–
b331	17:36:39.504	-31:46:13.08	356.57236	0.13988	<i>JHK_s</i>	–
b332	17:40:18.120	-30:32:14.28	358.03110	0.13982	<i>JHK_s</i>	–
b333	17:43:51.192	-29:17:52.80	359.48985	0.13988	<i>JHK_s</i>	–
b334	17:47:19.128	-28:03:10.80	0.94855	0.13988	<i>JHK_s</i>	–
b335	17:50:42.288	-26:48:09.36	2.40731	0.13985	<i>JHK_s</i>	–
b336	17:54:00.984	-25:32:49.92	3.86610	0.13985	<i>JHK_s</i>	–

Table B.1: continued.

Tile name	RA (J2000.0) dd:mm:ss.sss	DEC (J2000.0) dd:mm:ss.ss	longitude degrees	latitude degrees	Filters completed	K_s epochs completed
b337	17:57:15.528	-24:17:14.28	5.32478	0.13981	<i>JHK_s</i>	–
b338	18:00:26.208	-23:01:23.16	6.78348	0.13983	<i>JHK_s</i>	–
b339	18:03:33.336	-21:45:17.64	8.24226	0.13983	<i>JHK_s</i>	1
b340	18:06:37.152	-20:28:59.16	9.70099	0.13985	<i>ZYJHK_s</i>	1
b341	17:16:35.472	-36:00:07.56	350.73765	1.23203	<i>ZYJHK_s</i>	1
b342	17:20:42.432	-34:48:30.24	352.19686	1.23205	<i>JHK_s</i>	1
b343	17:24:42.144	-33:36:20.88	353.65613	1.23203	<i>JHK_s</i>	1
b344	17:28:35.040	-32:23:41.64	355.11542	1.23207	<i>JHK_s</i>	1
b345	17:32:21.576	-31:10:35.04	356.57468	1.23205	<i>JHK_s</i>	1
b346	17:36:02.160	-29:57:02.52	358.03399	1.23203	<i>JHK_s</i>	1
b347	17:39:37.152	-28:43:06.24	359.49322	1.23206	<i>JHK_s</i>	1
b348	17:43:06.960	-27:28:47.64	0.95251	1.23203	<i>JHK_s</i>	1
b349	17:46:31.896	-26:14:08.52	2.41172	1.23201	<i>JHK_s</i>	1
b350	17:49:52.296	-24:59:09.96	3.87096	1.23204	<i>JHK_s</i>	1
b351	17:53:08.496	-23:43:53.40	5.33027	1.23202	<i>JHK_s</i>	–
b352	17:56:20.760	-22:28:20.28	6.78955	1.23201	<i>ZYJHK_s</i>	–
b353	17:59:29.376	-21:12:31.68	8.24885	1.23202	<i>ZYJHK_s</i>	–
b354	18:02:34.608	-19:56:29.04	9.70808	1.23199	<i>ZYJHK_s</i>	–
b355	17:12:13.584	-35:21:49.68	350.73827	2.32427	<i>ZYJHK_s</i>	1
b356	17:16:22.488	-34:10:45.12	352.19857	2.32417	<i>ZY</i>	1
b357	17:20:24.096	-32:59:06.36	353.65894	2.32423	<i>ZY</i>	–
b358	17:24:18.888	-31:46:56.64	355.11924	2.32422	<i>ZY</i>	–
b361	17:35:26.472	-28:07:39.36	359.50024	2.32421	<i>ZY</i>	–
b362	17:38:58.008	-26:53:43.80	0.96059	2.32418	<i>ZYJHK_s</i>	–
b363	17:42:24.624	-25:39:25.92	2.42098	2.32420	<i>ZYJHK_s</i>	–
b364	17:45:46.632	-24:24:47.88	3.88124	2.32419	<i>ZYJHK_s</i>	–
b365	17:49:04.368	-23:09:50.40	5.34158	2.32416	<i>ZYJHK_s</i>	–
b366	17:52:18.096	-21:54:34.92	6.80192	2.32418	<i>JHK_s</i>	1
b367	17:55:28.104	-20:39:02.88	8.26224	2.32419	<i>JHK_s</i>	1
b368	17:58:34.656	-19:23:15.00	9.72265	2.32423	<i>JHK_s</i>	1
b369	17:07:55.872	-34:42:57.24	350.73892	3.41637	<i>ZYJHK_s</i>	1
b370	17:12:06.480	-33:32:24.36	352.20083	3.41644	<i>ZYJHK_s</i>	1
b371	17:16:09.864	-32:21:16.20	353.66280	3.41638	<i>ZYJHK_s</i>	–
b372	17:20:06.384	-31:09:35.28	355.12466	3.41637	<i>ZYJHK_s</i>	–
b373	17:23:56.496	-29:57:23.04	356.58663	3.41642	<i>ZYJHK_s</i>	–
b374	17:27:40.584	-28:44:42.36	358.04853	3.41640	<i>ZYJHK_s</i>	–
b375	17:31:19.032	-27:31:34.68	359.51046	3.41635	<i>ZYJHK_s</i>	–
b376	17:34:52.152	-26:18:01.44	0.97243	3.41644	<i>ZYJHK_s</i>	–
b377	17:38:20.328	-25:04:05.16	2.43434	3.41638	<i>ZYJHK_s</i>	–

Table B.1: continued.

Tile name	RA (J2000.0) dd:mm:ss.sss	DEC (J2000.0) dd:mm:ss.ss	longitude degrees	latitude degrees	Filters completed	K_s epochs completed
b378	17:41:43.848	-23:49:46.56	3.89631	3.41638	<i>ZYJHK_s</i>	–
b379	17:45:03.024	-22:35:07.44	5.35828	3.41637	<i>ZYJHK_s</i>	1
b380	17:48:18.120	-21:20:09.24	6.82020	3.41640	<i>ZYJHK_s</i>	1
b381	17:51:29.424	-20:04:53.40	8.28204	3.41640	<i>JHK_s</i>	1
b382	17:54:37.224	-18:49:20.64	9.74399	3.41636	<i>JHK_s</i>	1
b383	17:03:42.216	-34:03:30.60	350.73979	4.50856	<i>ZYJHK_s</i>	1
b384	17:07:54.408	-32:53:29.40	352.20380	4.50857	<i>JHK_s</i>	1
b385	17:11:59.352	-31:42:51.12	353.66783	4.50858	<i>JHK_s</i>	1
b386	17:15:57.480	-30:31:37.92	355.13195	4.50860	<i>JHK_s</i>	1
b387	17:19:49.176	-29:19:52.68	356.59597	4.50856	<i>JHK_s</i>	1
b388	17:23:34.824	-28:07:36.84	358.06004	4.50857	<i>JHK_s</i>	1
b389	17:27:14.784	-26:54:52.56	359.52411	4.50859	<i>JHK_s</i>	1
b390	17:30:45.384	-25:43:05.52	0.96034	4.50854	<i>JHK_s</i>	1
b391	17:34:15.096	-24:29:30.12	2.42444	4.50852	<i>JHK_s</i>	1
b392	17:37:40.080	-23:15:31.32	3.88850	4.50858	<i>JHK_s</i>	1
b393	17:41:00.672	-22:01:10.92	5.35253	4.50853	<i>JHK_s</i>	–
b394	17:44:17.136	-20:46:29.64	6.81666	4.50854	<i>JHK_s</i>	–
b395	17:47:29.736	-19:31:29.28	8.28074	4.50857	<i>ZYJHK_s</i>	–
b396	17:50:38.736	-18:16:11.28	9.74476	4.50855	<i>ZYJHK_s</i>	–

Bibliography

- Alard, C. 2001, *A&A*, 379, L44
- Alonso, A., Arribas, S., & Martínez-Roger, C. 1999, 140, 261
- Alves, D. R. 2000, *ApJ*, 539, 732
- Alves, D. R., Rejkuba, M., Minniti, D., & Cook, K. H. 2002, *ApJ*, 573, L51
- Alves-Brito, A., Meléndez, J., Asplund, M., Ramírez, I., & Yong, D. 2010, *A&A*, 513, A35+
- Asplund, M., Grevesse, N., Sauval, A. J., & Scott, P. 2009, *ARA&A*, 47, 481
- Athanassoula, E. 2005, *MNRAS*, 358, 1477
- Athanassoula, E. & Misiriotis, A. 2002, *MNRAS*, 330, 35
- Babusiaux, C. & Gilmore, G. 2005, *MNRAS*, 358, 1309
- Babusiaux, C., Gómez, A., Hill, V., et al. 2010, *A&A*, 519, A77+
- Bagnulo, S., Jehin, E., Ledoux, C., et al. 2003, *The Messenger*, 114, 10
- Bensby, T., Adén, D., Meléndez, J., et al. 2011, *A&A*, 533, A134
- Bensby, T., Alves-Brito, A., Oey, M. S., Yong, D., & Meléndez, J. 2010a, *A&A*, 516, L13+
- Bensby, T., Feltzing, S., Johnson, J. A., et al. 2010b, *A&A*, 512, A41+
- Bertelli, G., Bressan, A., Chiosi, C., Fagotto, F., & Nasi, E. 1994, 106, 275
- Bissantz, N. & Gerhard, O. 2002, *MNRAS*, 330, 591
- Bournaud, F., Elmegreen, B. G., & Martig, M. 2009, *ApJ*, 707, L1
- Brown, T. M., Sahu, K., Anderson, J., et al. 2010, *ApJ*, 725, L19
- Bureau, M., Aronica, G., Athanassoula, E., et al. 2006, *MNRAS*, 370, 753
- Bureau, M. & Freeman, K. C. 1999, *AJ*, 118, 126

- Burstein, D., Faber, S. M., Gaskell, C. M., & Krumm, N. 1984, *ApJ*, 287, 586
- Burstein, D. & Heiles, C. 1982, *AJ*, 87, 1165
- Cabrera-Lavers, A., Hammersley, P. L., González-Fernández, C., et al. 2007, *A&A*, 465, 825
- Cappellari, M., Emsellem, E., Krajnović, D., et al. 2011, *MNRAS*, 413, 813
- Cardelli, J. A., Clayton, G. C., & Mathis, J. S. 1989, *ApJ*, 345, 245
- Carney, B. W., Lee, J.-W., & Dodson, B. 2005, *AJ*, 129, 656
- Carollo, C. M., Scarlata, C., Stiavelli, M., Wyse, R. F. G., & Mayer, L. 2007, *ApJ*, 658, 960
- Casetti-Dinescu, D. I., Girard, T. M., Korchagin, V. I., & van Altena, W. F. 2011, *ApJ*, 728, 7
- Clarkson, W., Sahu, K., Anderson, J., et al. 2008, *ApJ*, 684, 1110
- Clarkson, W. I., Sahu, K. C., Anderson, J., et al. 2011, *ApJ*, 735, 37
- Combes, F., Debbasch, F., Friedli, D., & Pfenniger, D. 1990, *A&A*, 233, 82
- Combes, F. & Sanders, R. H. 1981, *A&A*, 96, 164
- Daddi, E., Bournaud, F., Walter, F., et al. 2010, *ApJ*, 713, 686
- Debattista, V. P., Carollo, C. M., Mayer, L., & Moore, B. 2005, *ApJ*, 628, 678
- Debattista, V. P., Mayer, L., Carollo, C. M., et al. 2006, *ApJ*, 645, 209
- Debattista, V. P. & Sellwood, J. A. 1998, *ApJ*, 493, L5
- Debattista, V. P. & Williams, T. B. 2004, *ApJ*, 605, 714
- Dwek, E., Arendt, R. G., Hauser, M. G., et al. 1995, *ApJ*, 445, 716
- Elia Garcia Perez, A., Allende Prieto, C., Bizyaev, D., et al. 2012, in *American Astronomical Society Meeting Abstracts*, Vol. 219, American Astronomical Society Meeting Abstracts, 410.04
- Elmegreen, B. G., Bournaud, F., & Elmegreen, D. M. 2008, *ApJ*, 688, 67
- Emerson, J. P. & Sutherland, W. J. 2010, in *Presented at the Society of Photo-Optical Instrumentation Engineers (SPIE) Conference*, Vol. 7733, Society of Photo-Optical Instrumentation Engineers (SPIE) Conference Series
- Emerson, J. P., Sutherland, W. J., McPherson, A. M., et al. 2004, *The Messenger*, 117, 27
- Emsellem, E., Cappellari, M., Peletier, R. F., et al. 2004, *MNRAS*, 352, 721

- Erwin, P. 2011, *Memorie della Societa Astronomica Italiana Supplementi*, 18, 145
- Eskridge, P. B., Frogel, J. A., Pogge, R. W., et al. 2000, *AJ*, 119, 536
- Feltzing, S. 2011, in *Stellar Clusters & Associations: A RIA Workshop on Gaia*, 311–320
- Förster Schreiber, N. M., Genzel, R., Bouché, N., et al. 2009, *ApJ*, 706, 1364
- Freeman, K. C. 2008, in *IAU Symposium, Vol. 245, IAU Symposium*, ed. M. Bureau, E. Athanassoula, & B. Barbuy, 3–10
- Fukugita, M., Hogan, C. J., & Peebles, P. J. E. 1998, *ApJ*, 503, 518
- Fulbright, J. P., McWilliam, A., & Rich, R. M. 2006, *ApJ*, 636, 821
- Fulbright, J. P., McWilliam, A., & Rich, R. M. 2007, *ApJ*, 661, 1152
- Gadotti, D. A. 2009, *MNRAS*, 393, 1531
- Gadotti, D. A. 2011, *ArXiv:1101.2714*
- Gadotti, D. A. & de Souza, R. E. 2006, 163, 270
- Genzel, R., Burkert, A., Bouché, N., et al. 2008, *ApJ*, 687, 59
- Genzel, R., Tacconi, L. J., Eisenhauer, F., et al. 2006, *Nat*, 442, 786
- Gerhard, O. & Martinez-Valpuesta, I. 2012, *ApJ*, 744, L8
- Girardi, L. & Salaris, M. 2001, *MNRAS*, 323, 109
- Gonzalez, O. A., Rejkuba, M., Minniti, D., et al. 2011a, *A&A*, 534, L14
- Gonzalez, O. A., Rejkuba, M., Zoccali, M., et al. 2011b, *A&A*, 530, A54+
- Gonzalez, O. A., Rejkuba, M., Zoccali, M., Valenti, E., & Minniti, D. 2011c, *A&A*, 534, A3
- Gratton, R. G. & Sneden, C. 1990, *A&A*, 234, 366
- Greggio, L. 2010, *MNRAS*, 406, 22
- Grocholski, A. J. & Sarajedini, A. 2002, *AJ*, 123, 1603
- Gustafsson, B., Edvardsson, B., Eriksson, K., et al. 2008, *A&A*, 486, 951
- Hill, V., Lecureur, A., Gomez, A., et al. 2011, *aap*
- Hopkins, P. F., Bundy, K., Croton, D., et al. 2010, *ApJ*, 715, 202
- Howard, C. D., Rich, R. M., Clarkson, W., et al. 2009, *ApJ*, 702, L153

- Immeli, A., Samland, M., Gerhard, O., & Westera, P. 2004, *A&A*, 413, 547
- Indebetouw, R., Mathis, J. S., Babler, B. L., et al. 2005, *ApJ*, 619, 931
- Jablonka, P., Gorgas, J., & Goudfrooij, P. 2007, *A&A*, 474, 763
- Jablonka, P. & Sarajedini, A. 2005, in *IAU Symposium, Vol. 228, From Lithium to Uranium: Elemental Tracers of Early Cosmic Evolution*, ed. V. Hill, P. François, & F. Primas, 525–530
- Johnson, C. I., Rich, R. M., Fulbright, J. P., Valenti, E., & McWilliam, A. 2011, *ApJ*, 732, 108
- Kauffmann, G., Colberg, J. M., Diaferio, A., & White, S. D. M. 1999, *MNRAS*, 303, 188
- Kormendy, J. & Barentine, J. C. 2010, *ApJ*, 715, L176
- Kormendy, J. & Bruzual A., G. 1978, *ApJ*, 223, L63
- Kormendy, J. & Illingworth, G. 1982, *ApJ*, 256, 460
- Kormendy, J. & Kennicutt, Jr., R. C. 2004, *ARA&A*, 42, 603
- Kuijken, K. & Merrifield, M. R. 1995, *ApJ*, 443, L13
- Kunder, A., Popowski, P., Cook, K. H., & Chaboyer, B. 2008, *AJ*, 135, 631
- Lackner, C. N. & Gunn, J. E. 2012, *MNRAS*, 421, 2277
- Laine, S., Shlosman, I., Knapen, J. H., & Peletier, R. F. 2002, *ApJ*, 567, 97
- Laney, C. D., Joner, M. D., & Pietrzyński, G. 2012, *MNRAS*, 419, 1637
- Lecureur, A., Hill, V., Zoccali, M., et al. 2007, *A&A*, 465, 799
- Lewis, J. R., Irwin, M., & Bunclark, P. 2010, in *Astronomical Society of the Pacific Conference Series, Vol. 434, Astronomical Data Analysis Software and Systems XIX*, ed. Y. Mizumoto, K.-I. Morita, & M. Ohishi, 91–+
- Lianou, S., Grebel, E. K., & Koch, A. 2011, *ArXiv e-prints*
- MacArthur, L. A., Ellis, R. S., Treu, T., et al. 2008, *ApJ*, 680, 70
- Marshall, D. J., Robin, A. C., Reylé, C., Schultheis, M., & Picaud, S. 2006, *A&A*, 453, 635
- Martinez-Valpuesta, I., Shlosman, I., & Heller, C. 2006, *ApJ*, 637, 214
- Matteucci, F. 2003, *Ap&SS*, 284, 539
- Matteucci, F. & Greggio, L. 1986, *A&A*, 154, 279
- McWilliam, A. & Rich, R. M. 1994, 91, 749

- McWilliam, A. & Zoccali, M. 2010, *ApJ*, 724, 1491
- Meléndez, J., Asplund, M., Alves-Brito, A., et al. 2008, *A&A*, 484, L21
- Minniti, D., Lucas, P. W., Emerson, J. P., et al. 2010, 15, 433
- Minniti, D., Saito, R. K., Alonso-García, J., Lucas, P. W., & Hempel, M. 2011, *ApJ*, 733, L43+
- Moorthy, B. K. & Holtzman, J. A. 2006, *MNRAS*, 371, 583
- Nakasato, N. & Nomoto, K. 2003, *ApJ*, 588, 842
- Nataf, D. M., Udalski, A., Gould, A., Fouqué, P., & Stanek, K. Z. 2010, *ApJ*, 721, L28
- Nataf, D. M., Udalski, A., Gould, A., & Pinsonneault, M. H. 2011, *ApJ*, 730, 118
- Ness, M. & Freeman, K. 2012, *Assembling the Puzzle of the Milky Way*, Le Grand-Bornand, France, Edited by C. Reylé; A. Robin; M. Schultheis; EPJ Web of Conferences, Volume 19, id.06003, 19, 6003
- Nishiyama, S., Nagata, T., Baba, D., et al. 2005, *ApJ*, 621, L105
- Nishiyama, S., Nagata, T., Kusakabe, N., et al. 2006, *ApJ*, 638, 839
- Nishiyama, S., Nagata, T., Tamura, M., et al. 2008, *ApJ*, 680, 1174
- Nishiyama, S., Tamura, M., Hatano, H., et al. 2009, *ApJ*, 696, 1407
- Origlia, L., Valenti, E., Rich, R. M., & Ferraro, F. R. 2006, *ApJ*, 646, 499
- Ortolani, S., Renzini, A., Gilmozzi, R., et al. 1995, *Nat*, 377, 701
- Paczynski, B. & Stanek, K. Z. 1998, *ApJ*, 494, L219+
- Pasquini, L., Alonso, J., Avila, G., et al. 2003, in Presented at the Society of Photo-Optical Instrumentation Engineers (SPIE) Conference, Vol. 4841, Society of Photo-Optical Instrumentation Engineers (SPIE) Conference Series, ed. M. Iye & A. F. M. Moorwood, 1682–1693
- Patsis, P. A., Skokos, C., & Athanassoula, E. 2002, *MNRAS*, 337, 578
- Peletier, R. F., Balcells, M., Davies, R. L., et al. 1999, *MNRAS*, 310, 703
- Peletier, R. F., Falcón-Barroso, J., Bacon, R., et al. 2007, *MNRAS*, 379, 445
- Peng, Y., Lilly, S. J., Kovač, K., et al. 2010, *ApJ*, 721, 193
- Pérez, I., Sánchez-Blázquez, P., & Zurita, A. 2009, *A&A*, 495, 775
- Pietrinferni, A., Cassisi, S., Salaris, M., & Castelli, F. 2004, *ApJ*, 612, 168

- Pietrzyński, G., Gieren, W., & Udalski, A. 2003, *AJ*, 125, 2494
- Plez, B. 1998, *A&A*, 337, 495
- Ramírez, I. & Meléndez, J. 2005, *ApJ*, 626, 446
- Rangwala, N., Williams, T. B., & Stanek, K. Z. 2009, *ApJ*, 691, 1387
- Rattenbury, N. J., Mao, S., Sumi, T., & Smith, M. C. 2007, *MNRAS*, 378, 1064
- Rejkuba, M., Greggio, L., Harris, W. E., Harris, G. L. H., & Peng, E. W. 2005, *ApJ*, 631, 262
- Renzini, A. 1998, *AJ*, 115, 2459
- Renzini, A. 2009, *MNRAS*, 398, L58
- Rich, R. M., Origlia, L., & Valenti, E. 2007, *ApJ*, 665, L119
- Rieke, G. H. & Lebofsky, M. J. 1985, *ApJ*, 288, 618
- Robin, A. C., Marshall, D. J., Schultheis, M., & Reylé, C. 2012, *A&A*, 538, A106
- Robin, A. C., Reylé, C., Derrière, S., & Picaud, S. 2003, *A&A*, 409, 523
- Rodriguez-Fernandez, N. J. & Combes, F. 2008, *A&A*, 489, 115
- Saito, R., Hempel, M., Alonso-García, J., et al. 2010, *The Messenger*, 141, 24
- Saito, R. K., Hempel, M., Minniti, D., et al. 2012, *A&A*, 537, A107
- Saito, R. K., Zoccali, M., McWilliam, A., et al. 2011, *AJ*, 142, 76
- Salaris, M. & Girardi, L. 2002, *MNRAS*, 337, 332
- Samland, M. & Gerhard, O. E. 2003, *A&A*, 399, 961
- Savage, B. D. & Mathis, J. S. 1979, *ARA&A*, 17, 73
- Schlegel, D. J., Finkbeiner, D. P., & Davis, M. 1998, *ApJ*, 500, 525
- Schultheis, M., Ganesh, S., Simon, G., et al. 1999, *A&A*, 349, L69
- Schultheis, M., Sellgren, K., Ramírez, S., et al. 2009, *A&A*, 495, 157
- Sharp, R., Saunders, W., Smith, G., et al. 2006, in *Society of Photo-Optical Instrumentation Engineers (SPIE) Conference Series*, Vol. 6269, Society of Photo-Optical Instrumentation Engineers (SPIE) Conference Series
- Shen, J., Rich, R. M., Kormendy, J., et al. 2010, *ApJ*, 720, L72
- Snedden, C. 1973, *ApJ*, 184, 839

-
- Springel, V. & Hernquist, L. 2005, *ApJ*, 622, L9
- Stanek, K. Z. & Garnavich, P. M. 1998, *ApJ*, 503, L131+
- Stanek, K. Z., Mateo, M., Udalski, A., et al. 1994, *ApJ*, 429, L73
- Stanek, K. Z., Udalski, A., Szymanski, M., et al. 1997, *ApJ*, 477, 163
- Stetson, P. B. & Pancino, E. 2008, *PASP*, 120, 1332
- Sumi, T. 2004, *MNRAS*, 349, 193
- Tacconi, L. J., Genzel, R., Neri, R., et al. 2010, *Nat*, 463, 781
- Taylor, M. B. 2006, in *Astronomical Society of the Pacific Conference Series*, Vol. 351, *Astronomical Data Analysis Software and Systems XV*, ed. C. Gabriel, C. Arviset, D. Ponz, & S. Enrique, 666–+
- Toomre, A. 1977, *ARA&A*, 15, 437
- Trager, S. C., Worthey, G., Faber, S. M., Burstein, D., & Gonzalez, J. J. 1998, 116, 1
- Udalski, A., Paczynski, B., Zebrun, K., et al. 2002, 52, 1
- Valenti, E., Ferraro, F. R., & Origlia, L. 2004, *MNRAS*, 351, 1204
- Valenti, E., Ferraro, F. R., & Origlia, L. 2007, *AJ*, 133, 1287
- van Helshoecht, V. & Groenewegen, M. A. T. 2007, *A&A*, 463, 559
- Weiland, J. L., Arendt, R. G., Berriman, G. B., et al. 1994, *ApJ*, 425, L81
- Weinberg, M. D. 1985, *MNRAS*, 213, 451
- Weinzirl, T., Jogee, S., Khochfar, S., Burkert, A., & Kormendy, J. 2009, *ApJ*, 696, 411
- Williams, M. J., Zamojski, M. A., Bureau, M., et al. 2011, *MNRAS*, 414, 2163
- Worthey, G., Faber, S. M., Gonzalez, J. J., & Burstein, D. 1994, 94, 687
- Wozniak, H. & Michel-Dansac, L. 2009, *A&A*, 494, 11
- Wyse, R. F. G. & Gilmore, G. 1988, *AJ*, 95, 1404
- Zoccali, M., Hill, V., Lecqueur, A., et al. 2008, *A&A*, 486, 177
- Zoccali, M., Lecqueur, A., Barbuy, B., et al. 2006, *A&A*, 457, L1
- Zoccali, M., Renzini, A., Ortolani, S., et al. 2003, *A&A*, 399, 931

Acknowledgments

When I look back, since the first day I arrived to ESO to this moment, I can only think on how grateful I am of having Marina Rejkuba as my PhD supervisor. No matter how busy she was, she always managed to find the right time for me. She always made me feel that my project was the most exciting thing in which she was working on. This is definitely an indescribably encouraging feeling. I cannot thank her enough for the pleasure it was to work with her during these 3 years and for everything I learned from her.

I could have never wished for better mentors, all the way since my early undergraduate studies, than Manuela Zoccali and Dante Minniti. They have always been my examples of everything that is good in science. The enthusiasm they showed on every little result I got as well as the unconditional support when that particular result was not coming out as expected. They have been there since the beginning of my journey, and I sincerely hope to have the privilege to continue my scientific path with their company and friendship.

During my time at ESO I had the opportunity to meet a large number of excellent scientist who made me feel everyday that I was in the best possible place to do my research. In particular, I would like to thank Eric Emsellem and Markus Kissler-Patig for showing me the importance of scientific interaction and for advising me in key moments of my PhD.

I would also like to express my gratitude to so many people who contributed to my work during these three years, from sharing a simple thought to having a long discussion on my latest result; Ortwin Gerhard, Elena Valenti, Giussepina Battaglia, Rodolfo Smiljjanic, Camilla Juul Hansen, Inma Martinez-Valpuesta, Michael Williams and Michael Hilker. Of course, this list is far from being complete.

I would like to thank all my friends for the great support during this time. In particular, I will be forever indebted to Luca Ricci, as it was because of his unconditional friendship that I could overcome a very hard period of my life. I also thank my family for supporting me from so far away and showing so much interest in my work.

Finally, I cannot thank enough to Nora Luetzgendorf for her love and support during these last two years, for sharing my passion on research, and for understanding my special way of seeing life.

Curriculum Vitae

OSCAR A. GONZALEZ

10.04.84 Born in Chillan, Chile

EDUCATION

15.08.2009 - 15.08.2012 PhD in Astronomy

Ludwig-Maximilians University, Munich, Germany

Thesis title: “*Unfolding the Milky Way bulge*”, as part of the International Max-Planck Research School (IMPRS) at the European Southern Observatory (ESO)

Advisors: Prof. Dr. Ortwin Gerhard (LMU) and Dr. Marina Rejkuba (ESO)

01.03.2004-01.06.2009 Licenciatura (Diploma) Degree in Astronomy

Pontificia Universidad Católica, Santiago, Chile

Thesis title: “*Lithium rich RGB stars in the Galactic Bulge*”

Advisor: Prof. Dr. Manuela Zoccali

MEETINGS, WORKSHOPS & SCHOOLS

May 2012 “Metallicity gradients in the Galactic disks”, Bologna, Italy [Invited talk]

March 2012 “Third VVV science meeting”, Vina del Mar, Chile [talk]

November 2011 The 3rd Subaru International Conference: “Galactic Archaeology: Near-field cosmology and the formation of the Milky Way”, Shuzenji, Japan [talk]

September 2011 School of Astrophysics “F. Lucchin”: “Transition from low-mass stars to planets and galaxy bulges”, Erice, Italy [talk]

July 2011 “Optical and Infrared Galactic Plane Surveys”, Hertfordshire, UK [talk]

April 2011 “Assembling the puzzle of the Milky Way”, Le Grand-Bornand, France [talk]

December 2010 “First VVV science meeting”, Vina del Mar, Chile [talk]

May 2010 “Excellence Cluster meeting Research Area G”, Garching, Germany [talk]

November 2009 IAUS 268 “Light Elements in the Universe”, Geneva, Switzerland [Poster]

January 2009 “VII SOCHIAS Meeting”, Santiago, Chile [Poster]

February 2008 “Planetary Science Workshop”, San Juan, Argentina [Poster]

November 2007 “VI SOCHIAS Meeting”, Valparaiso, Chile

December 2006 Fourth Advanced School of Astrophysics: “Interferometry in the Epoch of ALMA and VLTI”, Santiago, Chile

REFEREED PUBLICATIONS

- “*Reddening and metallicity maps of the Milky Way Bulge from VVV and 2MASS. II. The complete high resolution extinction map and implications for bulge studies*”
Gonzalez O. A., Rejkuba M., Minniti D., Zoccali M., Valenti E., Schultheis M., Tobar R., Shen B.
2012 A&A, in press, arXiv: 1204.4004
- “*VVV DR1: The First Data Release of the Milky Way Bulge and Southern Plane from the Near-Infrared ESO Public Survey VISTA Variables in the Via Lactea*”
Saito R. K., Hempel M., Minniti D., Lucas P. W., Rejkuba M., Toledo I., **Gonzalez O. A.**, Alonso-Garcia J., and the VVV Team
2012, A&A, 537, 107
- “*C and N abundances of MS and SGB stars in NGC 1851*”
Lardo C., Milone A. P., Marino A. F., Mucciarelli A., Pancino E., Zoccali M., Rejkuba M., Carrera R., **Gonzalez O. A.**
2012, A&A in press, arXiv: 1202.6176
- “*The inner Galactic bar traced by the VVV survey*”
Gonzalez O. A., Rejkuba M., Minniti D., Zoccali M., Valenti E., Saito R. K.
2011c A&A, 534, L14
- “*Reddening and metallicity maps of the Milky Way Bulge from VVV and 2MASS. I. The method and minor axis maps*”
Gonzalez O. A., Rejkuba M., Zoccali M., Valenti E., Minniti D.
2011b, A&A, 534, A3
- “*Mapping the X-Shaped Milky Way Bulge*”
Saito R. K., Zoccali M., McWilliam A., Minniti D., **Gonzalez O. A.**, Hill V.
2011, AJ, 142, 76
- “*Alpha element abundances and gradients in the Milky Way bulge from FLAMES-GIRAFFE spectra of 650 K giants*”
Gonzalez O. A., Rejkuba M., Zoccali M., Hill V., Battaglia G., Babusiaux C., Minniti D., Barbuy B., Alves-Brito A., Renzini A., Gomez A., Ortolani S.
2011, A&A, 530, A54

- “*Lithium-rich giants in the Galactic thick disk*”
Monaco L., Villanova S., Moni Bidin C., Carraro G., Geisler D., Bonifacio P., **Gonzalez O.A.**, Zoccali M., Jilkova
2011, A&A, 529, A90
- “*VISTA Variables in the Via Lactea (VVV): The public ESO near-IR variability survey of the Milky Way*”
Minniti D. & the VVV team (**incl. Gonzalez O. A.**)
2010, NewA, 15, 433
- “*Li-rich red giant branch stars in the Galactic bulge*”
Gonzalez O. A., Zoccali M., Monaco L., Hill V., Cassisi S., Minniti D., Renzini A., Barbuy B., Ortolani S., Gómez A.
2009, A&A, 508, 289

OTHER PUBLICATIONS

- “*Towards the big picture of the Milky Way bulge*”
Gonzalez O. A.
2012, EPJWC, 19, 06005G
- “*VISTA Variables in the Via Lactea (VVV): Current Status and First Results*”
Saito R. K., Hempel M., Alonso-Garcia J., Toledo I., Borissova J., **Gonzalez O.A.**, et al.
2010, Msngr, 141, 24S
- “*Li-rich giants in the Galactic Bulge. Is Li linked only to evolutionary status?*”
Gonzalez O. A.
2010, IAUS, 268, 333G
- “*Chemistry of the Galactic Bulge: New Results*”
Zoccali M., Hill V., Barbuy B., Lecureur A., Minniti D., Renzini A., **Gonzalez O. A.**, Gomez A., Ortolani S.
2009, Msngr, 136, 48Z
- “*Observatory UC at Santa Martina: A small observing facility operated by PUC*”
Baffico M., Avila G., Baade D., Bendek E., Guirao C., **Gonzalez O.**, Marchant P., Salas V., Toledo I., Vasquez S., Vanzì L.
2008, Proceedings of SPIE Vol. 7012, [7012-99]

PROFESSIONAL SERVICES

- Referee for A&A and ApJ
- ESO OPC assistant for period 85-86-87-88-89-90
- ESO Journal club Co-organizer, 2010 to present

- Co-organizer of Excellence Cluster meeting Research Area G, May 2010
- LOC of ESO Workshop Science from the Next Generation Imaging and Spectroscopic Surveys